

Sheath for Reducing Local Scour in Bridge Piers

Robie Bonilla Gris¹, Member, ASCE

¹Professor (retired), Instituto Politécnico Nacional, México, Retorno de Chapulines # 316, Frac. Club de Golf, Tequisquiapan, Qro., México, 76750, email: robie_bonilla@yahoo.com

ABSTRACT

A sheath is presented which reduces the local scour around structures placed in a fluvial, lacustrine, estuarine, coastal or marine environment susceptible to scour. Such structures can be piers and abutments of bridges, columns, and other objects. The sheath has an especially designed rugosity which reduces the effect of the secondary flow that occurs in the border of attack of the structure. Additionally, the sheath can include complementary elements to give the ensemble a streamlined profile, enhancing the anti-scour performance. Also, it could be configured to rotate freely to align with a variable direction of flow, if needed. Preliminary experimental work indicates that the sheath could be a solution against local scour, the main cause of collapse of bridges. The sheath could be cost-effective; could withstand any hydraulic conditions; its installation would not need heavy equipment; does not provoke alterations in the watercourse; can substitute environment-altering solutions; being underwater, does not interfere with the structure's aesthetics; could be used as a preventive or as a remedial measure.

INTRODUCTION

A problem frequently found in the case of structures and objects submerged in moving bodies of water is the *local scour* or erosion of material of the bottom in which they lean on, induced by the alteration of the flow caused by the presence of those structures and objects. This alteration consists of local increases of velocity and of the onset of secondary flows and of turbulent wakes with whirls or vortices. The local scour removes material of the bottom around the structures and objects and can put at risk their support, threatening their stability and its security and those of the corresponding superstructure, if any.

In spite of the technical development achieved through research (theoretical, experimental and with the help of numerical simulation and with field studies), carried out in institutions of many countries, and in spite of the interest of the official institutions in charge of the ground communications infrastructure and in spite of the enormous amounts of money invested in the search of solutions, *scour is the main cause of the collapses of bridges, worldwide*. 60% of those disasters is due to this phenomenon; because of that, nowadays it is still a factor of paramount importance in the design of these structures and an urgent technical

challenge to solve (Jones, 2000; Khotyari, 2001; Parker, 1995; Briaud, 2005; Annandale, 2002).

In the United States, 17,000 bridges are considered in critical state with regard to scour (Briaud, 2005). The great number of bridges (about 600,000 in the United States) (Briaud, 2005) gives an indication of the problem dimension, and of the dramatic impact in the economy. The costs directly related to the bridge collapses are always very high. For example, 19% of the federal emergency funds of the United States used in the item of highways are used in the restoration of bridges. It should be added to the direct costs of a bridge collapse the indirect costs due to the serious affectations to roads and the dysfunctions in many activities; such costs can be even higher than the direct costs: the Federal Highway Administration estimates that these indirect costs can be five times the direct ones (Annandale, 2002). There is also a cost of prevention of those disasters.

The collapses of bridges, above all, are an important risk for the public security: human lives have been lost in those disasters.

Other examples of structures susceptible to damage due to local scour are piles, columns, supports of structures or equipment or machines, and similar structures, leaning or anchored in the bed or bottom or in the riverbanks of a ravine, a body of water or an artificial conduct or in a fluvial, lacustrine, estuarine, coastal or marine environment.

THE LOCAL SCOUR

The collapse of a bridge due to local scour generally begins with the loss of support of one or more piers. One of the abutments can also fail.

Local scour is produced by a complex turbulent flow that is mainly the effect of two independent, well-known mechanisms. A brief explanation of those two different causes of the local scour follows.

First mechanism: *The horseshoe vortex*. Figure 1 shows a submerged structure or object, leaning on an erodible bottom. The flow **11** that collides against the border or attack area of the structure **10** (the area that directly faces the current or flow) is deflected downward by the vertical gradient of the stagnation velocities, generating this way the *secondary flow* **12**, which travels vertically, in close contact with the front of attack of the structure. The secondary flow powers the so-called *horseshoe vortex* **13**. This vortex surrounds the submerged structure or object, in contact with the bottom, and spreads downstream, transporting sediment detached by the secondary flow and also removing material from the bottom around the structure; that material is then carried away by the current, giving place to the scour hole.

This first mechanism is the main responsible for the local scour.

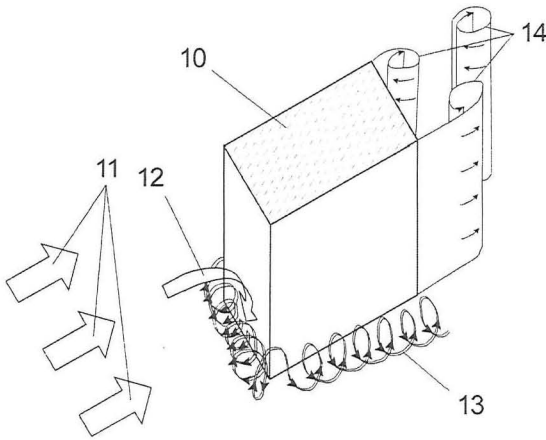


FIG. 1. Local scour mechanisms

Second mechanism: *wake vortices* 14 (Fig. 1). The flow that surrounds the submerged structure or object produces vertical vortices called *wake vortices*. These vortices tend to appear periodically and alternately from one side and the other of the structure and are carried away by the flow. As small tornadoes, they remove particles from the bottom and put them to movement; the flow transports them and so completes the second local scour mechanism. The wake vortices belong to the turbulent wake caused by the presence of the structure inside the flow.

If the depth of the scour hole, basically due to the combined effect of the two described mechanisms, surpasses certain critical magnitude, the support of the structure is reduced and its security is at risk.

THE STATE-OF-THE-ART

The current state-of-the-art consists on facing the problem with the following main types of measures intended to reduce the scour effects around the submerged structure:

1. The protection of the bed or bottom near the submerged structure, using one or more of the following resources: rock, monolithic precast and cast-in-place concrete structures, crushed concrete, riprap, mattresses or mats of several types constituted by such heavy elements as bags made of plastic meshes or geotextiles containing concrete or stones, layers of stones retained and separated by geotextiles, gabions, concrete blocks tied to each other by steel cables, and other resources.

2. The construction on or near the submerged structure of some appendices or elements, whose shape helps to deviate the flow away from the structure, or whose position and shape tend to move the scour away from the structure, such as spurs, flow deflectors, semicircular or triangular endnoses, protection slabs, collars, sacrifice piles and other elements.

3. The construction or setting of the structure foundation to considerable depths, greater than the scour depths estimated by means of the available calculation formulae. The reason of this measure is that such formulae don't give very reliable results; their error margins are generally big. Also, their application is limited because they don't consider the cases of complex flows, like those that include surf and variable currents; furthermore, they don't take into account complex geotechnical characteristics of the bottom and are only applied to simple shapes of piers.

From the functional point of view, the described measures, which constitute the main body of the current state-of-the-art, have as objective to reinforce the scour-susceptible bed or bottom, or to move away the phenomenon of scour away from the structure or object to protect, or set the structure to a depth that responds more to a collapse fear than to a rational, engineering decision. That is, the state-of-the-art attempts, at great cost and without much success, to reduce the effects of local scour, without directly attacking the cause of the phenomenon itself. The statistics of vulnerability of the submerged structures to the action of local scour show that the protection obtained nowadays is faulty and that there is an urgent need of better solutions.

Only some relatively recent developments are based on the control of the hydrodynamics responsible for the mechanisms that produce the local scour. The FHWA Sterling Jones Hydraulics Research Laboratory (2007) has a current research project which considers using streamlining of the shape of a bridge pier and also roughness elements on the surface of the pier. Khwairakpam and Mazumdar (2009) report about some flow-altering techniques, using splitter plates or threaded piles (Day, S.; Sumer, B. M. and Fredsøe, J., 2006) and pier slots and collars (Kumar, V., Ranga Raju, K. G. and Vittal, N., 1999).

DESCRIPTION OF THE SHEATH

The patented sheath presented here (Bonilla Gris, R., 2009) faces the problem of local scour attacking its origin itself, modifying conveniently the flow near the submerged structure or object, in order to reduce the intensity and the effect of the mechanisms of local scour.

The sheath (Fig. 2) is to be placed around the exterior surface of the structures and objects submerged in a current or flow. Those structures and objects can have any shape and can be made of any material.

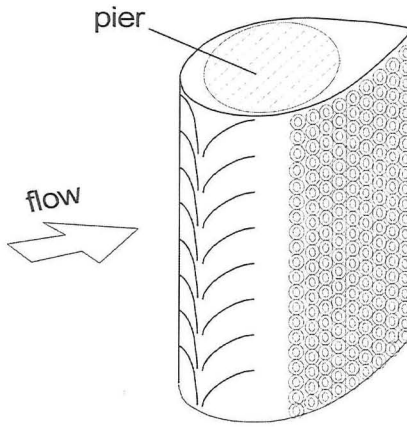


FIG. 2. The pier sheath

The sheath has the following basic features:

(a) A specially designed artificial *directional* rugosity in the front of attack, whose characteristics will be described later on.

This artificial rugosity has a decisive influence on the downward secondary flow through the creation of systems of inclined vortices which are carried away by the current without arriving to the bottom, resulting in a damping of the vertical momentum of the secondary flow.

(b) A specially designed *non-directional* rugosity in the rest of the external surface, which gives the sheath a "golf ball" effect; that is, transforms the laminar boundary layer to turbulent relocating the flow separation line downstream of the position corresponding to a smooth pier. This way, the wake reduces its strength and so do the wake vortices.

The current local scour state-of-the-art, in general, doesn't take into consideration the characteristics of the surface of the submerged structures; it is customary to give it a smooth finish, when the structure is made in a form (as in the most frequent case, of concrete structures), and to keep unchanged the natural rugosity of the construction material, in other cases.

(c) Optionally, an efficient hydrodynamic, streamlined profile that reduces the area of the front of attack—then the secondary flow and the horseshoe vortex momenta—and produces a minimum turbulent wake. In this option, the non-directional rugosity is excluded.

In the current state-of-the-art, it is not usual to give the submerged structures and objects a very convenient hydrodynamic (streamlined) profile, due to high construction costs because forms of complex geometry are needed, when the structures or the objects are built of reinforced concrete or another formed material; also, there are structural and damage susceptibility issues.

(d) Also, optionally, the streamlined ensemble could be so made as to rotate freely around the structure, to align itself automatically with a variable direction of flow.

The sheath would be put on the pier so that its directional rugosity is located in the border or area of attack of the submerged structure. In the case of structures located in flows whose direction is variable, as in estuarine, coastal and marine environments or in rivers with tide influence, the directional rugosity would face the different directions, or would be put in the whole perimeter; also, the sheath could be made so as to have the hydrodynamic profile and to rotate freely to align automatically with a variable direction of flow.

The sheath is conceptually made of the cover (Fig. 2) that contains the two types of artificial rugosity; optionally, the sheath may include one or more intermediate components fixed to the submerged structure. Those intermediate components would give the ensemble the streamlined profile and hold the cover in place.

The rugous cover could be formed out, for example, of a flexible, water- and weather-proof material, as well as resistant to the particular characteristics of the flowing liquid (it must be resistant to brackish or salt water found in the estuarine, coastal and marine areas). It also must have appropriate mechanical characteristics in order to be fastened to the intermediate components, or directly to the submerged structure or object, if no intermediate elements are present, and to remain this way. The cover would resist cutting, tearing and bumping due to floating matter. It must also fulfill the environment protection standards.

The intermediate component or components would be manufactured from a material which can be conveniently formed and that keeps its shape and dimensions along the work life of the sheath. It would also be capable of being held by means of a simple procedure to the structure or object to be protected; for example, it can be made up of two or more complementary parts that can be united to each other in a simple way. The intermediate component would also be capable of holding fast the cover.

The directional rugosity is constituted by linear rugous elements in the shape of stripes distributed in an essentially symmetrical way with regard to the vertical axis of the border of attack of the structure (Fig. 2). The non-directional rugosity consists of a multiplicity of individual rugous elements.

Due to the fact that the vertical gradient of the stagnation velocities increases with the water depth, making the secondary flow become gradually swifter as it approaches the bed, the sheath should be fixed on the pier so as to sit on the bed. Also, the most important stretch of the vertical dimension of the sheath being the lower part, the sheath's height could be less than the design water depth.

The parameters of the hydrodynamic profile would depend on the pier shape and size and on the Froude Number range of the watercourse or of the water environment velocities. As for floating debris, the hydrodynamic profile of the sheath, having the same maximum width as the pier (with a difference of less than 10 cm) and a smaller area of attack, it seems that would retain less debris than the pier itself; the inclined and curved stripes of the rugosity would also help.

EXPERIMENTAL RESULTS

The advantageous results of the application of the artificial rugosity of the sheath in the reduction of local scour, have been proven in 2 preliminary experimental studies in a Hydraulics laboratory, using scale physical models with the characteristics indicated in the following abbreviated description; in that description the following dimensionless hydrodynamic parameters are used:

$$F = \frac{U}{\sqrt{gd}} \quad (1)$$

(Froude Number), where U is the mean velocity of the flow, g is the acceleration due to gravity and d is the flow depth.

$$R = \frac{UD}{\nu} \quad (2)$$

(Reynolds Number), where U is the mean velocity of the flow, D is the diameter of the cylindrical pier and ν is the coefficient of kinematic viscosity of the liquid.

In the first study, a channel of rectangular section 0.56 m wide, a flow of 21.6 l/s were used and as bottom material, ground Bakelite with an initial transport velocity of 0.14 m/s. In the experiment, cylindrical piers with a diameter of 0.07 m were used and the flow depth was 0.27 m. The Froude Number was 0.09 and that of Reynolds, 8.8×10^3 .

The second study was carried out in a channel of rectangular section 1.50 m wide, with a flow that varied between 49.5 and 59.4 l/s; the material of the bottom was sand and its initial transport velocity was 0.22 m/s. Cylindrical piers 0.10 m in diameter were used; the flow depth varied from 0.12 m to 0.20 m. The values of the Froude Number varied between 0.14 and 0.27 and the values of the Reynolds Number, between 1.7×10^4 and 2.7×10^4 .

Both series of experiments were done in clear-water sediment conditions.

The tests were done to assess the scour-reducing performance of the artificial roughness created on a cylindrical pier, relative to a cylindrical smooth pier with the same diameter in the same hydraulic and sediment conditions. Because of

this restraint, several parameters were left out of the picture as variables: streambed and sediment characteristics, depth and angle of attack of flow, shape and relative obstruction of the pier. The duration of every couple of tests (smooth pier, rugous pier) was the same; they were stopped when the smooth pier scour depth was no longer time-dependent.

As already noted, no streamlined profile was added to the model piers.

In every experiment, with a variety of rugosities, the maximum scour depth and the total scour volume were calculated.

The results of both laboratory studies showed a significant reduction of the depth and volume of the scour hole in piers with the artificial rugosity, in comparison with the values corresponding to a smooth pier under the same hydrodynamic and sediment conditions (Fig. 3). The reduction in scour depth ranged from 20% to 30%. A scour hole topography different from that of the well-known smooth pier scour hole was found.

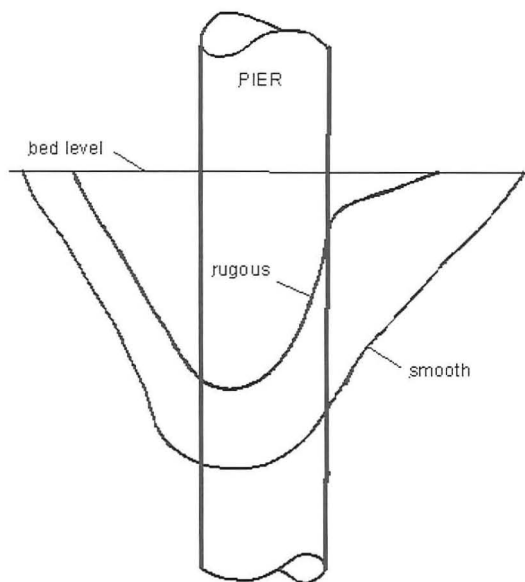


FIG. 3. Scour holes for rugous and smooth piers (typical)

CONCLUSIONS AND RECOMMENDATIONS

1. In comparison with the common measures and solutions provided by the state-of-the-art, the sheath, besides being efficient in the reduction of the local scour, has the following advantages:

- (a) It can be applied, as a preventive measure against local scour, to recently built or placed submerged structures and objects; also, as an attenuation or remediation measure, can be applied to others that already run risks or have problems due to this phenomenon.
- (b) It could be cost-effective, since the application of the sheath would not require considerable additional work, neither additional times of construction, or heavy equipment.
- (c) It can resist any hydrodynamic conditions of velocity and turbulence.
- (d) The optional streamlined profile of the sheath is independent of the profile of the submerged structure, so that the sheath can be applied to any shape of horizontal section of such structure.
- (e) It doesn't increase the underwater profile of the structure, and then it does not produce parasite scour effects downstream of the structure, which could do harm.
- (f) It doesn't interfere with the aesthetics of the structure, since the sheath can be applied under the water level.
- (g) The technology is simple, of easy transfer and application.
- (h) The technology can substitute environment-altering solutions.

2. The addition of artificial rugosity to the surface of a pier as a local scour countermeasure sets a new paradigm –the state-of-the-art of local scour depth assessment (formulae, parameters, criteria) assumes beforehand that the pier or structure is smooth---. In fact, the experimental work mentioned shows that *the smooth pier is the worst performer in respect to local scour*. This means that a new parameter representing rugosity should be included in the current formulae.

3. The experimental results presented here were obtained in cylindrical piers; the streamlined sheath, having a smaller front of attack, should generate a weaker secondary flow and horseshoe vortex; then, better anti-scour performance. This conclusion can be applied also to the downstream end of the sheath; the wake vortices produced will be less strong.

4. As mentioned, the hydrodynamics of the lab tests were observed without high-speed instrumentation; then, the flow near the rugosity must be studied with more precise methods to fully assess and optimize the artificial rugosity effect.

5. The results presented here should be confirmed by extensive laboratory tests and also by tests in real structures.

Some pending studies are:

(a) Refined rugosity characteristics for smallest scour depth (for different Reynolds Number ranges);

(b) Best hydrodynamic profiles for different ranges of flow conditions;

(c) Needed vertical extent of the sheath (probably, not through the entire water depth).

REFERENCES

- Annandale, G. W., Melville, B., Chiew, Y. (2002). "Scour Case Studies". *Mitteilungsblatt der Bundesanstalt für Wasserbau*, Nr. 85 (*Information Newsletter of the Federal Institute of Rivers and Channels Engineering and Research*, Germany, (No. 85)).
- Bonilla, R., U. S. Patent No. 7628569, PCT filed July 12, 2005.
- Briaud, J. L. (2005). "SRICOS Sheds Light on Bridge Scour Problems". *Texas Transportation Researcher*, Texas Transportation Institute, (Vol. 34, No. 2).
- FHWA Sterling Jones Hydraulics Research Laboratory, Current Research Project: "Pier Scour Countermeasures Using Fluidic Devices". (2007). Available at: <http://www.fhwa.dot.gov/engineering/hydraulics/research/summary.cfm>
- Hamill, L. (1999). *Bridge Hydraulics*, E&F Spon, London and New York.
- Jones, J. S. (2000). "Hydraulics Testing of Wilson Bridge Designs". *Public Roads*, Federal Highway Administration, U. S. Department of Transportation, (March/April 2000, Vol. 63 No. 5).
- Khotyari, U. C.; Ranga R. K. G. (2001). "Scour Around Spur Dikes and Bridge Abutments". *Journal of Hydraulic Research*, (Vol. 39, 2001, No. 4).
- Khwaitrakpam, P.; Mazumdar, A. "Local Scour Around Hydraulic Structures". *International Journal of Recent Trends in Engineering*, ACEEE, (Vol. 1, No. 6, May 2009).
- Parker, G., Voigt, R. (1995). "Countermeasures to Protect Bridge Piers from Scour". *National Cooperative Highway Research Program*, (NCHRP Project 24-7(2)).

Effects of Collars on Scour Reduction at Bridge Abutments

Mustafa Gogus¹ and Abdullah Ercument Dogan²

¹ Middle East Technical University, Department of Civil Engineering, Hydraulics Laboratory, Ankara-Turkey, phone: +90 312 210 54 99; fax: +90 312 210 24 38; email: mgogus@metu.edu.tr

² PLANSU Engineering & Consultancy Company, Ankara-Turkey; phone: +90 312 219 53 11; fax: +90 312 219 53 18; email: ercumentdogan@plansu.com

ABSTRACT

Bridge failures are generally resulted from scour of the bed material around bridge piers and abutments during floods. In this study, scour phenomenon around bridge abutments and collars, located at abutments as scour countermeasures, were experimentally investigated.

Based on the results of 97 experiments conducted, the effect of various sizes of collars which were located around the abutments at different elevations, on the scour reduction at bridge abutments was determined. The results were compared with previous studies, and the effect of the sediment grain size on the performance of abutment collars was emphasized. It was noticed that when the collar width was increased and it was placed at or below the bed level, the reduction in the maximum local scour depth increases considerably. It was also seen that the change of the sediment size did not affect the optimum location of the collar at the abutment, which yields the maximum scour reduction around the abutment.

INTRODUCTION

There are numerous works, experiments and case studies given in the literature about pier scour and abutment scour concept. The statistical data show that in a bridge failure case, the main reason of the failure is most probably the pier or abutment scour (Melville 1992, Kandasamy and Melville 1998).

In the literature there are many studies related with the pier scour and its countermeasures. For bridge pier countermeasures, the NCHRP 24-7 (1998) project final report named "Countermeasures to Protect Bridge Piers from Scour" has reviewed nearly all the literature in this aspect and also has given recommendations and design suggestions for a number of countermeasures. Also, the Federal Highway Administration has developed several comprehensive technical manuals for dealing with the problem of bridge scour. Moreover, a field survey of pier countermeasures was carried out across the United States (Li, Kuhnle, and Barkdoll 2006). However, the scour at bridge abutments has received less attention, and especially the future works on countermeasures for abutment scour are greatly needed.

The literature review shows that the researchers studied the collars mainly to reduce the local scour at bridge piers. The researchers like Dargahi (1990), Chiew (1992, (b)), Kapoor and Keana (1994), Kumar et. al. (1997), Singh et. al. (2001), Mashahir and Zarrati (2002), and Borghei et al. (2004) all investigated the reducing effect of the collars on the local scour at bridge piers.

There are fewer researchers studying the countermeasure effect of collars on bridge abutment scour. Kayatürk (2005) conducted experiments in a rectangular channel with glass side walls, 30.0 m long, 1.0 m deep and 1.5 m wide, with erodible uniform sand having a median diameter of $d_{50} = 1.48$ mm under clear water conditions. The tests showed that with a flow depth of 0.10 m and a flow rate of 0.050 m³/s, the bed material would be at incipient motion condition. The ratio of the shear velocity in these experiments to the critical shear velocity calculated from Shield's diagram was about 0.90. Kayatürk (2005) tested vertical wall abutments having rectangular plan view with a constant width of $B_a = 10$ cm and five different lengths perpendicular to the flow direction $L_a = 7.5$ cm, 15 cm, 20 cm, 25 cm and 35 cm. For rectangular collars of widths, $B_c = 2.5$ cm, 5.0 cm, 7.5 cm and 10 cm were tested with each abutment at various elevations from the bed level, $Z_c = -5$ cm, -2.5 cm, ± 0.0 cm, 2.5 cm and 5.0 cm, for a time period of 6 hours. Based on the experimental results Kayatürk (2005) stated that the efficiency of a collar was a function of its size and its vertical location on the abutment. As the size of the collar increases, the scour depth decreases. If the ratio of the abutment length to the flow depth $L_a/y > 1$, the efficiency of the collar increases with decreasing L_a/B_c and the elevation of the collar shifts in downward direction from the bed level, as long as the clear water flow conditions are satisfied, regardless of the flow depth. If $L_a/y < 1$, the collar, which is placed at the bed level ($Z_c/y = \pm 0.00$), gives higher performance than those having other Z_c/y values. Instead of full-collars, the partial collars can be used to provide maximum reduction in the scour depth from an economical point of view (Kayatürk, 2005).

Li, Kuhnle and Barkdoll (2006) have conducted some laboratory experiments with collars at a vertical-face wing wall abutment placed at the main channel edge, an abutment configuration typical of older bridges on smaller streams. To mitigate the abutment scour, flat, horizontal, steel collars were attached around a wing-wall abutment ending at the main channel edge under clear-water flow conditions in a laboratory flume channel. It was found that these collars were able to protect the bridge abutment efficiently by eliminating secondary vortices that ordinarily would cause local scour. The minimum collar dimensions that eliminated the local scour were a flow perpendicular width of $0.23 L_a$ (L_a is the abutment length perpendicular to the flow direction) and a flow parallel length of 0.7 times the flow parallel abutment width. It was determined that a vertical location of $0.08 y$ (where y is the main channel flow depth) below the mean bed sediment elevation gave the best results of scour reduction. In addition, the collar did not only reduced the scour magnitude near the abutment, but also retarded the development of the scour hole.

This review exposes that there is a gap in the literature related to the use of collars to mitigate abutment scour. Although there are some studies conducted and presented, there is a need for further investigation of this phenomenon.

The aim of this study is to investigate the effect of the grain size of the bed material on the performance of collars on reducing the local scour depth at the base of the abutments. For this reason, a series of experiments were conducted at the laboratory under clear water flow conditions with vertical abutments and collars of various sizes using almost uniform sand of $d_{50} = 0.90$ mm and the results obtained

were compared with those of Kayatürk (2005) to see they are valid or not for finer bed materials.

EXPERIMENTAL SETUP

The experiments were conducted in a 1.5 m wide, 1.0 m deep and 30 m long, flume with glass side walls and a bed slope of $S_0 = 0.001$. The working section, in which the abutments were located, was 10 m long with a recess on the bed 0.50 m deep and was situated 10 m downstream from the entrance of the flume. The recess was filled with uniform sediment with a diameter of 0.90 mm.

The longitudinal cross-sectional view of the flume is shown in Figure 1.a. The flume had a closed-loop water system and the flow to the flume was supplied from a constant-head water tank by a pump. A gate was mounted at the tail end to adjust the flow depths.

The flow discharge was measured with a sharp-crested rectangular weir mounted at the upstream section of the flume. By means of bricks and sheet-iron strainer placed between brick walls, located at the entrance of the channel as a filter, turbulence of the flow was reduced and the uniform flow conditions were maintained which were required for upstream head measurements. The scour depths were also measured with a point gage to an accuracy of ± 1 mm. The tip of the gage was painted with white paint and for each measurement the painted tip penetrated the sandy bottom of the scour hole until it could no longer be seen.

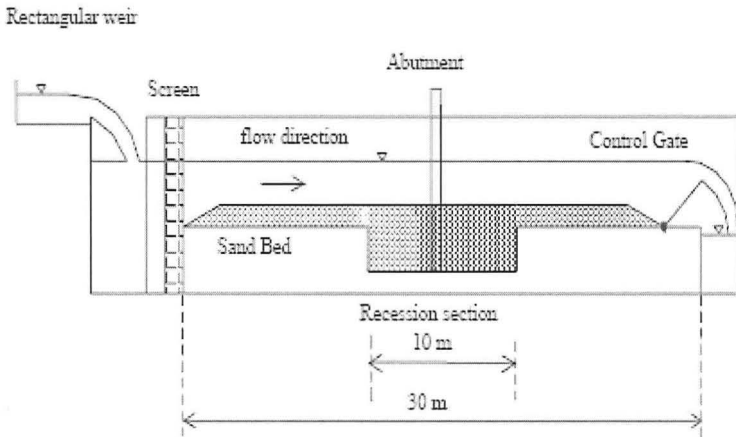


Figure 1.a. The longitudinal cross-section of the experimental setup

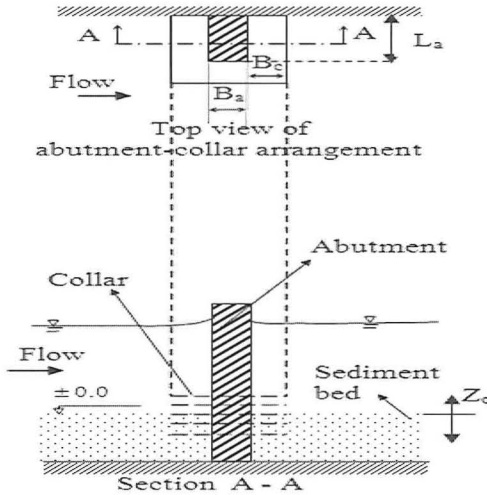


Figure 1.b. Abutment-collar arrangement

The abutments and collars used in this study were manufactured from 3 mm thick Plexiglas at the laboratory (Figure 1.b.).

The lengths of the abutments rectangular in plan were the same as those used in Kayatürk's study (2005) as being 35 cm, 25 cm, 20 cm, 15 cm, and 7.5 cm with a constant width of 10 cm (Table 1.). According to Oliveto and Hager (2002), and Kayatürk (2005), the effect of the stream wise abutment length on the development of the scour hole is small and can be neglected. Four different collars of widths, $B_c = 2.5$ cm, 5.0 cm, 7.5 cm and 10 cm, were tested with each abutment (Table 1).

EXPERIMENTAL PROCEDURE

All tests were conducted under the clear water flow conditions at $U^*/U_{*c} = 0.90$, where U^* is the shear velocity of the approach flow and U_{*c} is the value of U^* at the threshold of grain motion. The threshold flow depth of bed material motion, $y_c = 5.3$ cm, was calculated from the Shield's diagram. Then, the result for y_c was confirmed with the experimental observation when the abutment was not installed. Finally, the flow depth satisfying the ratio of $U^*/U_{*c} = 0.90$ was calculated as $y = 4.25$ cm, and the experiments were conducted by using this flow depth, which corresponds to upstream Froude and Reynolds numbers of 0.41 and 43439, respectively.

After locating the abutment in place in the flume without or with a collar, the experiments were started by filling the channel with water without disturbing the leveled surface of sediment bed until the water depth was adjusted to satisfy the ratio of $U^*/U_{*c} = 0.90$, by making use of the control gate placed at the far downstream of the flume. When the corresponding flow depth ($y = 4.25$ cm) and discharge ($Q =$

0.017 m³/s) were achieved and the flow regime was checked as being uniform by making use of line meters attached to the glass side walls of the flume, the experiment was started. The scour hole was obtained by performing a 6-hour continuous run under clear water conditions and both the maximum scour depth and the scour formation at the abutment site were investigated. The maximum scour depth at the end of a 6-hour continuous run was determined with the help of a mirror by estimating the distance between the zero level of the mirror and the current level of the channel bed. At the end of each experiment, the flume was carefully drained and sand bed level was straightened and compacted for the next experiment with a special apparatus, which was made of steel plate welded on a steel frame. Before the straightening and compaction of the channel bed, the longitudinal cross-sectional bed profile in front of the abutment face, where the maximum scour depth occurred, was gauged and recorded in the flow direction. The frame used for straightening could slide from the beginning to the end of the flume over steel rails which were mounted on the glass side walls.

As the efficiency of the collar is also a function of its vertical location on the abutment, collars of different sizes were placed at different elevations on the abutments (Z_c) as; at the bed level, 1.0 cm and 2.0 cm above the bed level and also 1.0 cm and 2.0 cm below the bed level. In Table 1, all collars used are classified considering their sizes and also abutment types.

Table 1. Abutment and collar sizes used in the tests

Z_c (cm) = +2.0, +1.0, ±0.0, -1.0, -2.0 (with respect to the channel bed)			
Type	L_a (cm)	Case	B_c (cm)
1	7.5	a	10.0
		b	7.5
		c	5.0
		d	2.5
2	15	a	10.0
		b	7.5
		c	5.0
		d	2.5
3	20	a	10.0
		b	7.5
		c	5.0
		d	2.5
4	25	a	10.0
		b	7.5
		c	5.0
		d	2.5
5	35	a	10.0
		b	7.5
		c	5.0
		d	2.5

Maximum Scour Reductions around the Abutments with Collars

The total number of the experiments conducted; with abutments of lengths: $L_a = 7.5$ cm, 15 cm, 20 cm, 25 cm and 35 cm, collars of widths: $B_c = 2.5$ cm, 5.0 cm, 7.5 cm and 10 cm, and finally collar locations of $Z_c = -2.0$ cm, -1.0 cm, ±0.0 cm, 1.0 cm and 2.0 cm is 97. The experiments for the abutment length of 7.5 cm with the

collar widths of 10 cm, 7.5 cm, and 5 cm at the elevation of $Z_c = -2.0$ cm have not been performed. The reason is that the propagation of the scour depth in the vertical direction is stopped during the experiments for $Z_c = -1.0$ cm, meaning that there is no sense or need to locate collars below this limiting level. The bed profiles obtained at the end of these experiments and the maximum scour depths around the abutments for each experiment were determined. Then, the scour depths around abutments with and without collar were compared to see the percent reduction in the scour depth.

In Figure 2, the overall effect of abutment length, collar width and the location of the collar on the reduction of maximum scour depth can be seen according to the results of this study. Figure 3 is provided to show the same graph for the Kayatürk's results (2005). Each line given in the figures corresponds to a constant L_a/B_c value. According to the plot of Kayatürk (2005), at small values of L_a/B_c which is less than about 2.0, maximum reductions in scour depths are mainly obtained when the collars are located at the bed level, $Z_c/y = \pm 0.0$. For greater values of L_a/B_c , maximum reduction in scour depths are mostly observed when the collars have the value of $Z_c/y = -0.50$. This figure also clearly shows that scour reduction capacity of a collar increases as the width of the collar increases, and decreases with increasing abutment length. Collars are generally more effective in reducing the scour depth around the abutment when they are located below the sand bed, $-0.50 < Z_c/y < -0.25$, compared to the cases of above the sand bed, $0.0 < Z_c/y < 0.50$, for the value of $L_a/B_c > 2.0$. The trend lines of the data points in Figure 2 also imply that at Z_c/y values less than -0.50 , higher reductions in the maximum scour depths around the abutments can be obtained than those given in the figure for $Z_c/y = -0.50$. For design purposes when the optimum value of Z_c/y is required, the one close to the bed level but having adequate scour reduction capacity should be selected (Kayatürk, 2005). When Figure 2 is compared to Figure 3 it is clearly seen that the general trends of the data of the same abutment and collar are very similar. At small values of L_a/B_c , which is less than and equal to 2.0, the maximum reductions in the scour depths are mainly obtained when the collars are located at the bed level, $Z_c/y = \pm 0.0$. For the range of L_a/B_c between 2 and 5, the maximum reduction in the scour depths is observed for Z_c/y values between -0.24 and -0.47 . But, it has a fluctuating behavior. For L_a/B_c values greater than and equal to 5, the optimum Z_c/y occurs at $Z_c/y = -0.47$, which is similar to the results of Kayatürk (2005). One additional observation can be summarized as, the increase in the collar width increases the scour reduction performance of the collar, whereas the increase in the abutment length decreases this efficiency. This holds true for both studies.

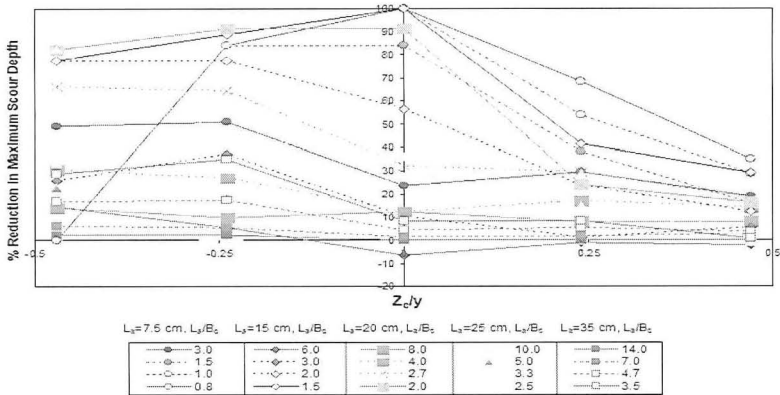


Figure 2. Effect of collar size and elevation on the maximum scour depth around the abutments of various lengths ($Q = 0.017 \text{ m}^3/\text{s}$, $y = 4.25 \text{ cm}$, $d_{50} = 0.90 \text{ mm}$)

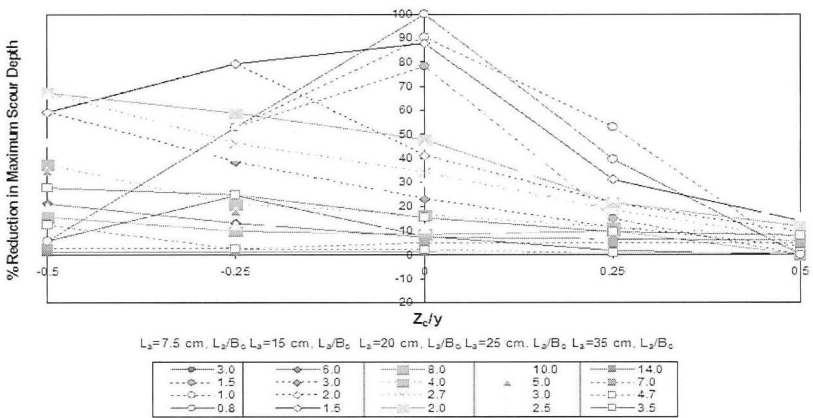


Figure 3. Effect of collar size and elevation on the maximum scour depth around the abutments of various lengths ($Q = 0.050 \text{ m}^3/\text{s}$, $y = 10 \text{ cm}$, $d_{50} = 1.48 \text{ mm}$) (Kayatürk, 2005)

According to the results of the experiments, the locations of the collars having the best scour reduction efficiency for each abutment length and collar width were chosen and presented in Table 2 along with the corresponding values of $[(d_s)_{\max,c} / y]_{opt}$ and $[Z_c / y]_{opt}$. Here, $(d_s)_{\max,c}$ is the maximum scour depth obtained

from experiments conducted with collars, $\%Reduction = [(d_s)_{max} - (d_s)_{max,c}] / (d_s)_{max}$ where $(d_s)_{max}$ is the maximum scour depth around the abutment without collar.

Table 2. Results of present study and Kayatürk's one (2005)

		RESULTS OF PRESENT STUDY			KAYATÜRK'S RESULTS (2005)		
L_a/B_c	L_a/B_c	$[Z_c/y]_{opt}$	$[(d_s)_{max,c}/y]_{opt}$	$[\%Reduction]_{opt}$	$[Z_c/y]_{opt}$	$[(d_s)_{max,c}/y]_{opt}$	$[\%Reduction]_{opt}$
0.75	3	-0.24	0.73	50.8	-0.25	0.40	24.5
	1.5	0.00	0.24	84.1	0.00	0.12	77.3
	1	0.00	0.00	100.0	0.00	0.05	90.3
	0.75	0.00	0.00	100.0	0.00	0.00	100.0
1.5	6	-0.47	1.79	14.6	-0.50	0.97	23.0
	3	-0.24	1.32	37.1	-0.50	0.50	60.0
	2	-0.24	0.47	77.5	-0.25	0.25	80.0
	1.5	0.00	0.00	100.0	0.00	0.15	86.0
2	8	-0.47	2.26	14.3	-0.50	1.29	16.0
	4	-0.47	1.84	30.4	-0.50	0.96	37.0
	2.67	-0.47	0.89	66.1	-0.50	0.60	61.0
	2	0.00	0.24	91.1	-0.50	0.50	67.0
2.5	10	-0.47	2.64	1.8	-0.50	1.47	20.0
	5	-0.47	2.07	22.8	-0.50	1.19	35.0
	3.33	-0.47	1.79	33.3	-0.50	0.98	46.0
	2.5	-0.47	0.47	82.5	-0.50	0.61	67.0
3.5	14	-0.47	3.04	2.3	-0.50	1.99	1.0
	7	-0.47	2.92	6.1	-0.50	1.95	2.9
	4.67	-0.24	2.56	17.4	-0.50	1.76	12.4
	3.5	-0.24	2.02	34.8	-0.50	1.45	28.0

To determine the optimum locations of the collars for known values of L_a/B_c , the data of $[Z_c/y]_{opt}$ given in Table 2 for both studies are plotted versus L_a/B_c in Figure 4. From this Figure the following classification for L_a/B_c and $[Z_c/y]_{opt}$ can be proposed for the present study:

$$[Z_c/y]_{opt} = 0 \quad \text{for } L_a/B_c \leq 2.0$$

$$-0.47 \leq [Z_c/y]_{opt} \leq -0.24 \quad \text{for } 2.0 < L_a/B_c < 5.0$$

$$[Z_c/y]_{opt} = -0.47 \quad \text{for } 5.0 \leq L_a/B_c \leq 14.0$$

And for the Kayatürk's one (2005):

$$[Z_c/y]_{opt} = 0 \quad \text{for } L_a/B_c < 2.0$$

$$-0.50 \leq [Z_c/y]_{opt} \leq -0.25 \quad \text{for } 2.0 \leq L_a/B_c \leq 3.0$$

$$[Z_c/y]_{opt} = -0.50 \quad \text{for } 3.0 < L_a/B_c \leq 14$$

The above relations are valid within the range of L_a/B_c between 0.75 and 14.

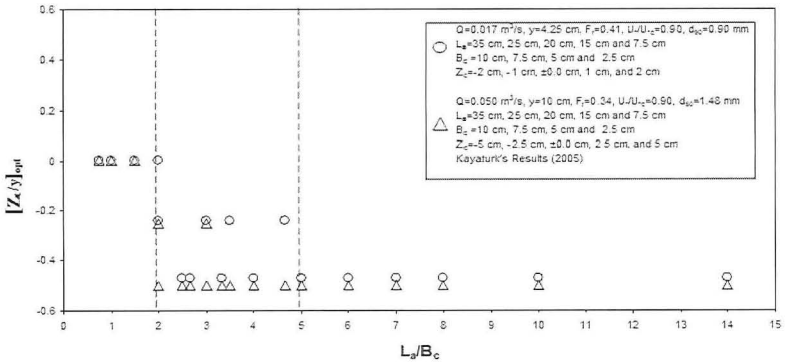


Figure 4. Variation of $[Z_c/y]_{opt}$ with L_a/B_c

Figure 5 shows the variation of $[\%Reduction]_{opt}$ with L_a/B_c (Table 2) for the data of both studies. In the figure it is seen that the best fit lines drawn for all data sets almost coincide to each other. This means that after determining the optimum location of the collar from Figure 4 for a given L_a/B_c , one can also estimate the corresponding $[\%Reduction]_{opt}$ from Figure 5. Consequently, the scour reduction percentages for both sediment sizes are very close to each other. Referring to this figure it can be concluded that to have at least 20% reduction in the maximum scour depth around an abutment, the L_a/B_c value of the abutment must be less than 6, while this value would be less than about 2 to have at least 60% reduction for the Kayatürk's data set (2005). The results for the present data set are almost the same.

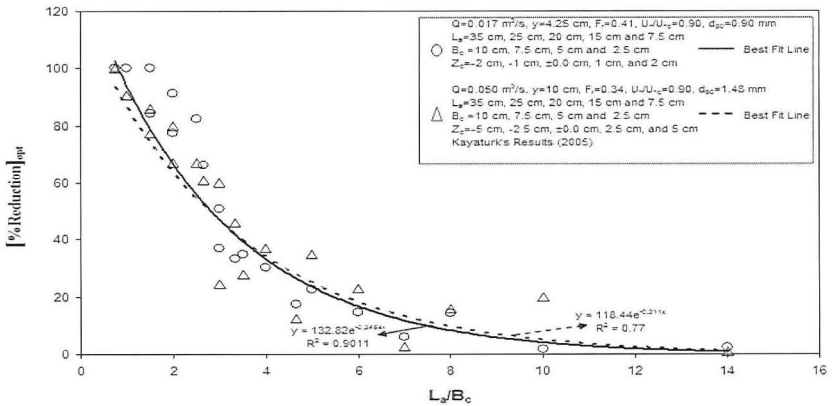


Figure 5. Variation of $[\%Reduction]_{opt}$ with L_a/B_c

CONCLUSIONS

A collar reduces the sediment particles at the bottom of an abutment from erosion by down flow. The efficiency of a collar for reducing scour is a function of its size and its vertical location on the abutment. As the size of the collar increases the scour depth decreases. But, increasing abutment lengths reduce the performance of a collar.

In Kayatürk's study (2005), if $L_a/y > 1$, the efficiency of the collar increases with decreasing L_a/B_c . Also, the elevation of the collar shifts in downward direction from the bed level for increasing L_a/B_c , as long as the clear water flow conditions are satisfied, regardless of the flow depth, that is $U^*/U_{*c} = 0.90$. If $L_a/y < 1$, the collar, which is placed at the bed level ($Z_c/y = \pm 0.00$), gives higher performance than those having other Z_c/y values. In this study, all of the experiments satisfy the condition of $L_a/y > 1$ for all the abutment lengths, which were used. Accordingly, the result derived by Kayatürk (2005) is also satisfied by the results of this study. In other words, according to the general trends of the data presented in Figures 4 and 5, the experiments conducted with a grain size diameter of 0.90 mm provide almost the same results of the experiments conducted with a grain size diameter of 1.48 mm by Kayatürk (2005). In both studies the optimum location of the collar on the abutment, $(Z_c/y)_{opt}$, which will yield the maximum reduction in the scour depth is almost the same for a given L_a/B_c within the ranges tested.

Consequently, it can be stated that the findings of the present study verify that the results of the previous investigation are valid. In order to state a final conclusion about the validity of these findings for other sediments having median diameters different than those; 0.90 mm and 1.48 mm, the similar experiments should be repeated with different erodible material and abutments longer than those used in this study.

REFERENCES

- Borghei, S. M., and Nazari, A., (2004). "Experimental Investigation of Sediment Pattern in River Confluence." *6th International Civil Engineering Conference*, Isfahan Technical University, Isfahan, Iran: 247-255.
- Chiew, Y. M., (1992). "Scour Protection at Bridge Piers." *J. of Hydr. Eng.*, Vol. 118, No. 9: 1260-1269.
- Dargahi, B., (1990). "Controlling Mechanism of Local scouring." *J. of Hydr. Eng.*, Vol. 116, No. 10: 1197-1214.
- Kandasamy, J. K., and Melville, B. W., (1998). "Maximum Local Scour Depth at Bridge Piers and Abutments." *J. of Hydr. Eng.*, Vol. 36, No. 2: 183-198.
- Kapoor, B. S., and Keana, C. M., (1994). "Experimental Overview to Mechanism of Scour Around A Round Nosed Pier and Effect of Delta Wing like Device on Scour Pattern Around It." *Modeling, Measurement & Control C: Energetics, Chemistry, Earth, Environmental & Biomedical Problems*, v46, Issue number: n3, 1994: 25-44, AMSE Press, Tassin-la-Demi-Lune, Fr.
- Kayatürk, Ş.Y., (2005). "Scour and Scour Protection at Bridge Abutments." *Thesis presented to Middle East Technical University*, Ankara, Turkey, in partial fulfillment of the requirements for the degree of Doctor of Philosophy.

- Kumar, V., Raju, K. G. R., and Vittal, N., (1997). "Reduction of Local Scour Around Bridge Piers Using Slots and Collars." *J. of Hydr. Eng.*, Vol. 125, No. 12: 1302-1305.
- Li, H., Kuhnle, R. A., and Barkdoll, B. D. (2006). "Countermeasures Against Scour at Abutments." *National Sedimentation Laboratory*, Research Report No. 49, U.S.
- Mashahir, M. B. and Zarrati, A. R., (2002). "Effect of Collar on Time Development of Scouring around Rectangular Bridge Piers." *The 5th International Conference on Hydro Science and Engineering*, Warsaw, Poland.
- Melville, B. W., (1992). "Local Scour at Bridge Abutments." *J. of Hydr. Eng.*, Vol. 118, No. 4: 615-631.
- Oliveto, G., and Hager, W. H., (2002). "Temporal Evolution of Clear-Water Pier and Abutments Scour." *J. of Hydr. Eng.*, Vol. 128, No. 9: 811-820.
- Parker, G., C. Toro-Escobar, and R.L. Voight, Jr., (1998). "Countermeasures to Protect Bridge Piers From Scour" User's Guide, Vol. 1, *prepared for National Cooperative Highway Research Program, Transportation Research Board, National Research Council, NCHRP Project 24-7*, St. Anthony Falls Laboratory, University of Minnesota, Minneapolis, MN (revised 7/1/99).
- Singh, C. P., Setia, B. and Verma, D. V. S., (2001). "Collar-Sleeve Combination as a Scour Protection Device Around a Circular Pier." *XXIX IAHR Congress Proceedings*, Beijing, China, Vol. 2: 202-210.

ASSESSING BRIDGE VULNERABILITY AND RISK DUE TO STREAM INSTABILITY

P.A. Johnson¹ and R.M. Whittington²

¹Professor and Head, Dept. of Civil and Environmental Eng., 212 Sackett Bldg., Penn State University, paj6@psu.edu; 814-863-3084

²Graduate Student, Dept. of Civil and Environmental Eng., 212 Sackett Bldg., Penn State University, mmw5023@psu.edu; 814-863-3084

ABSTRACT

The FHWA recommends that stream stability analyses begin with a Level 1 assessment. Following data collection and observations at the bridge, the user must determine whether the relative risk is low or not. If it is low, then no action is needed. If the risk is greater than low, then a Level 2 analysis is recommended. In this paper, the relative risk of failure due to stream channel instability at a bridge is assessed as a simple function of vulnerability and criticality. Vulnerability is based on a stream stability assessment and the National Bridge Inventory (NBI) ratings for channel condition for a particular bridge. Criticality is determined indirectly as a function of the bridge importance, using data extracted from the NBI. Relative risk is then qualitatively determined by combining vulnerability and criticality. An example is provided in which the relative level of risk is used to determine the need for a Level 2 analysis.

INTRODUCTION

Bridge scour, including pier, abutment, and contraction, have been heavily researched over the past several decades. Relatively simple equations have been developed to estimate scour depths, although much work still remains to refine those equations and improve confidence. Stream instabilities, such as widening, lateral migration, and downcutting, on the other hand, have received less attention in the scour literature for various reasons. The Federal Highway Administration's manual for assessing stream stability, HEC-20 (Lagasse et al., 2001), recommends that stream stability analyses begin with a Level 1 assessment. Following data collection and observations at the bridge, the user must determine whether the risk is low. If so, then no action is needed. If the risk is greater than low, then a hydrologic, hydraulic, and scour analysis is needed (Level 2). However, no method is given for determining the level of risk, even in a relative sense. Thus, a systematic approach to this decision-making process is needed to provide sufficient justification to decide whether the risk is low or otherwise. Given the importance of stream channel stability to the safety of bridges over water, the difficulty in assessing or quantifying stream channel stability, and the expense of conducting full hydrologic, hydraulic, and scour studies, this study focuses on the use of a simplified assessment to determine the relative risk of bridge loss due to stream channel instability as a basis for making this important decision. Data from the National Bridge Inventory, as well as a stream stability assessment, are used.

ASSESSING STREAM CHANNEL STABILITY

Based on substantial field observations, Johnson (2006) described the characteristics of bridge-stream intersections across the United States and developed recommendations for addressing and improving channel stability at bridges, including: (1) controlling water and sediment discharges at the catchment level; (2) revegetating channel banks with woody vegetation; (3) reshaping the channel cross-section to a more stable, configuration; (4) removing disturbances from the stream channel, such as cattle and (5) using structures to control flow near channel beds and banks. Johnson found that the physiographic setting of the bridge-stream intersection is a factor in the solution of at least the first three suggestions in this list and suggested that attention to the physical characteristics of bridge-stream intersections in the various physiographic regions can lead to sustainable solutions for stabilizing channels at bridge-stream intersections

The Federal Highway Administration's Hydraulic Engineering Circular 20 (HEC-20) (Lagasse et al. 2001) provides guidelines for bridge owners and inspectors to assess channel stability and potential stability-related problems in the vicinity of bridges and culverts. A three-level approach is suggested. If the results of the qualitative Level 1 assessment suggest that the channel may be unstable in either the vertical or lateral direction, then the user is guided to continue to the more quantitative Level 2. Based on those results, the user may or may not be instructed to continue to Level 3. To assist in the determination of the need to go on to Level 2 in HEC-20, Johnson et al. (1999, 2005) developed a rapid stability assessment method based on geomorphic and hydraulic indicators that have been included in the most recent revision of HEC-20. This method is based on observations at bridges in 13 physiographic regions of the continental United States. The method provides an assessment of channel stability conditions as they affect bridge foundations. It is intended as a rapid assessment of conditions for the purpose of documenting conditions at bridges and for judging whether more extensive geomorphic studies or complete hydraulic and sediment transport analyses are needed to assess the potential for adverse conditions developing at a particular bridge in the future, as advised in the Federal Highway Administration guidelines (see Lagasee et al., 2001).

RELATIVE VULNERABILITY AND RISK

Vulnerability indices (VI) and vulnerability assessments have been developed for a variety of purposes and have been used by several U.S. government agencies to rank and assess a wide variety of threats, both natural and human. In this paper, vulnerability is assessed using data from the National Bridge Inventory along with ratings of stability from the stream channel stability assessment method developed by Johnson (2005) to provide a current picture of the state of the stream channel in the vicinity of the bridge. The most relevant NBI data is the Channel Condition (Item 61 in the FHWA coding system (FHWA, 1995)). The rating for channel condition ranges from 0-9, with 0 the worst condition (bridge closed because of channel failure) and 9 being the best condition (no noticeable or noteworthy deficiencies). The reason to use both the stability assessment rating as well as the NBI rating is that they are based on

different sets of factors, thus giving a more complete picture of the overall condition. In the stability assessment rating, the higher the resulting rating, the more unstable the channel. For the NBI items, the higher the number, the better the conditions are at the bridge. Given this difference in ratings and also given that the factors scaled differently, the ranges of values for each factor were reduced to similar scales.

Using the reduced ratings, the vulnerability was computed. The resulting vulnerability is categorized as given in Table 1.

Table 1. Categories of vulnerability.

Category	Description
Low	A loss event due to stream channel instability is unlikely.
Moderate	Given continuing stream conditions, a loss event occurrence is moderate and more likely to occur than not.
High	Continuing stream instabilities will likely cause a significant loss event.
Very High	Given the current conditions, continuing stream instability will almost certainly lead to a loss event.

Criticality is defined here as the impact or consequences of loss. In risk analyses, losses are typically quantified in terms of costs, such as costs associated with loss of life, replacement costs, costs of services interrupted, and environmental costs. However, for the purpose of deciding on the need to conduct a Level 2 analysis, relative risks are sufficient. Thus, criticality was assessed in this study using NBI data as surrogates for costs, as these data are readily available. NBI items that are related to costs (Stein et al., 1999), and thus criticality, include detour length, functional class, average daily traffic (ADT), number of spans, structure length, and overall width. As with the vulnerability factors, the criticality factors have different units and ratings. In order to have consistent scales, the criticality factors were transformed to reduced scales. The categories of criticality are given in Table 2.

Table 2. Categories of criticality.

Category	Description
Low	Costs of failure are low.
Moderate	Costs of failure are moderate.
High	Overall loss is high and somewhat costly.
Very High	Overall loss is very high and costly.

Combining the vulnerability and the criticality leads to a relative approximation of risk. A risk and decision matrix can then be constructed based on these factors. The result is a matrix of decisions, including: (1) the levels of vulnerability and loss are too high to ignore and must be made a high priority to be controlled or eliminated; (2) the risks may be unacceptable, however, following further investigation, the bridge owner may choose to accept these risks; and (3) these risks may be accepted upon the bridge owner's review.

EXAMPLE USING RISK-LOGIC MATRIX FOR DECISION-MAKING

As an example of using the method described in this paper, a bridge over Bentley Creek in north-central Pennsylvania is presented, along with the results of the vulnerability, criticality, and risk-logic decision. The Bentley Creek watershed lies within the glaciated Appalachian Plateau physiographic region of north-central Pennsylvania in the Susquehanna River Basin. The channel bed material is primarily gravel and cobbles. The stream banks are noncohesive sand and gravel. In 1972, Hurricane Agnes destabilized large portions of the channels in the watershed, causing a significant increase in bank erosion and subsequent movement of large quantities of sediment through the channel. In addition, the channel was straightened along several reaches to facilitate road construction. As a result, the channels were further destabilized and erosion rates continued to increase. To maintain flood flow through the bridge openings along the channels, the Pennsylvania Department of Transportation dredges the area beneath and immediately upstream of the bridges, creating a potential sediment trap during subsequent high flow events. Sediment has been observed to accumulate beneath one of the two-span bridges to a depth of more than 1.5 meters during a single storm, nearly filling the left span with sediment. Because most overbank flood events deposit an abundance of material beneath the bridges, dredging must be conducted on almost an annual basis at the majority of the six bridges along Bentley Creek. Upstream, channel degradation and bank erosion are actively occurring. The eroded sediment is then carried downstream where it deposits at the bridges because of gentler gradients and backwater conditions during high flows. The specific bridge used in this example is PA Route 4013 over Bentley Creek about 0.8 km south of the town of Bentley Creek in Bradford County.

According to a stability assessment and other relevant factors and Table 1, the Bentley Creek bridge has a Very High vulnerability rating due to a highly unstable channel, a meander bend at bridge, continued dredging, and a poor stability assessment rating. Based on Table 2, the criticality is determined as moderate. This is primarily due to a moderate ADT (average daily traffic) and a long detour length. For a very high vulnerability and moderate criticality, the risk-logic matrix yielded a level 3A, meaning that the levels of vulnerability and loss are too high to ignore and must be made a high priority to be controlled or eliminated. Thus, the decision for a HEC-20 Level 1 analysis is that the relative risk is greater than low and, thus, a Level 2 analysis is required.

CONCLUSIONS

In this paper, a method was described to systematically document the factors related to risk and provide justification for the need for a Level 2 analysis using HEC-20 for stream channel stability considerations. The analysis was completed for a bridge in Northern Pennsylvania where channel stability problems threaten the sustainability of the structure. The results showed that the combination of a moderate ADT, a long detour length, and a highly unstable channel resulted in a high level of risk, thus providing a compelling argument for a Level 2 analysis. The majority of data used in this analysis are readily available. The stream stability assessment needed to determine vulnerability is based on a rapid assessment method provided in HEC-20 and Johnson (2005).

REFERENCES

- Federal Highway Administration (1995). Recording and Coding Guide for the Structure Inventory and Appraisal of the Nation's Bridges. Report No. FHWA-PD-96-001. U.S. Department of Transportation, Washington, DC. <http://www.fhwa.dot.gov/BRIDGE/mtguide.pdf> (Last accessed Nov., 2009).
- Johnson, P.A. (2006). Physiographic characteristics of bridge-stream intersections. *River Research and Applications*, 22(2006), 617-630.
- Johnson, P.A. (2005). Preliminary assessment and rating of stream channel stability. *Journal of Hydraulic Engineering*, 131(10), 845-852.
- Johnson, P. A., Gleason, G., and Hey, R. D. (1999). Rapid assessment of channel stability in vicinity of road crossing. *Journal of Hydraulic Engineering*, 125(6), 645-651.
- Lagasse, P. F., Schall, J. D., Johnson, F., Richardson, E. V., Richardson, J. R., and Chang, F. (2001). *Stream Stability at Highway Structures*, Third Edition. Report No. FHWA-IP-90-014, HEC-20-ED-2, Federal Highway Administration, Washington, D.C.
- Stein, S.M., Young, G.K., Trent, R.E., and Pearson, D.R., (1999). Prioritizing scour vulnerable bridges using risk, *Journal of Infrastructure Systems*, 5(3), 95-101.

Evaluation of Sedimentation History of Sandbars at Entrance of Lake Tofutsu, Hokkaido, Japan, by MASW Technology

Yoichi Watabe¹ and Shinji Sassa²

¹Leader, Soil Mechanics and Geo-environment Research Group, Port and Airport Research Institute, 3-1-1, Nagase, Yokosuka 239-0826, Japan; watabe@ipc.pari.go.jp

²Senior Researcher, Soil Mechanics and Geo-environment Research Group, Port and Airport Research Institute, 3-1-1, Nagase, Yokosuka 239-0826, Japan; sassa@ipc.pari.go.jp

ABSTRACT

A significant development of sandbars can be seen at the entrance of Lake Tofutsu, one of the lagoons located along the Okhotsk Sea in Hokkaido, Japan. The purpose of this study is to investigate the sequential sedimentation history of these sandbars. We examined the shear-wave velocity and stiffness structures of these sandbars using a surface wave method called the multichannel analysis of surface waves (MASW) in order to identify and describe the stratigraphy of the sediments at the entrance of Lake Tofutsu. We discovered that even though the sandbars appear to be composed of the same sandy material, the subsoil under the sandbars has a very varied sedimentation stratigraphy, consisting of muddy soil derived from the upstream of the lake and sandy soil derived from the coastal sand of the Okhotsk Sea. On the basis of the shear-wave velocity structure obtained in this study, we successfully determined the sequential sedimentation process.

INTRODUCTION

A significant development of sandbars can be seen at the entrance of Lake Tofutsu (Figure 1), one of the lagoons located along the Okhotsk Sea in Hokkaido, Japan. This entrance is located at 43° 57' 10" N and 144° 21' 34" E. It is speculated that the sandbars have developed because of the transportation of sediments from the river mouth by the back current of the river. The dike at the river mouth was straightened using a sheet pile wall more than 10 years ago in order to prevent erosion; hence, a back current tends to be created more easily when a storm occurs during a flood tide. If the lake entrance is blocked by sandbars, there is a risk that fishing boats will not be able to pass through it. In addition, the lake environment may be damaged by the rise in the water level, desalination of the lake water, blocking of the fish-way, and declining water quality, despite Lake Tofutsu being registered with the Ramsar Convention.

The formation and migration of sandbars have conventionally been studied by hydrodynamic approach. However, Sassa and Watabe (2009) demonstrates that the sandbar morphodynamics are in fact the interplay between hydrodynamics and geodynamic effects, which are reflected in their sedimentation history. The objective of this study is to identify and describe the sedimentation history, which should be the consequence of erosion and sedimentation of the sandbars, in order to understand the sequential sedimentation process. This can be achieved by applying

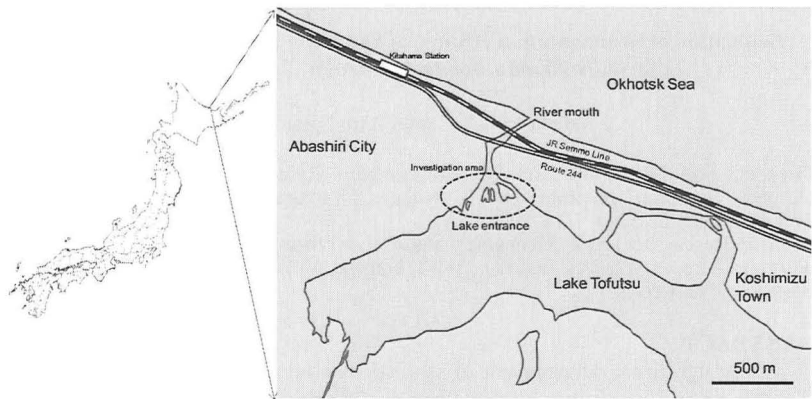


Figure 1. Map of Lake Tofutsu.

multichannel analysis of surface waves (MASW) technology, a useful technology for geophysical exploration.

The MASW technology used in this study was developed by Park et al. (1999) and Hayashi and Suzuki (2004). The authors have applied MASW technology to various types of intertidal flats such as sandy, muddy, and sand-mud layered flats, and have confirmed that this technology is very useful for efficiently surveying the stratigraphy of various types of intertidal flats (Watabe and Sassa, 2008).

SITE INVESTIGATION

MASW was performed on the sandbars during a low-tide period when the sandbars were exposed in the spring tide on July 3 and 4, 2008. Along the Okhotsk Sea in Hokkaido, tidal variation is characterized by diurnal fluctuation as opposed to semidiurnal fluctuation during a spring tide. The diurnal difference between high and low tides at the Okhotsk Sea around the site was approximately 1.4 m; however, the diurnal difference in Lake Tofutsu is smaller because of the bottleneck effect at the lake entrance.

The location of the entrance of Lake Tofutsu is shown in Figure 1. The distance from the lake entrance to the river mouth is approximately 400 m. A railway and roadway were constructed on the coastal sand bank, which is situated between the sea and the lake. The MASW surveys were conducted along arrays A–F on the sandbars at the lake entrance, as shown in Figure 2. The arrays were mainly along the longitudinal direction of each sandbar; a part of array B was along the transverse direction of the corresponding sandbar. The outlines of both grassy areas and the sandbars at the low-tide period were obtained using global positioning system (GPS) measurement; these outlines are shown in Figure 2. In addition, the elevations along the arrays were leveled, and the results were reflected in the figures of the shear-wave velocity structure. Array C was located in a small rise with grasses, and array E was located in a small paddock on the lakeside.

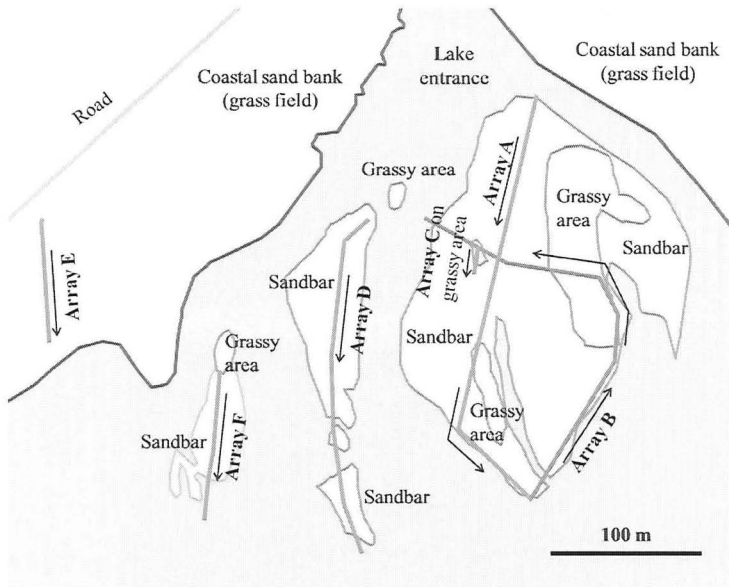


Figure 2. Exposed area of sandbars at lake entrance and arrays for MASW measurement.

The measurement principle of the MASW and the instruments (seismograph: McSEIS-SXW, OYO Corporation, Tokyo, Japan; geophone: GS-11D, OYO Geospace Corporation, Houston, Texas, USA) used in the present study are schematically illustrated in Figure 3. At the site, we used a land streamer (Inazaki, 1999) comprising 24 geophones on aluminum plates aligned in series at 1-m intervals along two parallel ropes on the ground surface. Prior to each measurement, the land streamer was moved by a distance of 4 m. A large portable wooden hammer was used to impose a vertical force on the soil surface at a distance of 0.5 m from the end of the land streamer, thereby triggering Rayleigh waves in the soil. The propagation of the surface waves thus generated in the soil resulted in the propagation of high-frequency short-wavelength waves in the shallow soil region and low-frequency long-wavelength waves in both the shallow and deep portions of the soil, as is characteristic of Rayleigh waves. The propagation of the Rayleigh waves was measured using the aligned geophones.

The scenes typical of the MASW measurements carried out in this study are shown in Figure 4. The photograph shown in Figure 4(a) depicts the moving of the land streamer and leveling of the ground surface and that shown in Figure 4(b), the triggering of the Rayleigh waves using a wooden hammer.

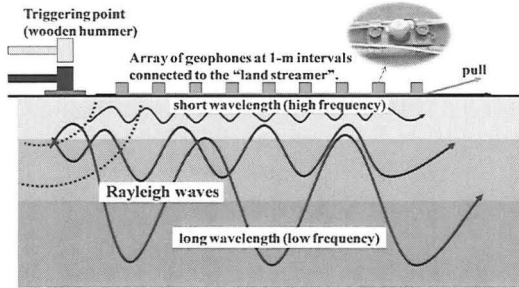
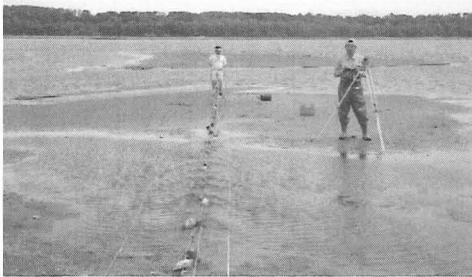


Figure 3. Measurement principle of MASW.



(a) Moving of land streamer and leveling of ground surface (array D).



(b) Triggering of Rayleigh waves using a wooden hammer (array A)

Figure 4. Typical scenes of MASW measurement.

The shear-wave velocity structure can be estimated by the inverse analysis of the various propagation velocities corresponding to the frequencies. In this survey, we obtained the spatial distributions of the surface-wave velocities in the soils and used them to assess the stiffness structures of the sediments under the sandbars. The typical wave patterns corresponding to the various soil types and the algorithm in the calculation are not described here because these details have already been provided

in the study by Watabe and Sassa (2008).

RESULTS

The shear-wave velocity structures obtained along the survey arrays are shown in Figure 5. The surface morphology reflects the results of leveling. The shear-wave velocity v_s can be converted to the initial (maximum) shear modulus G_0 by using the following equation:

$$G_0 = \rho_t \times v_s^2 \quad (1)$$

where ρ_t is the bulk density. Equation 1 indicates that high and low surface-wave velocities correspond to high and low soil stiffness, respectively. It should be noted that the MASW measurement could not be conducted between 165 and 185 m along array D because this region was submerged at a certain water depth with a strong current; this can be observed in the exposed sandbar regions in Figure 2 and in the photograph shown in Figure 4(a).

The shear-wave velocity structure at 0–130 m along array D on a sandbar is similar to that along array E on the lakeside. Both the regions exhibit a shear-wave velocity of 200–250 m/s, indicating that the deposit consists of slightly dense and stiff sand. This fact indicates that these regions had been a part of the coastal sand bank. Therefore, it can be hypothesized that the region at 0–130 m along array D had been connected to the mainland, even though this region is a part of a sandbar that is separated from the mainland today.

The regions where the deposits are very soft from the surface to the deep portion provide evidence of previous water channels; these regions are at 125–175 m along array A, at around 100–200 m along array B, at 150–225 m along array D, and at 20–90 m along array F. The regions along arrays A, D, and F have very soft deposits and a shear-wave velocity lesser than 100 m/s, whereas the region along array B does not have such soft deposits and has a shear-wave velocity of around 150 m/s. These facts indicate that the former are clayey deposits derived from the upstream of the lake, and the latter is a silty sand deposit transported from the river mouth by the back current.

The shear-wave velocities at around a 2-m depth at 0–175 m along array A; at around a 4-m depth at 175–300 m along array A; at around a 4-m depth at 0–50 m, 125–175 m, and 250–275 m along array B; at around a 4-m depth at 175–225 m along array D; at around a 4-m depth at around 0 m on array F; and at around a 2-m depth at 50–75 m along array F indicate that the soils at these depths are stiffer than those at greater depths. These stiffer soils are an evidence of sand layers or oyster mats. In fact, several oyster shells were found when the deposits under the lake were excavated.

The shear-wave velocities at the shallower depths along array C are as low as approximately 80 m/s; however, it is notable that those at the surface are as high as approximately 150 m/s. This fact indicates that the sand on the surface is well-compacted.

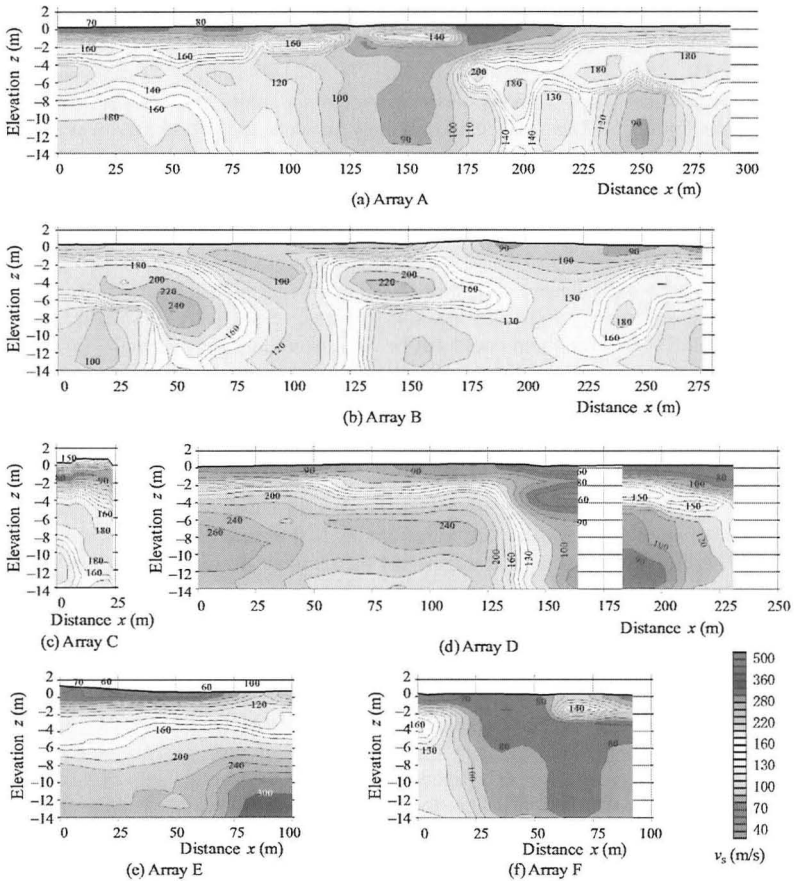


Figure 5. Shear-wave velocity structures obtained by MASW measurement along the survey arrays.

The shear-wave velocity distribution at a 0.5-m depth along the arrays is indicated by color gradation in Figure 6. All the shear-wave velocities at the sandbar surfaces are evaluated to be lesser than 100 m/s. It is notable that the surface grasses have no significant effect on the shear-wave velocity distribution. The shear-wave velocity distribution at a 5.5-m depth along the arrays is shown in Figure 7. In the southern regions of arrays A and B and in the northern region of array D, the deposits are slightly stiffer and the shear-wave velocities are greater than 200 m/s. Around the center of array A and in the southern regions of arrays D and F, the deposits are very soft and the shear-wave velocities are in the range of 50–80 m/s. These deposits

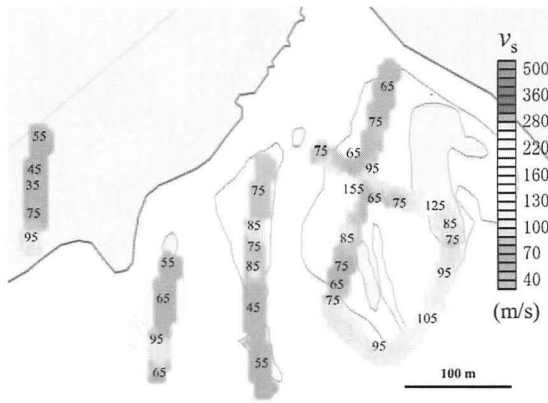


Figure 6. Shear-wave velocity distribution at 0.5-m depth along survey arrays.

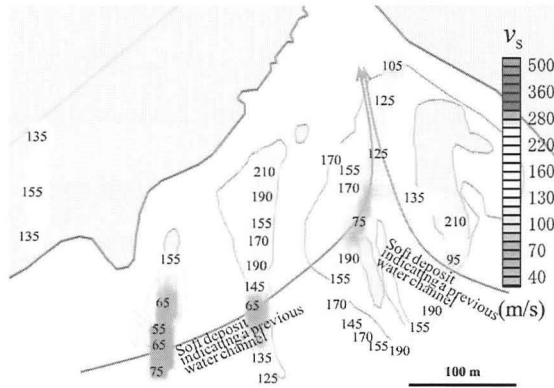


Figure 7. Shear-wave velocity distribution at 5.5-m depth along survey arrays.

indicate that muddy soil was transported from the upstream of the lake, indicating the existence of previous water channels.

All these sandbars appear to be composed of the same deposits with relatively loose and soft sand from the river mouth. However, the shear-wave velocity structure of the sandbars obtained using MASW revealed that these deposits consisted of three layers of different types of soils in a very complicated stratigraphy: (a) dense sand deposited as a coastal sand bank, (b) loose sand rapidly transported from the river mouth by the back current and deposited as sandbars, and (c) very soft muddy soil transported from the upstream of the lake. In other words, even though the sandbars appear to be composed of the same sandy deposit, the subsoil has a very varied stratigraphy.

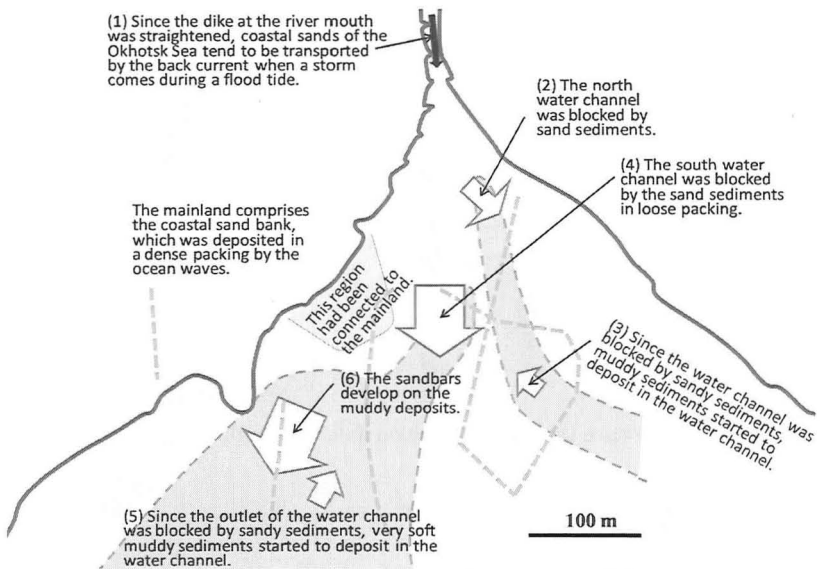


Figure 8. Summary of sandbar formation process at lake entrance.

DISCUSSION: SEDIMENTATION HISTORY AT LAKE ENTRANCE

On the basis of the shear-wave velocity structures obtained by applying MASW on the sandbars during the exposure period, the sedimentation history of the sandbars at the entrance of Lake Tofutsu is discussed in this section. The summary of the sandbar formation process is shown in Figure 8.

The shear-wave velocity structure of the left side sandbar (array D) is very similar to that of the subsoil on the mainland (array E). This fact indicates that these regions are a part of the coastal sand bank, which had stiff deposits and a high shear-wave velocity owing to the effects of ocean waves, currents, and tides. This fact also indicates that the northern region of array D had been previously connected to the mainland as a lakeside.

The two water channels evidenced by MASW in the north and south were very soft from the surface to the deep portion, indicating that the positions of these two water channels were very stable for a long period. This also indicates that appropriate water current to flush away the sediments in the water channels had been maintained from the upstream to the sea through the lake entrance. The positions of the water channels evidenced by MASW are consistent with those observed in an aerial photograph (inset of Figure 9) taken in 1948 before the river mouth dike was straightened.

Since the dike at the river mouth was straightened (Figure 1) about 10 years ago, coastal sands of the Okhotsk Sea tend to be transported by the back current when a storm occurs during a flood tide. Because the back-current velocity suddenly

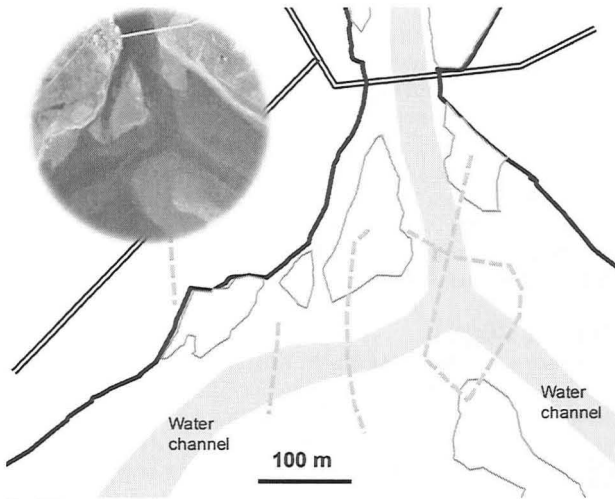


Figure 9. Water channels and sandbars identified in the aerial photograph (inset) taken in 1948.

decreases at the lake entrance where the current is significantly widened, sand particles are rapidly deposited in a loose packing. In fact, the sand deposits are clearly divided into two types: loose and soft deposits corresponding to previous water channels (around 100 m and 200 m on array B) and dense sand deposits corresponding to the coastal sand bank (array E and northern region of array D).

The sands transported by the back current from the coast were first deposited in the north water channel, which was the main stream at that time. Then, the main stream shifted from the north to the south, and consequently, the sands transported by the back current were deposited in the south water channel.

Since the water channels were blocked by the sandbars, muddy sediments transported from the upstream started getting deposited in the previous water channel. The development of the river basin caused a decrease in the river current; this fact should be considered to be a remote cause for the muddy soil deposition.

Presently, the sandbars to the west of the recent main water channel are still developing to upstream of the lake. Consequently, sandbars are developing on the muddy sediments deposited in either the previous water channels or the deeper lake regions seen in array F.

The development of the sandbars is apparently caused only by the sediment transportation by the back current from the river mouth. However, as mentioned above, there is a history of competition between the sandy deposits transported from the coast and the muddy deposits transported from the upstream of the lake. The assessment of the sandbar development on the basis of the MASW results is consistent with an old aerial photograph taken in 1948 (inset of Figure 9) and the memories of the local inhabitants.

SUMMARY

In the present study, MASW technology was applied to investigate the sedimentation history of the sandbars deposited at the entrance of Lake Tofutsu in Hokkaido. The results of this investigation indicate that even though the sandbars are apparently composed of the same sandy deposits, the stratigraphy of the subsoil under the sandbars is considerably different. This reflects the sedimentation history as a competition between the sandy sediments transported from the river mouth and the muddy sediments transported from the upstream of the lake. On the basis of the shear-wave velocity structures obtained using MASW, the sedimentation history of the sandbars was successfully sequenced. The sequenced sedimentation history is consistent with an old aerial photograph and the memories of local inhabitants.

ACKNOWLEDGEMENT

The authors would like to thank Dr. Koichi Hayashi of OYO Corporation for his contribution to the MASW investigation. The field observations were carried out in collaboration with the Abashiri Fisheries Cooperative Association. This study was supported by a Grant-in-Aid for Scientific Research (No. 18360232) from the Ministry of Education, Culture, Sports, Science and Technology, Japan.

REFERENCES

- Hayashi, K. and Suzuki, H. (2004): "CMP cross-correlation analysis of multi-channel surface-wave data." *Exploration Geophysics*, **35**, 7–13.
- Inazaki, T. (1999): "Land streamer: a new system for high-resolution S-wave shallow reflection surveys." *Proceedings of the Symposium on the Application of Geophysics to Engineering and Environmental Problems '99*, 207–216.
- Park, C.B., Miller, R.D., and Xia, J. (1999): "Multichannel analysis of surface waves." *Geophysics*, **64**(3), 800–808.
- Sassa, S. and Watabe, Y. (2009): "Persistent sand bars explained by geodynamic effects." *Geophysical Research Letters*, **36**, L01404, doi:10.1029/2008GL036230.
- Watabe, Y. and Sassa, S. (2008): "Application of MASW technology to identification of tidal flat stratigraphy and its geoenvironmental interpretation." *Marine Geology*, **252**, 79–88.

Instability of Grass caused by Wave Overtopping

Gijs Hoffmans¹, Andre van Hoven², Henk Verheij³

^{1,2,3} Deltares, P.O. Box 177, 2600 MH Delft, The Netherlands
email: gijs.hoffmans@deltares.nl

ABSTRACT

This paper presents a method to deal with the instability of turf in a grass cover that could be considered as an engineering approach, in which both turbulence and two strength models (root model and turf-element model) are discussed in a heuristic way. Turbulence is discussed because of its essential role in erosion. The root model determines the shear strength of rooted soil in the vertical direction. The turf-element model based on a force balance predicts not only the instability of the grass cover but also the initiation of motion of grass. The results of the turf-element model are compared with experimental data of some prototype experiments at Dutch sea dikes.

Introduction

Grass prevents erosion and is an effective control measure. This form of protection has long been used for agricultural drainage channels and on slopes of dikes. In addition, grass-lined emergency spillways are being used as an alternative to costly concrete lining. Following Samani and Kouwen (2002), five methods to evaluate the stability of grass-lined channels have been proposed: maximum permissible velocity, maximum depth, equivalent stone size, permissible tractive force and permissible deflection. All these methods are based on hydraulics, and are probably good enough for steady, uniform flow for the evaluation of roughness coefficients (e.g. Temple 1999). De Baets et al. (2005) investigated the impact of root density and root length density of grass on the erodibility of root-permeated saturated top soils and added this aspect to the available methods based on hydraulics. As hydraulics (load) and geotechnical and vegetation (strength) aspects of the grass cover interact, this requires more insight.

Dutch river dikes usually have clay layers covered with grass on the crest and on both the inner and outer slopes. Sea dikes with hard revetments in the wave impact zone of the seaward slope also have a grass cover on the crest and the inner slope. The grass cover includes grassland vegetation rooted in soil with two layers: the topsoil and the subsoil (Fig. 1, Muijs 1999). The porous turf layer consists of organic matter and sandy clay with a high root density and is elastic in moist conditions. The root structure connects the small clay aggregates and prevents them from being washed out, whereas the underlying clay substrate is stiffer or plastic and less permeable. On the inner slope, the sward contributes to the strength of the grass cover by covering the clay aggregates during overtopping flows, although its contribution to the actual grass strength may be modest. Near the surface, the grass strength is dominated by the root reinforcement, whereas deeper below the surface, where the number of roots decreases rapidly, the soil cohesion and the submerged weight of the soil dominate its strength.

Turbulence

For a grass-clay aggregate, relatively large forces are required to break up the aggregates within the bed, while relatively small forces may suffice to transport pure sand and small clay aggregates. Therefore, at the onset of dislocation, a grass cover or other types of vegetation on dike slopes will experience considerable turbulence, especially at

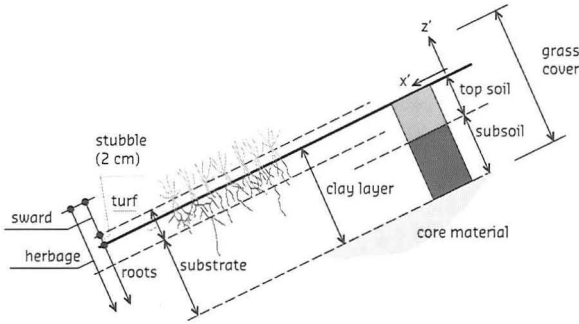


Figure 1. Definition sketch of grass cover (Muijs 1999)

steep slopes. Usually the bed roughness is characterised by the Chézy coefficient (C) as in

$$U_0 = C\sqrt{R_b S_b} \quad (1)$$

in which R_b is the hydraulic radius that may be taken equal to the flow depth (h) for overtopping flow at dikes, S_b is the dike slope and U_0 is the depth-averaged flow velocity. The depth-averaged relative turbulence intensity (r_0) is defined as (Hoffmans 2010)

$$r_0 = \frac{\sqrt{k_0}}{U_0} \quad \text{where} \quad k_0 = \frac{1}{h} \int_0^h (\sigma_u^2(z') + \sigma_v^2(z') + \sigma_w^2(z')) dz' \quad (2)$$

in which k_0 is the depth-averaged turbulence energy and σ_u , σ_v and σ_w are standard deviations of the fluctuating velocities in the streamwise, transverse and normal (z') directions. For uniform flow and hydraulic smooth conditions, Nezu (1977) found $\sigma_u(z') = \alpha_u u_* \exp(-z'/h)$, $\sigma_v(z') = \gamma_v \sigma_u(z')$ and $\sigma_w(z') = \gamma_w \sigma_u(z')$ where u_* is the bed shear velocity, $\alpha_u = 1.92$, $\gamma_v = 0.71$ and $\gamma_w = 0.55$. For channels with smooth and rough bed, the turbulence distributions are reasonable the same (Graf 1998). Substituting these empirical relations in Eq. 2 yields $k_0 = (\alpha_0 u_*)^2$ with $\alpha_0 = [\frac{1}{2}\{1 - \exp(-2)\} \cdot \frac{1}{2}\alpha_u^2\{1 + \gamma_v^2 + \gamma_w^2\}]^{0.5} = 1.2$.

Usually in k - ε models the near bed turbulent energy is defined as $k_b = (u_*)^2 / (c_\mu)^{0.5}$ in which $c_\mu = 0.09$ (e.g. Launder and Spalding 1972). Assuming that $k(z')$ is linear distributed $k_0 = 1.65(u_*)^2$. Since $k(z')$ is an exponential distribution the value of 1.65 is less, so an appropriate value of α_0 for all types of uniform flow is $\alpha_0 = 1.2$. Using the Chézy equation, r_0 is for uniform flow

$$r_0 = \alpha_0 \frac{u_*}{U_0} = \alpha_0 \frac{\sqrt{g}}{C} \quad (3)$$

where g is the acceleration due to gravity. Prototype experiments on different sea dikes using a wave-overtopping simulator [typical wave characteristics are $H_s = 2$ m (significant wave height) and $T_w = 5.7$ s (peak wave period) for a varying dike crest

freeboard] showed that at the inner slope of sea dikes, the steepness of which is about 1V:3H, the maximum depth-averaged flow velocities (U_m) per overtopping event reach values up to 8 m/s (corresponding wave volume per unit width is 5,500 ℓ/m) (Fig. 2). The flow depths vary from 2 cm to 40 cm resulting in high turbulence intensities ($0.1 < r_0 < 0.3$).

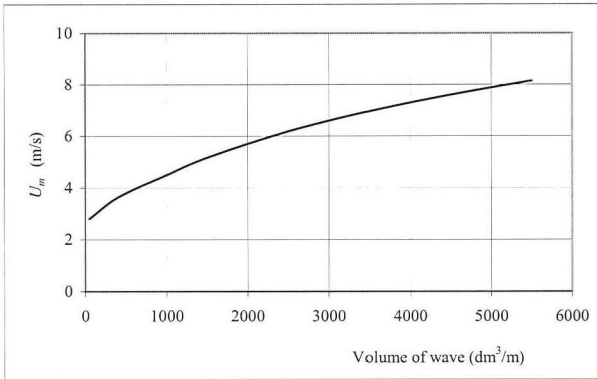


Figure 2. Relation between maximum depth-averaged velocity and wave volume

Emmerling (1973) investigated the instantaneous structure of the pressure near the bed under uniform turbulent flow conditions in air. The frequency (f) of the turbulent wall pressure fluctuations varied from 20 Hz to 2000 Hz and the mean flow velocity in the boundary layer measured 8.5 m/s. Hence, the largest eddies at macro (wave number ($k_w = 2\pi f/U_0$) is 0.15 cm^{-1}) and micro ($k_w = 1.5 \text{ cm}^{-1}$) scale which contribute most to the lift force are considered. The standard deviation of the instantaneous pressure ($\sigma_{p,b}$) on the bed was found to be $3\tau_0$ where τ_0 is the mean bed shear stress and that the maximum pressure fluctuation (p_m) could be up to $6\sigma_{p,b}$. With estimates of $p_m/\sigma_{p,b} = 6$ and $\sigma_{p,b} = 3\tau_0$, p_m can be written as

$$p_m = \alpha_r \tau_0 \quad \text{with} \quad \alpha_r = 18 \quad (4)$$

When grass-clay aggregates are uplifted, p_m represents the maximum lowering of the local pressure caused by eddies. According to Nezu (1977) $\sigma_{p,b}/\tau_0$ depends on the Froude number (Fr). If the turbulent structure is dominated by the Reynolds shear stresses, $\sigma_{p,b}/\tau_0$ is about 3 for $Fr < 0.5$ and $Fr > 2$. At the transition from sub to supercritical flow, $\sigma_{p,b}/\tau_0$ reaches an evident maximum, thus α_r has no universal value. The mean bed shear stress, defined as $\tau_0 = \rho(u_*')^2$, using Eq. 3 reads

$$\tau_0 = \alpha_0^{-2} \rho (r_0 U_0)^2 = 0.7 \rho (r_0 U_0)^2 \quad (5)$$

resulting in $p_m = \alpha_0^{-2} \alpha_r \rho (r_0 U_0)^2 = 12.5 \rho (r_0 U_0)^2$. Based on the above, pressures of about 50 kN/m^2 can be determined for the conditions with overflowing waves. In the next sections the influence of both the dike slope and the slope roughness is included by r_0 [$= \alpha_0 (gh_m S_b)^{0.5} / U_m$ where the maximum flow depth (h_m), U_m and S_b are obtained from measurements per wave volume].

Root model

The Mohr-Coulomb equation describes the shear failure of soil in terms of shear stresses as well as normal stresses and can be written as (e.g. Lambe and Whitman 1969)

$$\tau_s = c_e \cos \phi_e + (\sigma - p_w) \sin \phi_e \quad (6)$$

where c_e is the effective soil cohesion, p_w is the soil pore water pressure, σ is the soil normal stress, τ_s is the soil shear strength and ϕ_e is the effective internal friction angle. The soil cohesion (c) is the result of cementation, weak electrical bonding of clays and organic colloids and capillary tension, whereas ϕ_e represents the frictional interaction of individual particles and the interlocking of particles. The magnitude of σ depends on the weight of the soil and the soil moisture, whereas the buoyancy generated by p_w reduces the normal stress. For dry soil when $p_w = 0$ both $c_e = c$ and ϕ_e equals the internal friction angle (ϕ).

Typically the strength of roots is modelled by an artificial additional cohesion (c_r). In a root permeated soil Eq. 6 can be modified to include c_r

$$\tau_s = c_e \cos \phi_e + c_r + (\sigma - p_w) \sin \phi_e \quad (7)$$

Most attempts to determine the effects of root reinforcement by grassland vegetation have used root-cohesion estimates according to the root equation of Wu et al. (1979), which requires the root tensile strength (σ_r) and the mean root diameter (d_r). Where a root crosses a shear zone, σ_r can be resolved into components parallel (H_r) and perpendicular (V_r) to the shear zone (Fig. 3). Thus, c_r is

$$c_r = \frac{A_r}{A_1} (V_r \tan \theta + H_r) = \sigma_r \frac{A_r}{A_1} (\cos \theta \tan \theta + \sin \theta) \quad (8)$$

where A_r/A_1 is the root area ratio also known as RAR and θ is the angle of shear rotation. Though little is known about θ from field observations of conifers, Wu et al. (1979) suggested a range of 45° to 70° . Since Eq. 8 is insensitive to changes in θ (it is close to 1.2 for a large range of θ), c_r may be rewritten as $c_r \approx 1.2 \sigma_r A_r/A_1$.

Although horizontal roots may have some impacts on the threshold condition for vertical motion, here the vertical grass strength (V_{grass}) and the critical vertical grass strength ($V_{grass,c}$) are approximated by

$$V_{grass} = \sigma_{grass} \cos \theta = \sigma_r \frac{A_r}{A_1} \cos \theta \quad \text{and} \quad V_{grass,c} = \sigma_{grass,c} \cos \theta = \sigma_{r,c} \frac{A_r}{A_1} \cos \theta \quad (9)$$

where σ_{grass} and $\sigma_{grass,c}$ represent the normal grass strength and the critical normal grass strength. Hence, $V_{grass,c}$ does not include the critical friction strength of roots on clay ($c_{grass,c}$). If $c_{grass,c} \ll V_{grass,c}$ all roots are well-anchored and they will all break simultaneously, so they will not be pulled out before breaking owing to a lack of anchoring. However, prototype and laboratory experiments have demonstrated that the roots do not all break simultaneously (e.g. Pollen and Simon 2003) so if deformations are not included Eqs. 8 and 9 overestimate the critical values of c_r and V_{grass} .

The critical tensile strength depends strongly on the type and the quality of the grass. Sprangers (1999) measured grass parameters such as the root length and the dry

root mass densities from 24 Dutch dike sites. He found that A_r/A_1 of dike grassland decreases exponentially with depth and that about 50% of the roots can be found in the top 6 cm of the turf, while about 75% of the roots were located within the top 20 cm. Above $\lambda_{r,cf}$ ($= 10$ cm) about $\frac{2}{3}$ of all roots are to be found. The critical vertical grass strength, which is at maximum near the surface and decreases with depth, is here estimated by

$$V_{grass,c}(z) = \sigma_{0,grass,c} \exp\left(\frac{z}{\lambda_{r,cf}}\right) \cos \theta \quad \text{with} \quad \sigma_{0,grass,c} = \sigma_{r,c} \left(\frac{A_r}{A_1}\right)_0 \quad (10)$$

in which $\sigma_{0,grass,c}$ is the critical normal grass strength near the surface and $(A_r/A_1)_0$ represents the root area ratio close to the surface. For Dutch grasses, the number of roots near the surface lies in the range of 20 to 50 per standard area according to VTV-2006 (or 15,000 per m^2 to 60,000 per m^2). Using $d_r = 0.113$ mm it follows that $0.0002 < (A_r/A_1)_0 < 0.0008$.

Based on Spranger's work, the Dutch guidelines for assessing primary dikes (VTV 2006) distinguish 4 different qualities for the grass cover in which the quality of the grass is strongly correlated to the number (No) of roots. The mean root diameter of Dutch grasses is 0.113 mm (Paulissen 2009), which is significantly finer than the range of d_r tested by the Chinese researchers Chengh et al. (2003). If the following assumptions are made: $d_r = 0.113$ mm, $\sigma_{r,c} = 20 \cdot 10^6$ N/m², $\theta = 45^\circ$, $\phi = 30^\circ$ and $c_{grass,c}$ is neglected with respect to $V_{grass,c}$ then the root properties can be determined (Table 1).

Table 1 Root properties of Dutch dike grassland (near the surface)

Grass quality VTV-2006	⁽¹⁾ (No) ₀ per VTV area	⁽²⁾ $(A_r/A_1)_0$ (-)	⁽³⁾ $(A_r/No)_0$ (mm ²)	⁽⁴⁾ $(A_r/No)_0^{0.5}$ (mm)	⁽⁵⁾ $c_{0,r,c}$ (kN/m ²)	⁽⁶⁾ $\sigma_{0,grass,c}$ kN/m ²
very poor	18	0.0003	39	6	5.7	5.1
poor	26	0.0004	27	5	8.2	7.4
average	53	0.0008	13	4	16.8	15.0
good						

⁽¹⁾ (No)₀ is number of roots per VTV area near the surface;

$(No)_0 = (A_r/VTV/A_1)_{root}$ where A_r/VTV = number of roots near the surface per VTV area which is defined as $\frac{1}{2}n d_b^2$ with $d_b = 0.03$ m and A_1 = root area with $d_r = 0.113$ mm;

⁽²⁾ $(A_r/A_1)_0$ is root area ratio near the surface with $A_1 = 1$ m²;

⁽³⁾ $(A_r/No)_0$ is turf area per root near the surface;

⁽⁴⁾ $(A_r/No)_0^{0.5}$ is root spacing near the surface;

⁽⁵⁾ see Eq. 8 using $\theta = 45^\circ$, $\phi = 30^\circ$, $\sigma_{r,c} = 20 \cdot 10^6$ N/m²;

⁽⁶⁾ see Eq. 9 using $\sigma_{r,c} = 20 \cdot 10^6$ N/m².

Turf-element model

If a grass-clay aggregate with the dimensions of a cube is considered, the following forces acting on this cube can be distinguished: the load due to the lift force caused by pressure fluctuations perpendicular to the grass cover, and the strength, i.e., the submerged weight of the soil, and the forces caused by shear, cohesion and the roots. Figure 4 shows a cube $\ell_x \ell_y \ell_z = \ell^3$ at a horizontal plane where ℓ_x , ℓ_y and ℓ_z are length scales in the x , y and z direction respectively and ℓ is the representative aggregate scale. A grass-clay aggregate is unstable if the load is larger than the strength, thus

$$F_p \geq F_w + F_s + F_c + F_g \quad (11)$$

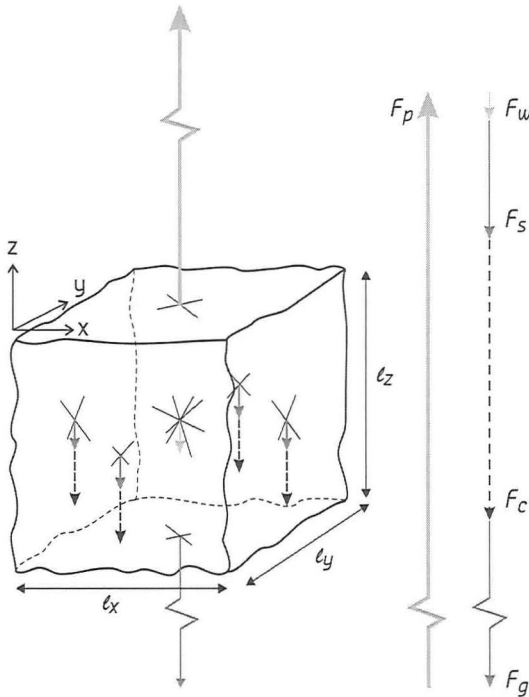


Figure 3. Forces acting upon a turf element

where $F_p [= p_m \ell_x \ell_y]$ is the maximum lift force. The force $F_w [= (1-n)(\rho_s - \rho) g \ell_x \ell_y \ell_z]$ is the submerged weight of the soil [n (≈ 0.4) is the porosity, ρ is the fluid density and ρ_s is the bulk density of soil]. The sum of the shear forces acting on the four sidewalls reads $F_s = \tan \phi (1-n)(\rho_s - \rho) g (\ell_x + \ell_y) (\ell_z)^2$. The sum of the artificial cohesion forces (F_c), which act on the four sidewalls, depends on the critical rupture strength of clay ($C_{clay,c}$) and the critical friction strength of roots ($C_{grass,c}$) averaged over ℓ_z . The sum of the cohesion forces (F_c) is approximated by $F_c = (1-n)(C_{clay,c} + C_{grass,c}) 2(\ell_x + \ell_y) \ell_z$ and the total force at the bottom-element is $F_g = (1-n)(C_{clay,c} + V_{grass,c}(z = -\ell_z)) \ell_x \ell_y$.

The assumption of Eq. 11 is applicable if p_m at the top of the grass-clay aggregate significantly decreases with depth or if the penetration length (ℓ_p) is $\ell_p/\ell \ll 1$. According to De Groot et al. (1996) $\ell_p = (c_v T_p / \pi)^{0.5}$ where c_v is the consolidation coefficient and T_p is the pressure period of the vortices in the turbulent flow at the inner slope of the dike. If the order of magnitude of c_v is $O(c_v) = 10^{-2} \text{ m}^2/\text{s}$ and $O(T_p) = 0.1 \text{ s}$, then $O(\ell_p) = 0.01 \text{ m}$, thus the pore pressure variation equals the total stress variation at a depth larger than one or two times ℓ_p . Based on measured flow fluctuations in open pores of granular filters under uniform and sub critical flow conditions, Klar (2005) found that the turbulence energy at 2 cm below the bed level is about 10% of k_b . Using $\ell_x = \ell_y = \ell_z = -z$, Eq. 11 can be rewritten as

$$p_m \geq V_{soil}(z) = -(1-n) \left[(\rho_s - \rho)(1 + 2 \tan \phi)gz - 4(C_{clay,c} + C_{grass,c}) - (C_{clay,c} + V_{grass,c}(z)) \right] \quad (12)$$

where $V_{soil}(z)$ is the vertical soil strength as function of z . When describing incipient motion, horizontal forces are usually considered. The critical condition for moving grass-clay aggregates is reached if τ_0 equals the critical mean bed shear stress (τ_c). If there is neither clay nor grass and neglecting the shear forces, τ_c of loosely packed materials is ($z = -d$)

$$\tau_0 \geq \tau_c = \Psi_c (\rho_s - \rho)gd \quad \text{with} \quad \Psi_c = \alpha_r^{-1}(1-n) = \gamma_{18}(1-0.4) = 0.033 \quad (13)$$

In turbulent flow, the critical Shields parameter (Ψ_c) varies from 0.03 to 0.06 for coarse sand and gravel, whereas for small Reynolds numbers up to fully laminar flow Ψ_c increases from 0.03 to 0.2. Hence, the first term in Eq. 12 confirms the earlier research of Shields. Substituting $z = -\lambda_{ref}$, Eq. 12 can be rewritten as

$$\tau_0 \geq \tau_c = \Psi_c \left[(\rho_s - \rho)(1 + 2 \tan \phi)g\lambda_{ref} + 4(C_{clay,c} + C_{grass,c}) + (C_{clay,c} + V_{grass,c}(-\lambda_{ref})) \right] \quad (14)$$

Compacted clay has a high resistance against erosion and a low hydraulic conductivity (k) provided the clay is kept in sufficiently moist condition. However, k of a grass-clay aggregate is significantly higher owing to atmosphere, flora and fauna and varies from 10^{-5} m/s to 10^{-4} m/s owing to cracks and other disturbances (Kruse 1998). Hence, near the surface the submerged weight and the rupture strength of clay are negligible with respect to the friction strength of the roots. If $(\rho_s - \rho)(1 + 2 \tan \phi)g\lambda_{ref} \ll C_{clay,c} \ll C_{grass,c}$ then Eq. 14 reduces to

$$\tau_0 \geq \tau_c = \Psi_c (4C_{grass,c} + V_{grass,c}(-\lambda_{ref})) \quad (15)$$

Per sidewall the strength of roots averaged over λ_{ref} is

$$C_{grass,c} = \frac{1}{\lambda_{ref}} \int_{-\lambda_{ref}}^0 V_{grass,c}(z) dz = \alpha_{grass} \sigma_{0,grass,c} \cos \theta \quad (16)$$

where $\alpha_{grass} = 1 - \exp(-1) = 0.64$. Combining Eqs. 10, 15 and 16 yields

$$\tau_0 \geq \tau_c = (1 + 3\alpha_{grass}) \Psi_c \sigma_{0,grass,c} \cos \theta = 2.9 \Psi_c \sigma_{0,grass,c} \cos \theta \quad (17)$$

Assuming that the flow is hydraulically rough, thus $r_0 > 0.05$ and for the condition of incipient motion $r_0 U_0 = r_{0,c} U_c$, the critical depth-averaged flow velocity is

$$U_c = (r_{0,c})^{-1} \alpha_0 \sqrt{(1 + 3\alpha_{grass}) \Psi_c \sigma_{0,grass,c} \cos \theta / \rho} = 2.0 (r_{0,c})^{-1} \sqrt{\Psi_c \sigma_{0,grass,c} \cos \theta / \rho} \quad (18)$$

where $r_{0,c}$ is the critical depth-averaged relative turbulence intensity. When the slope steepness increases or the bed becomes rougher the bed turbulence increases.

Examples of some prototype experiments

At several test locations in the Netherlands (Delfzijl, Boonweg, St. Philipsland, Kattendijke and Afsluitdijk) both the grass and dike core were inspected to determine the grass cover stability and the resistance of the grass to erosion. Different strength parameters were measured, such as the number of roots, soil cohesion, internal friction angle and liquidity index (Van Hoven et al. 2010). The wave-overtopping simulator (Van der Meer, 2007) was used to test the erosion resistance of the inner slope. Experiments were carried out by simulating a six hour storm for every overtopping condition at a constant q . These conditions started with a q of 0.1 ℓ/s per m and increased to 1 ℓ/s per m, 10 ℓ/s per m, 20 ℓ/s per m, 30 ℓ/s per m, 50 ℓ/s per m and 75 ℓ/s per m after testing no significant damage to the grass cover was observed.

The number of roots near the surface varied from 20 to 50 according to the Dutch standard area (VTV 2006). For turbulent flow the boundaries between occasional particle movement at some locations and general transport are $0.03 < \Psi_c < 0.06$. Assuming that $r_{0,c} = 0.17$, $d_r = 0.113$ mm, $\sigma_r = 20 \cdot 10^6$ N/m², $\lambda_{ref} = 0.10$ m and $\theta = 45^\circ$ Eq. 18 gives for poor grass: $4 \text{ m/s} < U_c < 7 \text{ m/s}$, for average grass: $5 \text{ m/s} < U_c < 9 \text{ m/s}$ and for good grass: $U_c > 6.5 \text{ m/s}$ (Table 2). Consequently, all experiments lie in the broad belt originally given by Shields (Fig. 4).

Conclusions and recommendations

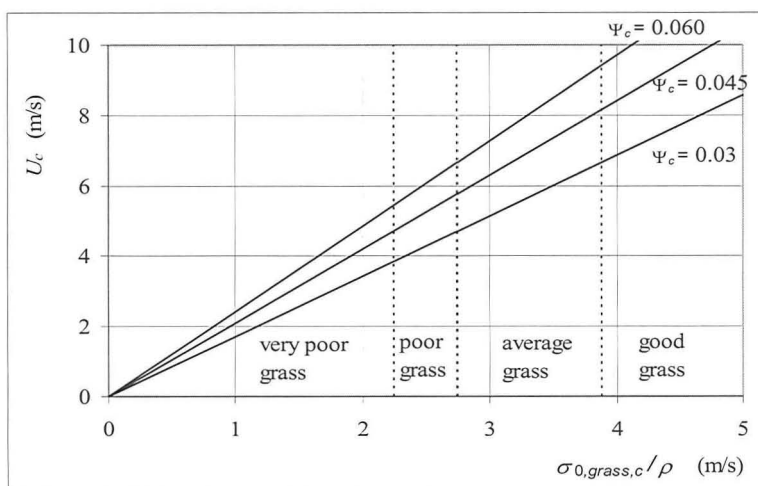
The critical normal grass strength as given in Table 1 is predicted to vary from 5 kN/m² to 15 kN/m² and represents the range of different qualities of grass. The critical vertical grass strength is influenced by No, d_r (= 0.113 mm), $\sigma_{r,c}$ (= $20 \cdot 10^6$ N/m²), λ_{ref} (= 10 cm) and θ (= 45°). Since these parameters can easily be determined to a reasonable degree of precision, the computed value of $V_{grass,c}$ should also be accurate in this respect. However, $V_{grass,c}$ does not include the heterogeneity of the grass cover, e.g., the decrease of d_r with depth and the standard deviations of No, d_r , $\sigma_{r,c}$, λ_{ref} and θ respectively.

Although the modelling is based on physical considerations and should be representative for the strength of the grass cover, the model is based on static equilibrium conditions ($c_{grass,c} \ll V_{grass,c}$). Therefore, it is necessary to examine the deformation of grass as function of the dynamic load, i.e. the relation between $c_{grass,c}$, $V_{grass,c}$ and the elastic modulus for grass, in greater detail and to validate the incipient motion of grass by carrying out sufficient experiments. Moreover, it is recommended to analyse the penetration of the pressure fluctuations close to bed.

The turf-element model should be considered as a conceptual approach, which incorporates a good description of the physics. The model predicts the initiation of motion of turf as an element with a length scale of 10 cm. To update the VTV in 2011 it is necessary to examine the deformation of grass as function of the load and to understand the physical significance of the parameters used in the turf model for different types of grass and clay.

Table 2 Observations and calculations of prototype experiments on Dutch sea dikes

Test location	Experimental programme (discharge in l/s per m)	Observations at inner dike slope	U_m (m/s) (Fig. 2)	Grass quality VTV-2006	U_c (m/s) $\Psi_c = 0.03$	U_c (m/s) $\Psi_c = 0.06$
Delfzijl 1	0,1-1-10-20-30-50	no damage	7	poor	4.0	7.0
Boonweg 1	0,1-1-10-30-50-75	no damage	8	good	6.5	> 10
Boonweg 2	0,1-1-10-30-50-75	no damage	8	good	6.5	> 10
Boonweg 3	0,1-1-10-30-50-75	damage at 75	8	good	6.5	> 10
Boonweg 4	0,1-1-10-30-50-75	damage at 50	7	good	6.5	> 10
St. Philipsland	0,1-1-10-30-50-75	damage at 50	7	good	6.5	> 10
Kattendijke 1	0,1-1-10-30-50-75	no damage	8	good	6.5	> 10
Afsluitdijk 1	1-10-30-50-75	damage at 50	7	average	5.0	9.0

**Figure 4. Critical depth-averaged flow velocity as function of the grass strength****References**

- Akkerman, G.J., Van Gerven, K.A.J., Schaap, H.A., Van der Meer, J.W., 2007. Workpackage 3: Development of alternative overtopping-resistant sea defences, Phase 3: wave overtopping erosion tests at Groningen sea dyke, Rijkswaterstaat, Delft.
- Cheng, H., Yang, X., Liu, A., Fu, H., Wan, M., 2003. A study on the performance and mechanism of soil-reinforcement by herb root system. *Proc. of the 3rd Int. Conf. on Vetiver and Exhibition*, Guangzhou, China.
- De Baets, S., Poesen, J., Gyssels, G., Knapen, A., 2006. Effects of grass roots on the erodibility of top soils during concentrated flows, *Geomorphology*, 76, 54-67.
- De Groot, M.B., Andersen, K.H., Burcharth, H.F., Ibsen, L.B., Kortenhaus, A., Lundgren, H., Magda, W., Oumeraci, H., Richwien, W., 1996. Foundation design of caisson breakwaters, Publication 198. Norwegian Geotechnical Institute, Oslo, Norway.

- Emmerling, A., 1973. Die momentane Struktur des Wanddruckes einer turbulenten Grenzschicht-strömung, Max-Planck-Institut für Strömungsforschung, Bericht 9.
- Graf, W.H., 1998. *Fluvial Hydraulics*, Flow and transport processes in channels of simple geometry, Wiley & Sons, New York.
- Hoffmans, G.J.C.M., 2010. Stability of Stones Under Uniform Flow, *J. of Hydr. Engrg., ASCE*, 136(2), 129-136.
- Klar, M., 2005. Design of an endoscopic 3-D particle-tracking velocimetry system and its application in flow measurements within a grave layer, *Doctoral Thesis*, University of Heidelberg, Germany.
- Kruse, G., 1998. Impact of weathering on resistance of soils, in *Dikes and revetments, Design, Maintenance and Safety Assessment* (edt. K.W. Pilarczyk), Balkema, Rotterdam.
- Lambe, T.W., Whitman, R.V., 1969. *Soil Mechanics*. John Wiley, New York.
- Lauder, B. E., Spalding D.P., 1972. *Mathematical models of turbulence*, Academic Press, London.
- Muijs, J.A., 1999. Grass cover as a dike revetment, Translation of TAW-brochure "Grasmat als Dijkbekleding" 9, Ministry of Public Works and Water Management, Rijkswaterstaat, Delft.
- Nezu, I., 1977. Turbulent structure in open-channel flows, (Translation of Doctoral Dissertation in Japanese), Kyoto University, Kyoto, Japan.
- Paulissen, M.P.C.P., 2009. Personal Communications. Alterra, Wageningen University and Research Centre, The Netherlands.
- Pollen, N.L., Simon, A., 2003. A new Approach for Quantifying Root-Reinforcement of Streambanks: the RipRoot, American Geophysical Union, Fall Meeting 2003, abstract #H52A-1174.
- Samani, J.M.V., Kouwen, N., (2002), Stability and erosion in grassed channels, *J. Hydr. Engrg., ASCE*, 128(1), 40-45.
- Shields, A., 1936. Anwendung der Aehnlichkeitsmechanik und der Turbulenzforschung auf die Geschiebebewegung, *Mitteilungen der Preussischen Versuchsanstalt für Wasserbau und Schiffbau*, Heft 26, Berlin NW 87.
- Sprangers, J.T.C.M., 1999. Vegetation dynamics and erosion resistance of sea dyke grassland, *Doctoral Thesis*, Wageningen Agriculture University, Wageningen, The Netherlands.
- Temple, D.M., 1999. Flow resistance of grass-lined channel banks. *Applied Engineering in Agriculture*, 15(2), 129-133.
- Van der Meer, J.W., 2007. Workpackage 3: Development of alternative overtopping-resistant sea defences, Phase 3: Design, construction, calibration and use of the wave overtopping simulator, Rijkswaterstaat, Delft.
- Van der Meer, J.W. Verheij, H.J., Lindenberg, J., Van Hoven, A., 2007. Wave overtopping and strength of the inner dike slopes; Predictions, [in Dutch], INFRAM, Marknesse, The Netherlands.
- VTV, 2006. Safety assessment of the primary flood defences [in Dutch], Ministry of Transport, Public Works and Water Management, Rijkswaterstaat, Delft.
- Winterwerp, J.C., Van Kesteren, W.G.M., 2004. *Introduction to the physics of cohesive sediment in the marine environment*, Elsevier, Amsterdam.
- Wu, T.H., McKinnell, W.P. III, Swanston, D.N., 1979. Strength of tree roots and landslides on Prince of Wales Island, Alaska. *Canadian J. of Geotechnical Res.* 16(1), 19-33.

Geomorphic and River Channel Stability Assessment of the Merced River at the Ferguson Slide, Mariposa County, CA

Strudley, M.W., Guensch, G.R., Hastings, B.K., Thompson, K., Chartrand, S.M., Roberts, B., Hecht, B.

Abstract On April 29, 2006, the Ferguson Rock Slide covered California Highway 140 with approximately 70,000 cubic meters of material at Ferguson Ridge. Slide debris protrudes into the Merced River and continues to periodically accumulate in and along the river channel. Caltrans has installed temporary detour bridges and proposes to permanently install one of several alternative bridge designs. Balance Hydrologics, under subcontract to Parsons Transportation Group, has conducted a geomorphic and river channel stability assessment to examine the potential effects of the various bridge alternatives on river stability, channel migration, and scour and fill. Here we describe morphologic evaluation of the existing channel and a spatially-distributed incipient motion analysis keyed to geomorphic map units and simulated 2D hydrodynamic river behavior. This work represents a novel and useful approach to assess channel stability at engineered crossings, and provides a much clearer picture of river behavior than typical scour analysis calculations.

Introduction

The Ferguson Rock Slide is located on California State Highway 140, in between the towns of Mariposa and El Portal, a crucial local and regional transportation corridor. Freely-flowing traffic was first disrupted by reactivation of the Ferguson Rock Slide beginning on April 29, 2006. Conditions quickly deteriorated thereafter, and by the end of May 2006, a 600-foot long stretch of Highway 140 was buried in rockfall debris (Harp and others, 2006) and closed indefinitely. Balance Hydrologics, Inc. was asked by Parsons Transportation Group, Inc., on behalf of the California Department of Transportation, to prepare a River Geomorphology Study in support of environmental compliance for transportation restoration of Highway 140 at the Ferguson Rock Slide in Mariposa County, California. To restore reliable freely-moving traffic on Highway 140 Caltrans is considering nine (9) separate project alternatives, including the no build alternative. Six (6) of these alternatives (see Figure 5), Alternatives C, T, S, S2, A, and the No Build (two, one-lane bridges obliquely spanning the Merced River connected by a single-lane roadway opposite the slide mass), are examined in this paper because of their potential to impact Merced River form, function, and recreational whitewater characteristics.

Environmental Setting

The project site is in the Merced River canyon approximately 0.5 miles downstream of the mouth of the South Fork Merced River, a major tributary which has cut a valley with similar morphology to that of the main fork. Drainage area at the project site is 661 square miles (Cipponeri, 2007). Canyon walls composed predominantly of fine-grained phyllite are steep and generally mantled with a thin veneer of sediments that support mesic to xeric vegetation. The Merced River traces

a relatively straight path from the Yosemite Valley area to the Central Valley, and is bedrock controlled. Significant bends are likely a result of active or inactive faults and knickpoints, and changes in structure and lithology. The walls of the valley at the approximate level of the design flood are composed of (a) bedrock, (b) blast rock, (c) imported (and often cemented or fortified) rip rap, (d) vertically-cemented rock walls, and (e) slide debris and derivative talus. All wall types listed are generally stable, with the obvious exception of slide debris. Local intrusions of the Bass Lake Tonalite and the Pilot Ridge Quartzite supplement the predominantly granitic-boulder/cobble bedload of the Merced River derived from glacial deposits and eroded bedrock of the Sierra Nevada batholith farther to the east in the Yosemite area (Beck, 2007a,b; Bateman, 1992). The local climate at the project site is characterized by a wet winter season (October to March) during which approximately 90% of total precipitation falls, and a warm, dry season (May to September) with temperatures which can reach 100°F. Lows during the winter season are generally around 20°F. Mean annual rainfall for the entire Merced River watershed is 42 inches, although higher elevations receive closer to 60 inches annually in the form of snow, while lower elevation areas near the project site receive 37 inches.

Technical approach

Our comprehensive, inter-disciplinary analytical approach is designed to address a number of outstanding questions. First, what constitutes the present-day geomorphic characteristics of the Merced River at the project site? Second, what are the estimated hydraulic characteristics of flood flows at the project site under existing river conditions? Third, under what hydraulic conditions will existing river morphologic features be mobile and subject to adjustment? Last but not least, did the recent episode at the Ferguson Rock Slide affect river morphology and function, and how may subsequent re-activation phases interact with the river, and the potentially implemented transportation alternatives?

To address these queries, we employed several site-specific hydrologic, hydraulic, and geomorphic analyses, including (a) complete historic flow analysis of all locally available USGS gaging data including estimation of the peak flows for the recent floods of 1997 and 2005; (b) geomorphic facies mapping of alluvial deposits through the project reach (to describe present-day river-bed architecture); (c) surface and near-surface sediment grain-size analysis (to characterize the composition of alluvial deposits); (d) quantitative dating of flood deposits and geomorphically-significant surfaces utilizing lichenometry and dendrochronology with results placed in context of historic floods for results validation; (e) development of one- and two-dimensional hydraulic models to verify predicted water surface elevations and profiles against observed high water marks and simulate river hydrodynamics at design flows; and (f) incipient motion or bed mobility analysis.

Hydrologic Analysis

A total of 5 USGS gages with varying periods of record and proximity to the project reach were used to estimate peak discharge values so that design flows could be selected for calibrating simulations to observed high water marks from 1997 and 2005 events. Discharge estimations were complicated by the fact that the gages near

the site have short records ending in mid 1970s and that Pohono gage, with a long continuous record, is located 16 miles upstream. We estimated project reach discharges using ratios of the gage records from near the site to the concurrent data from the upstream Pohono gage. This produced an estimates of 16,500 cfs for the 2005 peak, and 43,250 to 49,250 cfs for the 1997 event.

Geomorphic Facies Mapping

The centerpiece of this study from a geomorphic perspective is our geomorphic facies map of the project reach (Figure 1). This map illustrates the suite of alluvial and colluvial deposits that mantle the bedrock floor and channel margins within the Merced River canyon. It depicts the relative age of each deposit, determined by stratigraphic and onlapping relationships, along with lichenometric and dendrochronometric sampling that provide an approximate absolute age. We also identified and mapped the location of trees and lichen used for absolute dating, large woody debris (LWD) left by flood flows, sediment sampling sites, knickpoints, riffles and pools, and cross section traces where we developed depictions of cross-valley surfaces and features. Geomorphic facies were identified based on grain size, texture, landscape position, degree and age of vegetation development, and topographic correlation across the channel.

Sediment Grain Size Analysis

We focused our grain size sampling at, and adjacent to, the locations of bridge piers in the proposed alternatives. The grain size analysis consisted of: (a) pebble count surveys along linear transects over bar and floodplain surfaces; (b) point-sampling of the bed surface on bars and within the submerged channel; and (c) point-sampling of subsurface (bed core) sediments on bars and within the submerged channel. Transects did not cut across different surfaces. Grains were measured with ruler and tape to half phi-size increments. Point sampling on subaerial and submerged surfaces consisted of placing a 1-meter square grid on the surface and sampling all particles within the grid square at the surface. Once surface particles were removed, subsurface particles were measured, or if the subsurface consisted of a large proportion of fines (gravels and finer, indicating a well-armored surface), an estimate of the modal percentage of fines was made relative to the remaining large particles. Grain size results at the medial bar across from the slide, on the right-side point bar 100 feet downstream and 200 feet upstream of cross section G, and on the left-side bar at cross section F yielded D_{50} values of 136, 256, 107, and 147 mm and D_{84} values of 244, 524, 249, and 318 mm, respectively (Figure 1).

Hydraulic Modeling

The U.S. Army Corps of Engineers (USACE) Hydrologic Engineering Center's River Analysis System (HEC-RAS) was used to conduct the one-dimensional hydraulic modeling for the project reach. Cross sections were extracted from the elevation contour map generated in ArcGIS using GeoRAS. Manning's 'n' values were estimated in the field based on substrate roughness and vegetation characteristics according to established guidelines (Chow, 1959; Haan and others,

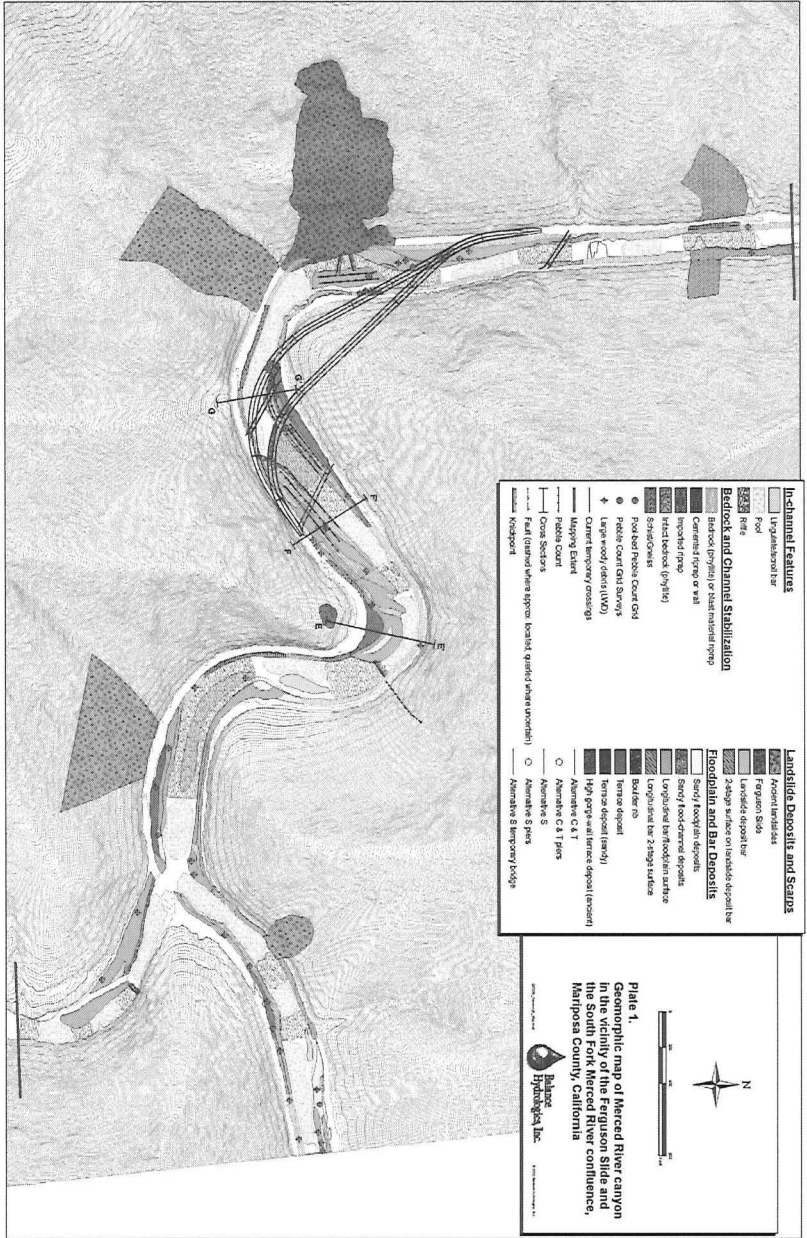


Figure 1. Geomorphic map of Merced River canyon in vicinity of the Ferguson Slide and South Fork Merced River confluence, Mariposa County, CA.

performed by comparing water surface elevations in the 1D HEC-RAS model with those developed in the 2D model.

Sediment Transport

A bed sediment mobility analysis was used to evaluate how the different transportation alternatives may affect sediment mobility relative to existing conditions. The analysis involved determining the dimensionless critical shear stress of the median grain size (D_{50}), which is likely to be mobile under the different transport conditions. We used our 2D hydrodynamic modeling results to generate discrete distributions of boundary shear stress across the study reach, which we then used to calculate a critical median sediment diameter, D_c :

$$D_c = \frac{\tau_0}{\tau_c^* (\rho_s - \rho) g}$$

τ_0 is the applied boundary shear stress, given *a priori* values for the Shields' parameter (dimensionless critical shear stress), τ_c^* , and density of sediment, ρ_s , and water, ρ . (We assume a density of 2.65 g/cm³ for the quartz-rich granitic sediment supply.) We then compared D_c to the median diameter measured in our grain size pebble counts to ascertain stability of the surface. Applied boundary shear stress is calculated using output from the 2D hydrodynamic model:

$$\tau_0 = \frac{\rho \bar{u}^2}{[5.75 \text{Log}(12.27R/k_s)]^2}$$

where \bar{u} is the depth-averaged flow velocity and R is the hydraulic radius (here, flow depth is used as an approximation for R). The term k_s is the boundary roughness length scale, which is generally greater than D_{50} (Buffington and Montgomery, 1997); here we use $k_s = 3.5 * D_{84}$, consistent with HEC-18 (Richardson and Davis, 2001) and others (e.g., Whiting and Dietrich, 1990), where D_{84} is the sediment diameter below which 84% of the sampled grains are finer.

Results

A total of 7 scenarios were run in addition to the natural (no-bridge) condition. As a brief example of this analysis, we present results from the natural condition, and Alternatives C and T, which share the same bridge alignments.

Natural conditions under high flow

Under our modeled high flow condition of 42,000 cfs and with no bridges in place (the "natural condition") the velocity distribution shows high velocity flow through the thalweg, with the highest velocities, shown as dark areas occurring at the bend (Figure 3). The large region of high velocity flow just downstream of the bend is located at the toe of the slide where a rapid has been formed from slide debris. The shear stresses result in critical bed sediment size distributions generally much higher than median sediment sizes sampled on the three bars analyzed. As a result, we

would anticipate that most of the material along channel margins, on the river bed, and on bars not sampled, will be mobile under the simulated high-flow condition. On both the left-bank and right-bank bars upstream, the critical bed sediment sizes generally represent cobbles and boulders (up to ~2000 mm diameter), except along the outside margins of these bars just below adjacent roadways (Highway 140 on the left bank and Incline Road on the right bank). In contrast, critical sediment size distribution on the medial bar across from the slide is much higher, ranging between 1000 – 5000 millimeters. This is a product of the large predicted shear stresses which would be exerted over this bar during the modeled high-flow.

The above shear stress and critical sediment size distributions yield potential incipient motion conditions which would provide for complete mobilization of the river bed and banks within the project reach under high flow conditions with the exception of narrow geomorphically stable deposits along the periphery of the upstream bar deposits.

Alternatives C and T under high flow

Plots of the changes in flow depth, velocity, shear stress, critical grain size diameter, and incipient motion potential between natural conditions and Alternatives C and T under high-flow conditions are shown in Figure 4. The obliquely-oriented bridges for Alternatives C and T create up to 1-foot increases in flow depth upstream of the two crossings that dissipate gradually a few hundred feet upstream of each crossing. The results also show the isolated effects of the piers on water surface elevation and velocity.

Changes in flow velocity are the direct result of flow being channeled through bridge openings, between piers, and between piers and the river banks. Flow velocity increases of up to 1 ft/sec are predicted for flow zones between piers at both the upstream and downstream bridges, while decreases in flow velocity are created at the wakes or eddies downstream of all of the piers. The most significant velocity increase of approximately 3 to 4 ft/sec is shown between the left bank pier of the upstream bridge and the left bank.

The increase in shear stress associated with piers is most pronounced on either side of the right bank pier at the upstream bridge, but shear stress increases are also expected at the downstream piers and in the channel center in upstream reaches, as suggested by the changes to the velocity field in the project reach. Shear stress declines slightly in many locations on the left-bank bar at the upstream bridge, because the backwater effect of the upstream bridge is most pronounced along the left channel margin.

Fields of high critical sediment diameter have contracted slightly for Alternatives C and T, compared to natural conditions. This is a result of decreasing shear stress over much of the project reach under Alternatives C and T compared to natural conditions, except at locations of flow constriction between proposed piers. These reductions in critical sediment diameter yield contracted fields of potentially mobile sediment on bar surfaces, despite the increases in shear stress at localized areas between proposed piers. We still expect sediment in the channel center and around piers to experience enhanced mobilization compared to natural conditions,

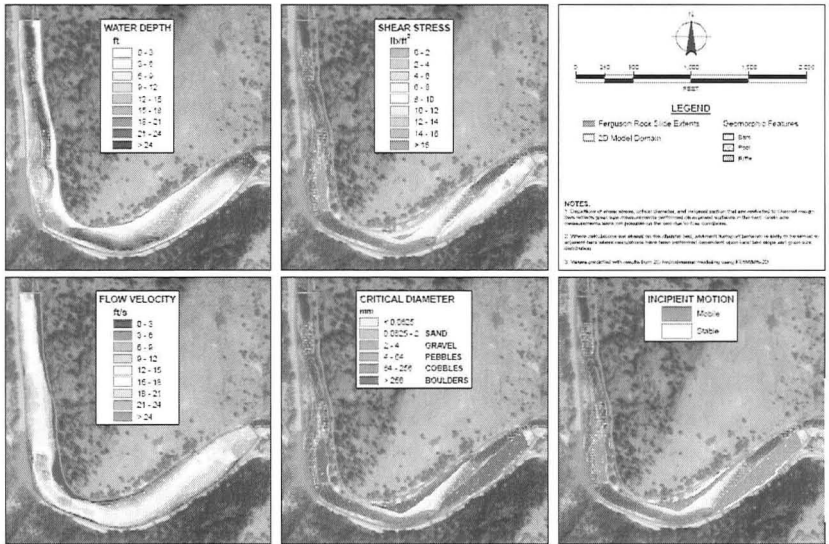


Figure 3. Distributions of depth, velocity, shear stress, critical sediment diameter and incipient motion for the natural condition at 42,000 cfs.

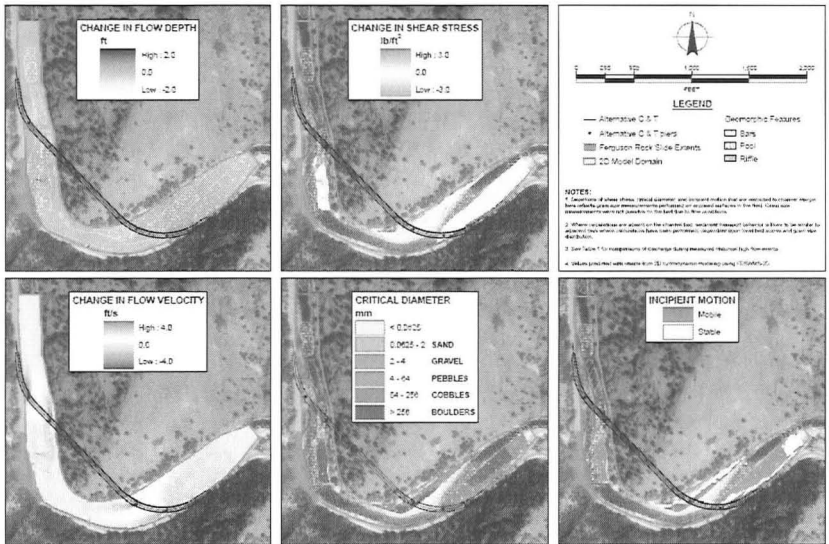


Figure 4. Distributions of change in depth, velocity, and shear stress relative to natural conditions for Alternatives C and T, and critical diameter and incipient motion.

whereas sediment mobility will be reduced in other locations that experience backwater effects and decreased flow velocities.

Synopsis of all modeling results

We performed the above analysis for all alternatives under both the low and high design flow conditions to assess river channel stability and whitewater recreational use. This resulted in a map of bridge pier feasibility zones (Figure 5). Our analysis goes far beyond a typical scour analysis and shows not only potential scour at pier locations but how the project reach as a whole may be modified under design flow conditions. In particular, our high flow analysis suggests that alternatives C, T, and S (results for S were not discussed) all pose some potential to permanently alter the nature of the existing river mostly in areas immediately adjacent to the bridges and piers, or in the high-flow channel and distal end of the bar mapped along the left bank, at the upstream bridges. These changes could include development of scour holes in bars, truncating the river side or downstream ends of these bars, erosion of the riffle mapped there, and perhaps upstream enlargement of the large pool mapped through the meander mid-way through the project reach.

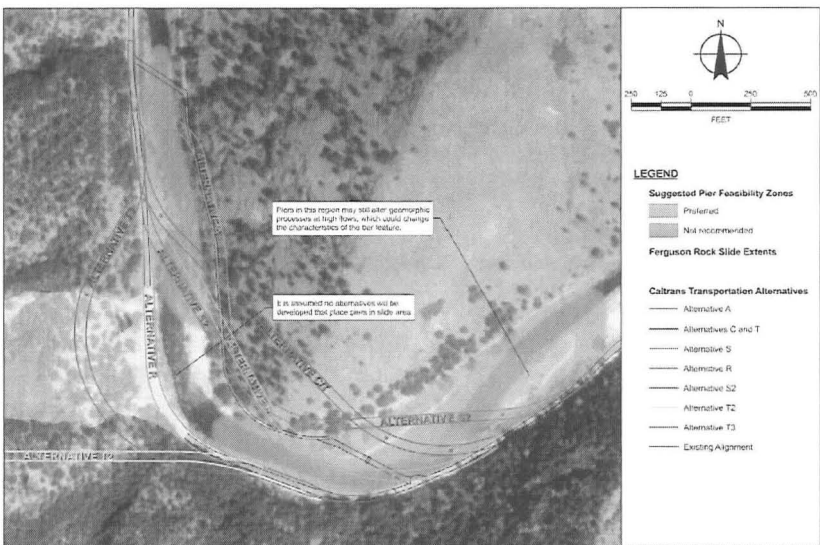


Figure 5. Suggested pier feasibility zones for continued planning and review of Ferguson Rock Slide Transportation Restoration Alternatives, Merced River, Mariposa County, California.

References

Bateman, P.C. (1992). "Pre-Tertiary bedrock geologic map of the Mariposa 1° by 2° quadrangle, Sierra Nevada, CA." *United States Geological Survey: Miscellaneous Investigations Series Map I-1960*.

- Beck, T.J. (2007a). "Preliminary Geotechnical Report." *Department of Transportation, Division of Engineering Services, Geotechnical Services – MS 5*, 13 p.
- Beck, T.J. (2007b). "Geotechnical Design Report." *Department of Transportation, Division of Engineering Services, Geotechnical Services – MS 5*, 11 p.
- Buffington, J.M. and Montgomery, D.R. (1997). "A systematic analysis of eight decades of incipient motion studies, with special reference to gravel-bedded rivers." *Water Resources Research* 33(8): 1993-2029.
- Caltrans (2006). "Chapter 860, Open Channels." *Highway Design Manual*: p. 860-1 – 860-13.
- Chow, V.T. (1959). *Open-channel Hydraulics*, McGraw-Hill, St. Louis, MO, 678 p.
- Cipponeri, A. (2007). "Location Hydraulic Study, Merced River at Ferguson Slide area." *State of California Department of Transportation*, 8 p.
- Environmental Modeling Research Laboratory (1999). "Surface-water modeling system reference manual, version 9.2." Brigham Young University, Provo, UT, 315 p.
- Froehlich, D.C. (2002). "Two-dimensional depth-averaged flow and sediment transport model—Users manual for FESWMS Flo2DH." *Federal Highway Administration: FHWA-RD-03-053*, 203 p.
- Haan, C.T., Barfield, B.J., and Hayes, J.C. (1994). *Design Hydrology and Sedimentology for Small Catchments*, Academic Press, San Diego, CA, 588 p.
- Harp, E.L., Reid, M.E., and Godt, J.W. (2006). "USGS memorandum re: Ferguson Rock Slide, Mariposa County, California." *United States Department of the Interior, U.S. Geological Survey*, 6 p.
- Huizinga, R.J. (2007). "Two-dimensional hydrodynamic modeling and analysis of the proposed channel modifications and grade control structure on the Blue River near Byram's Ford Industrial Park, Kansas City, MO." *United States Geological Survey: Scientific Investigations Report 2007-5098*, 45 p.
- Richardson, E.V. and Davis, S.R. (2001). *Evaluating scour at bridges, 4th Edition: U.S. Department of Transportation, Federal Highway Administration: Publication FHWA NHI 01-001, Hydraulic Engineering Circular No. 18*, 378 p.
- Whiting, P.J. and Dietrich, W.E. (1990). "Boundary shear stress and roughness over mobile alluvial beds." *Am. Soc. Civ. Eng., J. Hydraul. Eng.* 116(12): 1495-1511.

Correlation of Predicted and Measured Slope Erosion

Les Bromwell, Sc.D., P.E.¹ and Kenneth Ying, Ph.D.²

¹ BCI Engineers & Scientists, Inc., Lakeland, Florida

² Formerly BCI Engineers & Scientists, Inc.; currently Bechtel Power Corporation, Frederick, Maryland.

ABSTRACT

This paper presents calculated wave heights and predicted erosion of upstream earth dam slopes at the L-8 Reservoir during Hurricane Jeanne in September 2004. The predictions are compared with actual measurements of slopes erosion following the hurricane. The methodology used in this study includes application of the USACE (2006) Coastal Engineering Manual method for wave run-up and overtopping computation, the SWAN wave model, and the SBEACH erosion model.

During Hurricane Jeanne, the north interior slopes of the perimeter dam experienced significant erosion due to wave action. Using hurricane parameters from NOAA, the SBEACH model was used to predict the final configuration of the eroded slopes. By comparing the predicted slope configuration to photographs taken following the hurricane, it was seen that the model output closely resembled the actual damaged slope profile. This comparison provided a calibration of the SBEACH model that was then used to design the final reservoir slopes and to determine recommended operating levels prior to the passage of future hurricanes. The analytical modeling tools used for the L-8 Reservoir study have recently been extended to an analysis of placing expendable soil over stair-step soil cement armoring on an upstream dam slope. The purpose of expendable soil is to allow small animal ingress and egress from the water reservoir.

Introduction

Computer programs were used to calculate wave heights and predict erosion of upstream earth dam slopes at the Loxahatchee Reservoir (also termed as L-8 Reservoir) during Hurricane Jeanne, which passed over the area near the site on September 26, 2004. The predicted erosion profiles were compared with actual measurements of slope erosion made following the hurricane.

The Loxahatchee Reservoir is a key component of the Comprehensive Everglades Restoration Plan (CERP), a Federal/State project to improve water quality and the distribution of fresh water in south Florida. It is located in western Palm Beach County, Florida. The reservoir was constructed during the period 2003-2008 in a previously mined limestone quarry consisting of seven interconnected cells that had been excavated to approximately El. -4.26 m (-14 ft) (NAVD-1988). The reservoir was further deepened by dredging to El. -12.8 m (-42 ft) to provide additional storage capacity up to 56,740,165 m³ (46,000 acre-feet). A perimeter dam to El. +7.01 m (+23 ft) surrounds the reservoir to provide overtopping protection as well as additional water storage. Normal operating level for the reservoir is +4.57 m (+15 ft.), which is approximately natural ground level.

The determination of dam freeboard and the assessment of potential erosion due to wave action have been major design issues of the CERP program. This is due to the major cost implications of higher dam heights as well as the high cost of armorings interior slopes against excessive erosion caused by wind-driven waves. Computations of wave height, wave setup, run-up, overtopping/overwash, and embankment erosion are used to meet these objectives. The methodology used in this study includes application of the USACE (2006) Coastal Engineering Manual method, the SWAN wave model, and the SBEACH erosion model. Hurricane data from NOAA's website were downloaded to provide the wind field data input to wave model. Sediment samples collected from the site were used in the erosion model. The post storm condition includes the rainfall data, water level records and photographs taken during the damage assessment after Hurricane Jeanne. These data were used to compare the simulation results produced by computer models.

Methodology

The purpose of the wave and erosion modeling is to estimate potential damage to the reservoir embankments caused by storm generated waves. The modeling effort involves the computation of wave heights in the reservoir and the calculation of cross-sectional erosions under various storm conditions. The SWAN model was used to compute the wave height distribution in the reservoir, which was then used in the SBEACH erosion model to calculate the cross-sectional profile changes for each embankment. In order to demonstrate that the results generated by these computer models are reliable, a real hurricane event was selected to test the model in the validation procedure. The wind data used in the wave modeling was obtained from the historical storm records. Hurricane Frances passed through the site in September 2004 and followed by Hurricane Jeanne 20 days later. The L-8 reservoir was gradually filled up by precipitations brought in by Hurricane Frances and its remnant up to about 3.05 m (10 ft) elevation. During the passage of Hurricane Jeanne, wind generated waves caused severe damages to the earth embankments in the reservoirs.

The models were set up to simulate the storm conditions of Hurricane Jeanne 2004 for embankment erosion. An initial calibration was performed for each model to test grid and sensitivity of parameters as part of the standard procedure for numerical modeling. The wave data had no observed values to be compared with but the erosion model had the cross sectional profiles to be compared with. Comparisons were made between the modeled results and the photo record of the wave damages taken after the storm. Details of comparisons will be explained later in this paper.

Wave Model

SWAN (Simulating Waves Nearshore) model, developed by the Delft University of Technology (2006), is a two-dimensional model designed for the computation of wind generated waves in the coastal water bodies, lakes, reservoirs and estuaries. It is based on the discrete spectral action balance equation. The wave propagation is based on linear wave theory including the effect of currents. The processes of wind generation, dissipation and nonlinear wave-wave interactions are

represented explicitly with third-generation formulations. For application, it considers factors such as wave propagation in time and space, shoaling, refraction due to current and depth, diffraction, frequency shifting due to currents and non-stationary depth, nonlinear three and four-wave interactions, white-capping, bottom friction, and depth-induced breaking, etc.

In this investigation, SWAN was used to calculate the significant wave heights, wave periods and wave directions for each storm's wind field. All of these outputs are required by the SBEACH erosion model for the computation of the cross-sectional erosion. The input data for the SWAN model includes the 2-dimensional grid mesh, water depth, wind field distribution, friction coefficients, flow velocities, boundary conditions, and control parameters. Detailed description for the model application is to be presented later in this paper.

SBEACH Model

SBEACH model was developed by the U. S. Army Corps of Engineers (Larson and Kraus, 1989; Larson *et al.*, 1990) for the simulating of beach profile change under the short crested wave conditions. This model was formulated based on a series of large wave tank tests and was validated by field data from the east and west coasts of the United States. The model assumes that the cross-sectional profile change is mainly governed by breaking of short-period waves. Both of the regular and irregular waves were considered. The formulation also included the factors like water depth, grain size, deep water wave steepness, the angle of avalanching of sediments and the transport rate coefficient. The avalanching angle and transport rate coefficient are basic calibration parameters determining the geometric and time scale of profile change. For the cross-sectional profiles with rock or non-erodible surface, SBEACH model was incorporated with the Non-erodible or Hard Bottom option (Larson and Kraus, 1998), which allows users to include non-erodible segments in the profiles. It also allows the seawall options, but only the Hard Bottom option was used for the current study.

For the L-8 reservoir, each embankment can be treated as one beach profile. The waves near the center of the reservoir are similar to the incident waves offshore of a beach profile. Since the site includes soil and rock layers on the embankments, both of the erodible and non-erodible segments are applied for the current study. Other parameters and procedures will be discussed in the next section.

INPUT DATA

Storm Data

For a hurricane, the wind field distribution is determined by the central pressure deficit, forward speed, radius to maximum winds, landfall point, track of the storm and the geometric formation of land. The last factor is not easy to implement and others can be accounted by several methods. Among these methods, the Holland (1980) wind field model is one of the best methods to calculate the hurricane wind distribution. The method has been broadly used to produce the wind field distribution for the modeling of storm surges and wind damage forecasts. For the historical storm

data, the Holland model can be used to calculate the detailed wind field distribution wherever the historical data is not sufficient or available.

NOAA processes post storm wind data for each hurricane and publishes the results on their website (http://www.aoml.noaa.gov/hrd/data_sub/wind.html). In the current study, a historical storm is used for calibration and hypothetical storms are used for the operational runs. The historical hurricane wind field data from NOAA was applied to the validation model without any problem. For other runs after the validation run, the wind field distributions for hypothetical storms were calculated by using the Holland model. It should be pointed out that the wind speeds for the hypothetical storms could be overestimated. Holland model may overestimate wind speeds since it does not consider the land friction factor after storm moves into inland. For the current study, the existing estimated wind field data from the Holland wind field model were used. They give conservative design criteria, which will not cause any safety concern for the reservoir.

In September, 2004, Hurricane Jeanne passed through the northern part of the Palm Beach County, Florida. As a result, L-8 reservoir suffered a severe damage due to the wave erosion. The wind field data available from NOAA website for Hurricane Jeanne are shown in **Figures 1(a)** and **1(b)**. By applying these data, the time series of wind speed and wind direction at the L-8 site can be calculated as shown in **Table 1**. Note that these wind speeds are the one-minute sustained wind speeds at ten meters above the ground or water surface. They were converted to 10-minute sustained wind for the wave model. Data from NOAA include one complete wind field distribution for every three-hour interval along the storm track. Interpolations over space and time were necessary to derive the half-hour interval wind field data in between. The wind direction is measured counterclockwise from the east (positive x-axis) to the direction which wind is blowing to. The present computation adapts the Cartesian convention for the SWAN wave model.

Water Level Data

The water level data in L-8 reservoir were affected by two factors: rainfall and pumping activity. The water levels of the reservoir are monitored by the South Florida Water Management District. The record of water levels before and after the arrival of the Hurricane Jeanne is listed in **Table 2**. All the water levels are referred to NAVD datum in feet. The recorded water levels, ranging from 1.52m (5ft) to 5.18m (17ft) for various cells, on the day when the hurricane visited were selected for the model input. The local rain gage at the reservoir reported about nine inches of rainfall for Hurricane Jeanne. However, there was no data available for the day before the storm. Due to the remnant effect from Hurricane Frances prior to the landfall of Hurricane Jeanne, the exact starting water level in the reservoir for Hurricane Jeanne is not clear. It is assumed that the recorded water level on September 26, 2004 was the pool level in the reservoir when the maximum wind struck the L-8 site.

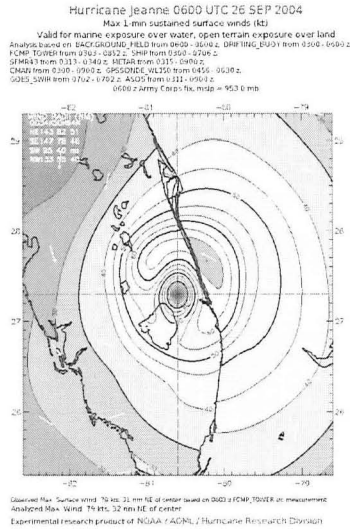


Table 1. Wind field data for Hurricane Jeanne at the L-8 site.

Time	10-min max. sust. wind, m/s	Wind Dir, degrees	Time	10-min max. sust. wind, m/s	Wind Dir, degrees
9/25 21:00	14.4	283.7	9/26 3:30	35.9	331.9
9/25 21:30	15.6	284.6	9/26 4:00	36.1	342.1
9/25 22:00	16.7	285.7	9/26 4:30	35.8	352.3
9/25 22:30	17.8	286.9	9/26 5:00	35.1	3.2
9/25 23:00	19.1	288.2	9/26 5:30	34.8	13
9/25 23:30	20.6	289.6	9/26 6:00	33.6	21.4
9/26 0:00	22.3	291.3	9/26 6:30	32.0	27.6
9/26 0:30	24.2	294.4	9/26 7:00	30.3	32.5
9/26 1:00	26.2	298	9/26 7:30	28.9	37.7
9/26 1:30	28.6	302.6	9/26 8:00	27.7	41.1
9/26 2:00	30.9	307.9	9/26 8:30	26.4	44.5
9/26 2:30	33.2	314.5	9/26 9:00	25.5	46.8
9/26 3:00	34.7	322.6			

Table 2. Water levels at the L-8 site during Hurricane Jeanne 2004.

Date	Cell 1	Cell 2	Cell 3	Cell 4	Cell 5	Process	L-8
9/15/2004	7.015	7.015	5.015	9.815	9.815	17.265	13.705
9/16/2004	7.095	7.095	5.175	9.875	9.875	17.165	13.165
9/17/2004	7.155	7.155	5.415	9.915	9.915	17.065	12.565
9/20/2004	8.315	8.315	3.515	9.915	9.915	16.455	12.485
9/21/2004	8.555	8.555	3.715	10.135	10.135	17.005	13.065
9/22/2004	8.635	8.635	4.015	10.215	10.215	17.045	14.665
9/23/2004	8.715	8.715	4.315	10.215	10.215	17.005	14.565
9/24/2004	9.015	9.015	4.315	10.015	10.015	16.985	13.965
9/26/2004	10.365	10.365	5.365	10.225	10.225	17.115	15.495
9/27/2004	11.715	11.715	6.415	10.445	10.445	17.235	17.015
9/28/2004	13.835	13.835	8.315	10.655	10.655	17.365	16.965
9/29/2004	14.315	14.315	13.215	11.015	11.015	17.365	16.925
9/30/2004	14.435	14.435	14.435	11.375	11.375	17.525	17.165

Calibration Run and Result Comparison

The model calibration focused on the cross-sectional erosion resulted from the wave. Since wind is the major driving force generating the waves which subsequently cause the erosion to the embankments, the calibration procedure emphasized on the relationship between the wind and the erosion result. Given the real wind data at the site, if the models can reproduce the real erosion conditions, then the models are ready to simulate the embankment erosion at the L-8 site.

After obtaining the wind data, the parameters in SWAN wave model were adjusted for a hurricane wind condition as follows: Bottom friction was set at wind sea condition with bottom coefficient of $0.067 \text{ m}^2/\text{s}^3$ for the Jonswap bottom friction dissipation formulation; Wave and wave interaction was set at the three wave interaction mode for the shallow water condition; and Wave setup mode was turned

on for the computation of surface water level build up due to the wave breaking and dissipation of wave energy.

The results of the wave model could be judged by comparing data from a similar water body. But this kind of data is not easy to find. Hence the wave outputs were only checked for the maximum values and the wave height distribution pattern. The maximum wave heights were expected to be much lower than the wave heights in the open sea due to the small volume of the water body in the reservoir relative to the ocean. For a storm with 128.7 km/hr (80 mph) wind, the wave heights in the open sea range from 7 to 14 meters according to the data measured by the National Data Buoy Center (NDBC) in the Gulf of Mexico and the Atlantic Ocean (<http://seaboard.ndbc.noaa.gov/hmd.shtml>). The buoys used by NDBC are located in the open sea with water depth more than 1,000 meters. The behavior of waves in the deep ocean is much different from the wave pattern in a small inland water body. The computed maximum wave heights in the L-8 reservoir for 128.7 km/hr (80 mph) wind are about 1.2 meters. With the water depth ranging from 14.3 to 17.3 meters in the reservoir and the surface area less than one square kilometer in each cell, the wave heights are limited by the dimension of the wind fetch. Using the Figure 3-23 in the Shore Protection Manual (1984), the significant wave height for the wind fetch of 2 km long and 128.7 km/hr (80 mph) wind speed is 1.25 meters. This indicates that the wave height of 1.2 meters given by the SWAN model seems reasonable for the 128.7 km/hr wind.

The output from the SWAN wave model provides the wave input to the SBEACH model. SBEACH requires wave height, wave period, wave direction, water level, wind speed, and wind direction. Other than the wind and wave data, SBEACH requires the cross-sectional profile of the embankment, physical properties of the sediment, and the water temperature. The cross-sectional profile includes the erodible and non-erodible segments of the embankment. In the input data, the rock bed and cemented surface are treated as non-erodible surfaces and others are erodible. The sediment properties include the medium grain size and the avalanching angle of the cross-section. For the L-8 site, the medium size is 0.319 mm and the avalanching angle is determined to be 60 degrees due to the high bonding force for the compacted dry material on site. The water temperature is taken to be 28°C for the local climate condition. The SBEACH model produces results in the graphic and tabular formats. For Hurricane Jeanne, the wave model output is shown in Figure 2. The simulated cross sectional profiles for Phase One embankment before and after the storm are presented in Figure 3. Note that the horizontal scale of the model output is compressed in order to fit in the paper size for the plot. Figure 4 shows the photos of Phase One embankment taken after Hurricane Jeanne. For comparison, the model output is stretched to get the right horizontal scale as shown in Figure 5. By comparing the model output figure to the photos, it can be seen that the model output closely resembles the real damaged profile with similar magnitude of slope angles on the upper part of the embankment.

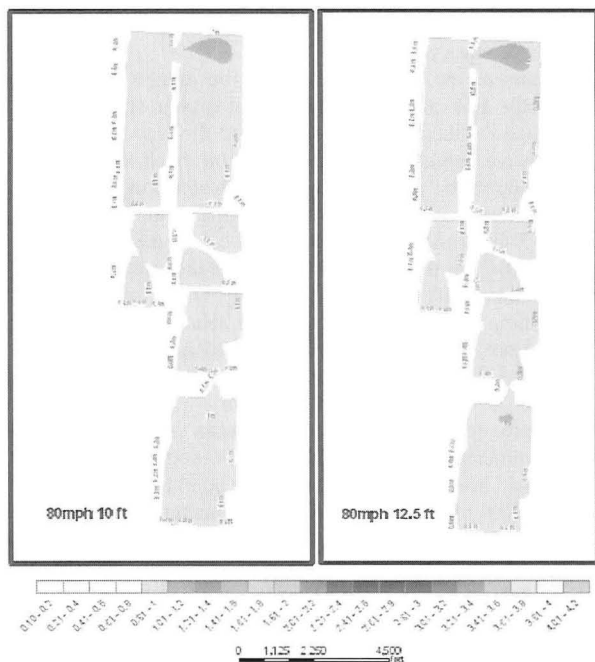


Figure 2. Significant wave height distribution in the PBA reservoir.

Old Phase One embankment

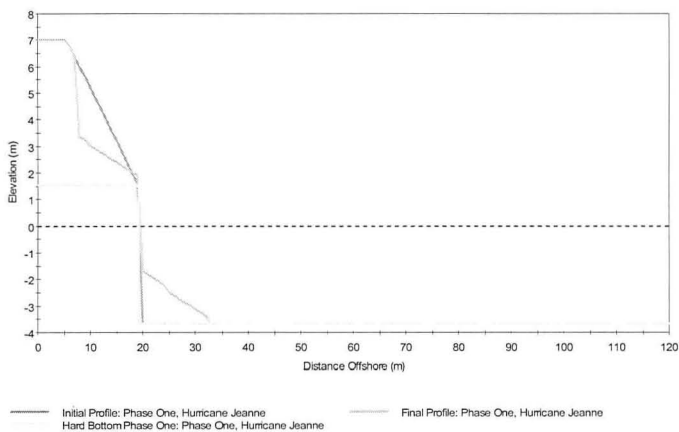


Figure 3. SBAECH erosion model output for Phase One embankment after Hurricane Jeanne.



Figure 4. Picture of Phase One embankment after Hurricane Jeanne.

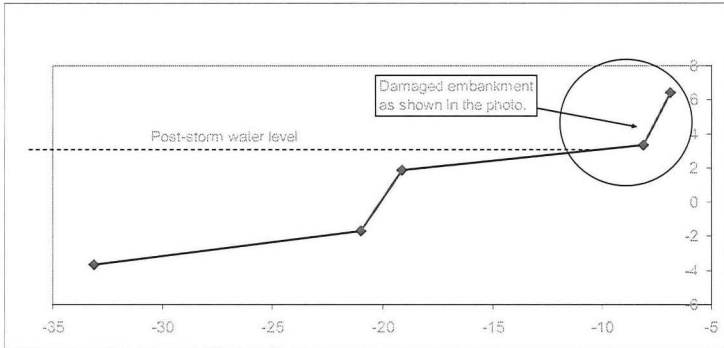


Figure 5. Model result with corrected horizontal and vertical scales for the damaged embankment cross section.

After the validation, a series of modeling runs were made to evaluate the wave and erosion conditions in the reservoir for various storms. The range of storm wind speeds varies from the 112.6 km/hr (70mph) to 321.8 km/hr (200 mph), which covers Category 1 to 5 hurricanes and the DCM-2 criteria (South Florida Water Management District, 2005). For each storm, the pool levels from 1.52 m (5ft) to 5.03 m (16.5ft) were used to simulate the operational mode of the reservoir. The soil volume loss caused by erosion at each embankment was calculated for each storm to evaluate the degree of possible damage. The quantified values of erosion are used as the reference to generate the operational guidance to minimize the damage by lowering water to the optimal level in the reservoir prior to the arrival of each storm.

The analytical modeling tools for this study have been extended to analysis of placing expendable soil over stair-step soil cement armoring on an upstream dam slope. The purpose of expendable soil is to allow small animals (mainly turtles and fledging birds) ingress and egress from the water reservoir with the stair-step type embankment. The models were applied to evaluate the mitigation of animal entrapment in reservoirs with stair-steps armoring appears feasible by using an expendable soil layer on top of the stair-steps to form a smooth slope. The model results show that the soil layer can be washed away by waves to expose the stair-steps within a short time during a major hurricane. The recommended construction material for this expendable layer is a non-cohesive sand, gravel, or combination thereof.

Summary

SWAN Model and SBEACH Model were applied to simulate the cross sectional erosion for the embankments in the L-8 Reservoir. The post storm wind data for Hurricane Jeanne were selected to be the input to the wave model. The wave output from SWAN model was then applied to the SBEACH erosion model along with the wind data and the soil properties. The results produced by this procedure closely resembled the real erosion damage caused by Hurricane Jeanne. The procedure shows that the models can be applied to simulate the future wave erosion in the L-8 Reservoir. Further simulations were carried for wind speeds from 70 mph to 200 mph with operational water levels ranging from 5 ft to 16.5 ft in the reservoir. The potential damage measured in eroded soil volume to each embankment was also estimated for each storm scenario. The results produced by the models provided significant information for the reservoir operation to minimize the potential damages caused by the hurricanes.

REFERENCES

1. Delft University of Technology (2006). "SWAN Technical Documentation", SWAN Cycle II Version 40.51, Delft, The Netherlands.
2. Holland, G. J. (1980). "An Analytic Model of the Wind and Pressure Profiles in Hurricanes," *Mon. Wea. Rev.*, Vol 108, pp 1212-1218.
3. Larson, M. and N.C. Kraus (1989). "SBEACH: Numerical Model for Simulating Storm-Induced Beach Change; Report 1: Empirical Foundation

- and Model Development.” U.S. Army Corps of Engineers, Technical Report CERC-89-9, Washington, D.C.
4. Larson, M., N. C. Kraus and R. Byrnes (1990). “SBEACH: Numerical Model for Simulating Storm-Induced Beach Change; Report 2: Numerical Formulation and Model Tests.” U.S. Army Corps of Engineers, Technical Report CERC-89-9, Washington, D.C.
 5. Larson, M. and N.C. Kraus (1998). “SBEACH: Numerical Model for Simulating Storm-Induced Beach Change; Report 5: Representation of Nonerrodible (Hard) Bottoms.” U.S. Army Corps of Engineers, Technical Report CERC-89-9, Washington, D.C.
 6. South Florida Water Management District (2005), “Design Criteria Memorandum: DCM-2 Revision 001.00. Wind and Precipitation Design Criteria for Freeboard,” Acceler8 Ref #: P 599, 2-3-056
 7. U.S. Army Corps of Engineers (2006). “Coastal Engineering Manual,” Part II, EM-1110-2-1100.
 8. U.S. Army Corps of Engineers (1984), “Shore Protection Manual,” Volume I, Coastal Engineering Research Center.

Design of Erosion Protection at Landfill Areas with Slopes Less than 10%

Clifford Anderson¹, M. ASCE, PE, PhD, D.WRE and Steve Wall²

¹Department of Engineering, Central Connecticut State University, 1615 Stanley Street, New Britain, CT 06050-4010, USA, email: cliff@ahymo.com

²Office of Pollution Prevention and Solid Waste (WST-7), US EPA Region 9, 75 Hawthorne St., San Francisco, CA 94105, USA, email: Wall.Steve@epamail.epa.gov

ABSTRACT

Surface water can enter landfill waste zones from top surface areas and erosion of the top surface can cause wash-out of waste material. Landfill covers at these locations must prevent surface water infiltration and provide erosion resistance. In arid climates a rock veneer can be used to reduce erosion, but this will increase infiltration and reduce surface evaporation making it more likely that surface water will enter waste zones. An alternative is the placement of a mix of soil and gravel as a surface layer; the mix is commonly called a gravel admixture. Studies of gravel admixture layers have shown they provide greatly reduced surface infiltration rates over gravel alone, and have evaporation rates very similar to soil alone. A method is presented to compute the rock and soil gradations, and thicknesses of gravel admixture layers based on peak flow, slope and the formation of surface channelization. The procedure is used to select gradation ranges and applicable slope lengths for a landfill cover.

INTRODUCTION

Regulations for closure of municipal waste landfills typically follow the Federal regulations established by the Resource Conservation and Recovery Act (RCRA, 1976, Subtitle D program, 40 CFR 258). These regulations require the top soil layer to have a slope not less than 0.03 m/m, and not greater than 0.05 m/m. This minimum slope is required to prevent surface ponding because a landfill is subject to substantial local settlement due to solid waste decomposition. To minimize ponding and infiltration, designers commonly consider slopes approaching the 0.05 m/m limit. Steeper slopes of 0.08 or 0.10 m/m have been considered for some sites.

In some climate zones a vegetative cover can be used to provide an effective erosion blanket at a landfill cover system. However, in many of the arid and semi-arid areas of the southwest United States, the natural vegetation will cover only 10 to 20 percent of the surface (Anderson and Stormont, 2005). If native plants are used for southwestern landfill cover systems, a continuous erosion blanket is not likely to be created. The impact from raindrops initiates local soil movement, but it is the conveyances across slopes that cause local soil movement to become erosion. The creation of longer or steeper cover slopes can have consequences for erosion that will become obvious only after severe rainfall events.

In dry climates, a gravel surface mulch or veneer can be designed to provide erosion protection. A gravel veneer is typically constructed by placing a 3 to 10 cm thick layer on the soil surface. The gravel must be of sufficient size that it will not be substantially displaced during a major storm event. Rounded gravel with a diameter of

1.3 to 5 cm ($\frac{1}{2}$ to 2 in.) is typically used. Experimental studies have shown that gravel mulch can significantly reduce sediment yield from a cover (Finley et al., 1985; Wischmeier and Smith, 1978). However, there are two properties of a gravel veneer that discourage landfill use: 1) it can reduce the evaporation rate, and 2) it may create a habitat for deep-rooted plants (Waugh and Petersen, 1994; Kemper et al., 1994).

Some landfills in arid climates are being constructed with thicker soil layers in place of clay or geomenbrane layers because they can provide equivalent or superior performance at a lower cost. The successful function of soil-only landfill covers is very dependent upon the ability of the surface layer to reduce surface infiltration and allow evaporation to remove moisture from the soil cover layers. Waugh and Petersen (1994) suggest that moderate amounts of gravel mixed into the cover topsoil will control both water and wind erosion without the negative effect on vegetation and soil-water balance caused by a gravel veneer. When a mix of soil and gravel is used as a surface layer, the mix is commonly called a gravel admixture. If the gravel admixture contains a sufficient quantity of appropriately sized rock, a gravel admixture will also provide erosion protection in a manner similar to placement of rock alone. The procedures described in this document can be used to guide the design of a gravel admixture that will provide for reduced surface erosion, and create a surface with water infiltration and evaporation similar to a natural soil.

The analyses presented in this document generally apply to landfill top surface areas with slopes between 3% and 10%. Flatter sloped areas may have settlement and ponding conditions that may not be adequately addressed by ordinary soil covers. The computed admixture layer thicknesses may become large for slopes steeper than 10% when slope lengths and runoff quantities also become large. While there is nothing in the procedure that specifically limits the use of gravel admixtures to slopes less than 10%, construction economics may lead to other surface treatment methods.

The design of a gravel admixture layer to protect a landfill surface requires evaluation of small watershed hydrology and hydraulics, and the design of the conveyances where water is expected to flow. In the case of most uniformly graded landfill surfaces, a fixed flow path or channel may not be constructed into the surface. The site physical conditions and measurements completed after events at similar areas can be used to predict surface flow conditions. For a landfill top surface in the arid and semi-arid areas of the southwest United States a 100-year event is a suggested design condition, but other site conditions may warrant use of different frequencies.

PEAK FLOW AND UNIT DISCHARGE

For any given watershed, the 100-year frequency event peak flow (Q_{100}) can be determined from a basic hydrologic analysis, such as with the Rational Method or NRCS Curve Number (CN) procedure. Peak flow during the storm event is the most important hydrologic property to accurately predict. For a planar watershed surface with an identified length, but a width that can be identified only after erosion has occurred, the recommended watershed width for runoff computations should be 25% of the watershed length. The dominant discharge peak flow (Q_m) can be evaluated by considering the statistically weighted average of the peak runoff occurring over a long period, for example 100 years. In the arid southwestern the Q_m can be estimated at 10% of Q_{100} . For a wide channel section where:

$$\frac{A}{WP} = \frac{b d_h}{b + (2 d_h)} = d_h \quad \text{at} \quad b \gg d_h \quad [1]$$

Manning's equation for open channel flow can be written to solve for the width of flow (b) as:

$$b = Q_{100} n s^{-0.5} d_h^{-1.667} \quad [2]$$

where: b is the width of flow (m),
 A is the area of flow (m²),
 WP is the wetted perimeter (m),
 d_h is the hydraulic depth (m),
 Q_{100} is the peak flow at 100-year frequency (m³/s),
 n is the Manning's roughness coefficient,
 and s is the slope of the channel profile (m/m).

A geomorphologic equation to describe the width of open channel flow as a function of dominant discharge and percentage of silt and clay is given in *Engineering Analysis of Fluvial Systems* (Simons, Li and Associates, 1982, p 5.47) and in *Watershed and Stream Mechanics* (D. B. Simons, R. M. Li, et al., 1980, p. 4-37). While this equation was not specifically adapted to address landfill cover runoff, it has been found to provide appropriate values for this application. The geomorphologic equation (converted from US customary to metric form) is:

$$b = 43.7 Q_m^{0.38} M^{-0.34} \quad [3]$$

where: Q_m is the dominant discharge (m³/s),
 and M is the percentage of silt and clay in the channel perimeter.

The value of Q_m can be computed as:

$$Q_m = Q_{100} / DD_{factor} \quad [4]$$

where: DD_{factor} is the dominant discharge factor = Q_{100} / Q_m (Use a value of 10),
 and Q_{100} is the peak flow at 100-year frequency (m³/s).

Manning's equation, [2], and the geomorphologic equation, [3], are both expressed as functions of b , so they can be equated to become:

$$Q_{100} n s^{-0.5} d_h^{-1.667} = 43.7 Q_m^{0.38} M^{-0.34} \quad [5]$$

Equation [4] and equation [5] can be combined to obtain:

$$d_h^{-1.667} = 43.7 (Q_m/Q_{100}) Q_m^{-0.62} n^{-1} s^{0.5} M^{-0.39} \quad [6]$$

Then equation [6] can be reformulated to obtain the hydraulic depth:

$$d_h = (43.7)^{-0.6} (Q_m/Q_{100})^{-0.6} Q_m^{0.372} n^{0.6} s^{-0.3} M^{0.234} \quad [7]$$

The channel profile slope, s , and the percentage of silt and clay, M , are physical properties that can be measured at a watershed. The Strickler relation (Anderson, et al, 1970) can be used to estimate the Manning's roughness coefficient, n , with the following equation:

$$n = 0.0488 (D_{50}/1000)^{0.167} \quad [8]$$

where: D_{50} is the median size of the rock riprap (mm).

The value of D_{50} can be estimated from a preliminary analysis, and this value can then be used to compute an interim D_{50} for the erosion protection. The final value of D_{50} can be obtained with an iterative process. Including equation [8] in equation [7] results in:

$$d_h = (43.7)^{-0.6} \left(\frac{Q_m}{Q_{100}} \right)^{-0.6} Q_m^{0.372} \left[0.0488 \left(\frac{D_{50}}{1000} \right)^{0.167} \right]^{0.6} s^{-0.3} M^{0.234} \quad [9]$$

Equations [3] and [9] describe the flow width and depth based on the geomorphologic equation of Simons, Li and Associates. Except for the D_{50} , all of the values in these equations can be estimated from physical watershed properties. The equations can also be used to compute the 100-year event unit discharge, Q_{100}/b , and the width-to-depth ratio, b/d_h . While the dominant discharge, Q_m , is used in equation [9], the computed hydraulic depth, d_h , represents the depth from a 100-year frequency event.

A second geomorphologic parameter is the width-to-depth ratio of the flowing water. For arid and semi-arid locations the maximum width-to-depth ratio is approximately 40, although other values may need to be considered for local conditions. If the width-to-depth ratio, b/d_h , using equations [3] and [9] exceeds 40, the b and the d_h should to be re-computed to maintain a width-to-depth ratio of 40. The width-to-depth relation can be represented with the following equation:

$$b = F d_h \quad [10]$$

where: F is the width-to-depth ratio. (Commonly a value of 40)

Equation [2] and equation [10] can be combined to obtain:

$$Q_{100} n s^{-0.5} d_h^{-1.667} = F d_h \quad [11]$$

This equation can be reformulated to compute the hydraulic depth as:

$$d_h = [(Q_{100} n)/F]^{0.375} s^{-0.1875} \quad [12]$$

Equations [10] and [12] describe the flow width and depth based on a defined width-to-depth ratio. Equations [10] and [12] should be used whenever the b/d_h computed from equations [3] and [9] exceeds 40. Using equations [3] and [9], or equations [10] and [12], the flow velocity, V_{100} , the Froude number, F_r , the width of flow, b , and the unit discharge, q_f , can be computed.

ROCK SIZES AND ADMIXTURE LAYER THICKNESS

With the flow properties established, the S. R. Abt and T. L. Johnson equation (1991) can be used to solve for the median rock size of the gravel veneer. A factor of safety of 1.2 should be applied to the rock size equation as recommended on page 967 of the Abt and Johnson paper. The Abt and Johnson equation uses the unit discharge, and profile slope to compute the median rock size when failure is expected to occur. The unit discharge is computed using the smallest b obtained from equation [3] and equation [10] so that the computed unit discharge is the maximum value computed from the two equations. The equation for unit discharge is:

$$q_f = Q_{100}/b \quad [13]$$

where: q_f is the unit discharge or unit flow rate (m^2/s).

The Abt and Johnson equation with the addition of the recommended factor of safety and converted to metric form is:

$$D_{50} = (12 \times 502.9) s^{0.43} q_f^{0.56} \quad [14]$$

where: D_{50} is the median rock size of the gravel veneer.

The physical testing by Abt and Johnson did not use slopes steeper than 20% (0.20 m/m). Abt and Johnson's paper suggested that the gravel layer thickness should be 1.5 to 3.0 times the D_{50} . The D_{50} computed from equation [14] can be used to determine the rock gradation for the gravel portion of the gravel admixture layer. The following procedure is recommended:

- specify a construction minimum D_{50} (D_{50-min}) based on the computed value from equation [14] rounded to the nearest 6.4 mm (0.25 inch).
- specify a design maximum D_{50} (D_{50-max}) at 140% of the D_{50-min} , rounded to the nearest 6.4 mm (0.25 inch).
- specify a minimum D_{100} ($D_{100-min}$) at 150% of the D_{50-min} , rounded to the nearest 6.4 mm (0.25 inch).

- specify a design maximum D_{100} ($D_{100-max}$) at 200% of the D_{50-min} , rounded to the nearest 6.4 mm (0.25 inch). The constructed admixture can have a larger value with an appropriate adjustment in the layer thickness.
- specify a minimum D_{15} (D_{15-min}) at 45% of the D_{50-min} , rounded to the nearest 6.4 mm (0.25 inch).
- specify a design maximum D_{15} (D_{15-max}) at 80% of the D_{50-min} , rounded to the nearest 6.4 mm (0.25 inch).
- specify the coefficient of uniformity ($C_u = D_{60} / D_{10}$) with an allowable range between 1.75 and 3.0.

The Abt and Johnson physical testing used rock with an average specific gravity of 2.66. In order to use this equation without adjustment, the rock in the gravel admixture should have an average specific gravity of 2.65 or larger. This is equivalent to a particle unit weight of 2650 kg/m^3 (165 lbs/ft^3). If any rock with a smaller average specific gravity is proposed for use, the size of the D_{15} , D_{50} , D_{100} , and Y_{min} would need to be adjusted based on the ratio of the buoyant weight of the rock.

The gravel admixture should have a constructed percentage of gravel of not less than 25% and not more than 50% of the total admixture. To maintain these limits it is recommended that the design percentage of gravel be established between 30 and 45%. The total thickness of the gravel admixture layer is the sum of the minimum rock layer thickness plus the scour depth. The total admixture layer thickness is computed as follows:

- specify the minimum rock layer thickness ($Y_{min-rock}$) at the 2.0 times the D_{50-min} , or 1.0 times the $D_{100-max}$, whichever is larger.
- compute the scour depth (Y_s) with the equation:

$$Y_s = Y_{min-rock} [(100/\%Gravel) - 1.25] \quad [15]$$

- compute the total admixture layer thickness (Y_{total}) as:

$$Y_{total} = Y_s + (1.5 \times Y_{min-rock}) \quad [16]$$

with Y_{total} rounded to the nearest 0.025 m (1.0 inch). The minimum recommended value of Y_{total} is 0.15 m (6 inches) for slopes between 0 and 10%. The minimum recommended value of Y_{total} is 0.30 m (12 inches) for slopes greater than 10%.

% OF GRAVEL, "FINER SOIL" AND "GENERAL SOIL"

In order for the gravel admixture layer to retain its properties of reduced surface infiltration and increased evaporation, constraints must be placed on the quantity of gravel in the admixture layer and on the remaining soil that is smaller than gravel. The percentage of gravel in an admixture layer is computed by comparing the computed D_{50-min} and D_{15-min} with the percentages in the proposed gradation that are at these computed sizes. For example, if a specified admixture has a higher percentage of

particles larger than the computed D_{50-min} , the percentage of gravel in the admixture gradation is larger than with an optimal gradation. The percentage of gravel in a gravel admixture is estimated by first computing the percent of the mix that passes the computed D_{50-min} and the computed D_{15-min} to obtain the % Passing D_{50} and % Passing D_{15} in the proposed mix. These values are then used to estimate the percentage of gravel in the mix using the following equation:

$$\%Gravel = [1.24 \times (1 - \%PassingD_{50})] + [0.36 \times (1 - \%PassingD_{15})] \quad [17]$$

The equivalent particle size for the gravel can be found by computing the gradation particle size that corresponds to the % Gravel. The range of % Gravel in the admixture should be between 5% and 50%. For the soil material in the admixture that is smaller than gravel, the gradation is further described as "finer soil" and "general soil". Finer soil is all soil material smaller than a #4 sieve (4.75 mm). In order to maintain good infiltration resistance and evaporation rates, the percentage of finer soil in the admixture should not be less than 34%. The finer soil should also have a minimum percentage of silt or clay size particles (particles passing a #200 sieve, or smaller than 0.075 mm) with the silt and clay at 5% to 50% by weight of the finer soils. A large percentage of clay size particles (smaller than 0.005 mm) in the finer soils could cause surface cracking, and it is suggested that clay size particles should not exceed 40% by weight of the finer soils. Additional specifications to limit the content of expansive clay and dispersive clays are recommended. For the gravel admixture, the finer soils should be between 34% and 95% by weight of the admixture. The soils that are finer than the gravel and larger than the #4 sieve (4.75 mm) are considered to be general soils. General soils are not required for the gravel admixture but they are expected to be present in a normal admixture gradation. General soils can be 0% to 60% by weight of the total gravel admixture.

In order for the gravel admixture to function as an erosion barrier, there must be a sufficient quantity of gravel in the admixture layer so the admixture layer can protect the soil layers below the admixture layer. The thickness of the gravel portion required to provide erosion protection for the admixture layer is approximately 3 times the computed D_{50-min} . This ratio of the rock layer thickness to D_{50-min} is greater than commonly used for larger riprap, because of the smaller size material and the reduced precision of individual particle placement. Ratios of 3 to 4 are commonly recommended for finer rock sizes. If the percentage of gravel in the admixture is 80% by weight, the finer material would have a volume nearly equal to the void space between the stable gravel particles, and there would be no need for consideration of additional layer thickness. However, the percentage of gravel in the admixture will be between 5% and 50%, so that a major portion of the required admixture thickness is due the material smaller than gravel. Additional layer thickness is required because the particles smaller than the gravel will be removed by channelized erosive flows. At 45% gravel the total admixture thickness will need to be approximately 5 times the computed D_{50-min} , and at 21% gravel the total admixture thickness will need to be approximately 10 times the computed D_{50-min} .

When a single proposed material gradation is evaluated as a gravel admixture layer, the gradation sizes are compared with the computed D_{50-min} and D_{15-min} to

determine the % Gravel. Then the percentages of the finer soil and the general soil are determined. These values are compared with the allowable percentages for each material classification. Finally the thickness of the total admixture layer is established.

GRAVEL ADMIXTURE SELECTION FOR A GRADATION RANGE

The procedure for the gravel admixture can be used to test for a single specified gradation and determine the applicable layer thickness appropriate to that gradation. It does not directly give the appropriate thickness when a gradation range is specified for a given location. When a gradation range is identified, the material that could be supplied may fall anywhere within the gradation band. Checking the computed thickness for only the minimum and maximum gradations does not provide a thorough examination of the possible gradations. A series of nine possible gradation scenarios within the specified gradation range is examined to determine the critical admixture layer thickness, Y_{Total} , applicable to a single slope and length condition. While each of the gradation scenarios will be within the specified gradation range, computations commonly show that the maximum layer thickness is obtained when using a gradation other than the maximum or minimum gradation. A single thickness and slope is used to compute the Y_{Total} for a specified gradation, but it is also possible to examine a range of slopes and lengths from 3% to 10% that can utilize the same gradation and Y_{Total} .

APPLICATION OF DESIGN PARAMETERS

A gravel admixture was applied to a typical municipal landfill site in a semi-arid climate. A multiple page spreadsheet was used to perform the computation. A section of a top cover with an area of 0.173 ha (0.428 ac) and a uniform slope of 0.05 m/m is considered. A summary of the design parameters are given below:

Design storm for erosion stability = 100-year frequency (1% per year)

Top slope = 0.05 m/m (5%)

Overland flow slope length = 83 m (273 ft)

Peak flow = 0.071 m³/s (2.5 cfs)

Unit flow rate = 0.042 m²/s (0.454 ft²/s)

Maximum channel velocity = 1.006 m/s (3.30 ft/s)

Hydraulic depth of channel flow = 42 mm (0.138 ft)

Froude number = 1.57

Computed D_{50} of gravel portion = 28 mm (1.11 in.), use 32 mm (1.25 in.)

Required thickness of armor layer = 57 mm (2.25 in.)

Computed thickness of gravel/soil admixture layer, Y_{Total} = 0.254 m (10 in.)

The design admixture gradation for the 0.173 ha area at a slope of 0.05 m/m is shown on Figure 1. The design admixture gradation from Figure 1 with a layer thickness, Y_{Total} , of 0.254 m (10 in) and slope of 0.05 m/m (5%) can also be applied to a spreadsheet analysis for slopes from 0.03 to 0.10 m/m (3 to 10%). Slopes flatter than 0.05 m/m will allow larger runoff areas and longer overland flow slope lengths, and slopes steeper than 0.05 m/m will require smaller runoff areas and shorter overland flow slope lengths.

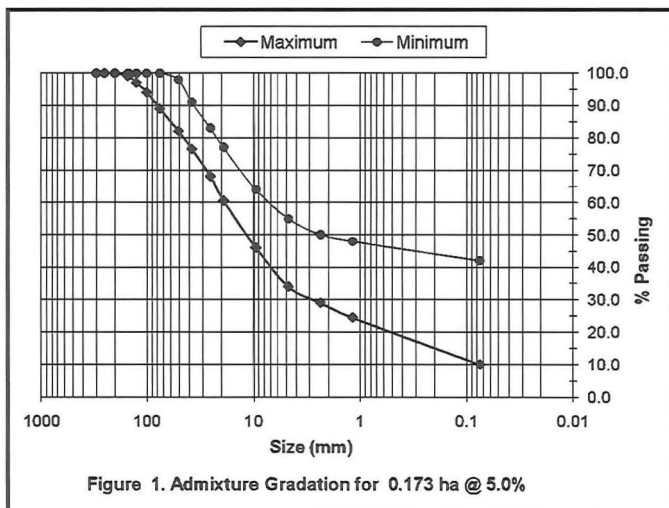


Table 1 shows values for the runoff areas and overland flow lengths that can be applied to the Figure 1 gradation with a 0.254 m (10 in) layer thickness. Moderate increases in the allowable runoff areas and overland flow lengths can also be obtained by increasing the layer thickness to 0.305 m (12 in) for the same gradation range. Table 1 also shows the areas and overland flow length when the thickness is increased.

Table 1. Gravel Admixture Runoff Areas and Overland Flow Lengths

Layer thickness (m)	Max. Area at 3% slope (ha)	Max. Area at 4% slope (ha)	Max. Area at 5% slope (ha)	Max. Area at 6% slope (ha)	Max. Area at 7% slope (ha)	Max. Area at 8% slope (ha)	Max. Area at 9% slope (ha)	Max. Area at 10% slope (ha)
0.254	0.372	0.244	0.173	0.130	0.103	0.084	0.070	0.060
0.305	0.590	0.379	0.270	0.203	0.161	0.132	0.109	0.093
Layer thickness (m)	Max. Length at 3% slope (m)	Max. Length at 4% slope (m)	Max. Length at 5% slope (m)	Max. Length at 6% slope (m)	Max. Length at 7% slope (m)	Max. Length at 8% slope (m)	Max. Length at 9% slope (m)	Max. Length at 10% slope (m)
0.254	122	99	83	72	64	58	53	49
0.305	154	123	104	90	80	73	66	61

A similar gravel admixture design was applied to a demonstration landfill cover constructed in northwestern New Mexico (Anderson and Stormont, 2005). The procedure described here is being applied to a landfill cover soon to be constructed in

southern Nevada. The Nevada project will provide the first large scale application of the procedure.

CONCLUSIONS

Measures to control erosion are a significant part of the safe function of landfills. While measures such as revegetation and application of organic mulches may reduce erosion in some climates, mechanical stabilization by a gravel veneer or a gravel admixture layer will likely be required to prevent water erosion in the arid and semi-arid Southwest. The design method for gravel admixtures presented here may provide erosion protection that does not reduce the evaporation rate, or create a habitat for deep-rooted plants.

REFERENCES

- Abt, S. R. and Johnson, T. L. (1991). "Riprap Design for Overtopping Flow." *Journal of Hydraulic Engineering*, 117 (8), pp 959-972.
- Anderson, C. E., and Stormont, J. C. (2005). "Gravel Admixtures for Erosion Protection in Semi-Arid Climates." *Erosion of Soils and Scour of Foundations, Proceedings of Sessions of the Geo-Frontiers 2005 Congress*, Austin, Texas.
- Anderson, G. K., et al. (1970). Tentative Design Procedure for Riprap-Lined Channels, Highway Research Board, NCHRP Report Number 108.
- Finley, J. B., Harvey, M. D., and Watson, C. C. (1985). "Experimental Study: Erosion of Overburden Cap Material Protected by Rock Mulch." *Seventh Symposium on Management of Uranium Mill Tailings, Low-Level Waste and Hazardous Waste*, Fort Collins, Colorado, 273-282.
- Kemper, W. D., Nicks, A. D., and Corey, A. T. (1994). "Accumulation of Water in Soils under Gravel and Sand Mulches." *Soil Science Society of America Journal*, 58, 56-63.
- Simons, D. B., Li, R. M., et al. (1980). *Watershed and Stream Mechanics*, prepared for the US Department of Agriculture, Soil Conservation Service, Washington, D.C.
- Simons, Li and Associates (1982). *Engineering Analysis of Fluvial Systems*, Fort Collins, CO.
- Waugh, W. J., and Petersen, K. L. (1994). "Paleoclimatic Data Application: Long-term Performance of Uranium Mill Tailings Repositories." *Climate Change in the Four Corners and Adjacent Regions: Implications for Environmental Restoration and Land-Use Planning, Proceedings of the Workshop*, Mesa State College, Grand Junction, Colorado, 163-185.
- Wischmeier, W. H., and Smith, D. D. (1978). "Predicting Rainfall Erosion Losses, A Guide to Conservation Planning." *Agriculture Handbook Number 537*, United States Department of Agriculture, Science and Education Administration, Washington, D.C.

Erosion Protection at Landfill Slopes Greater than 10%

Clifford Anderson¹, M. ASCE, PE, PhD, D.WRE and Steve Wall²

¹Department of Engineering, Central Connecticut State University, 1615 Stanley Street, New Britain, CT 06050-4010, USA, email: cliff@ahymo.com

²Office of Pollution Prevention and Solid Waste (WST-7), US EPA Region 9, 75 Hawthorne St., San Francisco, CA 94105, USA, email: Wall.Steve@epamail.epa.gov

ABSTRACT

In arid climates the steep side slopes of a landfill can be sources of severe erosion. The amount of vegetation that can be sustained commonly does not provide significant erosion protection, and alternative erosion protection measures are required. The commonly used side slope terrace drains can be difficult to construct and maintain. A method is presented to compute the gradation and thickness of a rock surface erosion protection layer that will allow for longer slope lengths than has been commonly applied. The procedure considers peak flow, slope and the formation of surface channelization. Criteria for applying a granular filter are also considered. As an alternative to separately placed riprap and granular filter layers, a combined mixture could serve the same function as separate layers, and reduce construction costs. A gradation range is considered for a combined mixture, and a series of gradations within the range is examined to determine the critical layer thickness. Examples of a resulting side slope design are presented.

INTRODUCTION

The steep side slopes of a landfill can be sources of erosion if surface runoff is allowed to accumulate on the steep slopes and the side slope surfaces are constructed with erosive materials. In some climates, vegetation can be utilized to reduce runoff velocities and stabilize surface soils. In arid climates the amount of vegetation that can be sustained commonly does not provide significant erosion protection, and alternative erosion protection measures are required. One erosion protection method commonly used limits the slopes to short lengths by the construction of side slope terrace drains, with additional protection provided by the addition of gravel armoring to the slopes. Side slope terrace drains can be difficult to construct and maintain, and their placement on existing slopes may provide additional construction difficulties. The procedures described in this document can be used to guide the design of a rock surface erosion protection layer that will allow for longer slope lengths than has been commonly applied. The longer slope lengths may greatly reduce or eliminate the need for side slope terrace drains.

It is desirable to reduce the amount of surface water that can enter the zone of fill, and this is typically accomplished by construction of a barrier layer above the area of fill. Studies in arid climates have shown that a thick soil layer can provide a superior barrier layer, because of the moisture storage properties of the soil, and high rates of evaporation and plant transpiration. Some studies have indicated that placement of a surface gravel layer will increase surface infiltration and reduce

evaporation so that the efficiency of a soil barrier layer is reduced. However, for very steep slopes the runoff percentages will be much higher than for flatter slopes, and the effects of surface gravel on overall evaporation will be minimized. When slopes are at 10% or steeper, and the base soil does not allow for the rapid infiltration of surface water, a gravel layer or "vener" can provide surface erosion protection without significantly reducing the function of the soil barrier layer.

The size of the gravel and layer thickness is normally based on a constructed watershed condition and a critical design slope. The design of a gravel veneer to protect steep side slopes from erosion requires evaluation of small watershed hydrology and hydraulics, and the design of the conveyances where water is expected to flow. In the case of steep uniformly graded or gradually varying embankment slopes, a fixed flow path or channel may not be constructed on the surface, but channelization will occur because of normal construction variability, settlement, and on-going erosion processes. Site physical conditions and experience at similar existing sloped areas can be used to establish surface flow criteria using geomorphologic equations. The resulting flow rates and velocities based on geomorphology will generally be larger than when only existing or constructed site topography is used.

Construction of a gravel veneer commonly includes a separately placed finer filter soil below the gravel, but construction could be simplified if the filtering material could be placed concurrently with the gravel. The design of a combined gravel-filter erosion layer is described in this document.

Using critical flow depth, velocity and slope criteria, a single gravel veneer gradation and thickness can be designed. When slopes and runoff areas vary widely, an alternative approach is to use preliminary analyses to determine veneer gradations, then to use this information as a guide for selection of material gradations that can be efficiently produced. Each selected gradation can then be evaluated to determine the range of site conditions where the gradation can be safely applied.

PEAK FLOW AND UNIT DISCHARGE

Erosion of landfill side slopes is most problematic during severe precipitation when erosion can remove waste from a landfill and convey it to downstream areas. For a landfill side slope in the arid and semi-arid areas of the southwest United States a 200-year event is a suggested design flow condition, because of the significant environmental damage that can result from side slope erosion. Special site requirements and waste materials may warrant use of more severe event frequencies. For any given watershed, the 200-year frequency event peak flow (Q_{200}) can be determined from a basic hydrologic analysis, such as with the Rational Method or NRCS Curve Number (CN) procedure. Peak flow during the storm event is the most important hydrologic property to accurately predict erosion. For a planar surface with an identified length, but a width that can be identified only after erosion has occurred, the recommended watershed width for runoff computations should be 25% of the watershed length. The dominant discharge peak flow (Q_m) can be evaluated by considering the statistically weighted average of the peak runoff occurring over a long period, for example 100 years. In the arid southwestern the Q_m can be estimated at 10% of Q_{100} . For any given watershed, the relationship between the 200-year

frequency event peak flow (Q_{200}) and the 100-year frequency event peak flow (Q_{100}) can be determined from a basic hydrologic analysis. Therefore, the value of Q_{100}/Q_{200} will have a fixed value for any single watershed. The ratio of Q_m/Q_{200} can be determined from Q_m/Q_{100} and Q_{100}/Q_{200} . For example, if the Q_{100}/Q_{200} is determined to be 0.78, the Q_m can be estimated as 7.8% of Q_{200} .

By following the analysis procedure described in "Design of Erosion Protection at Landfill Areas with Slopes Less than 10%" (Anderson and Wall, 2010, this volume), and substituting the Q_{200} for the Q_{100} , the hydraulic depth equation is:

$$d_h = (43.7)^{-0.6} \left(\frac{Q_m}{Q_{200}} \right)^{-0.6} Q_m^{0.372} \left[0.0488 \left(\frac{D_{50}}{1000} \right)^{0.167} \right]^{0.6} s^{-0.3} M^{0.234} \quad [1]$$

where: d_h is the hydraulic depth (m),
 Q_{200} is the peak flow at 200-year frequency (m^3/s),
 Q_m is the dominant discharge (m^3/s),
 D_{50} is the median size of the rock riprap (mm).
 M is the percentage of silt and clay in the channel perimeter
 and s is the slope of the channel profile (m/m).

Equation [1] describes the flow width based on the geomorphologic equation of Simons, Li and Associates (1982, and Simons and Li, 1980). Except for the D_{50} , all of the values in this equation can be estimated from physical watershed properties. This equation and Manning's equation can also be used to compute the 200-year event unit discharge, Q_{200}/b , and the width-to-depth ratio, b/d_h . While the dominant discharge, Q_m , is used in equation [1], the computed hydraulic depth, d_h , represents the depth from a 200-year frequency event.

A second geomorphologic parameter is the width-to-depth ratio of the flowing water. For arid and semi-arid conditions a maximum width-to-depth ratio of 40 is recommended. If the width-to-depth ratio, b/d_h , exceeds 40, the b and the d_h must be re-computed to maintain a width-to-depth ratio of 40. The width-to-depth relation can be used to obtain an alternate equation for the hydraulic depth as:

$$d_h = [(Q_{200} n)/F]^{0.375} s^{-0.1875} \quad [2]$$

where: F is the width-to-depth ratio. (Use a value of 40)
 and n is the Manning's roughness coefficient.

Equation [2] describes the flow width and depth based on a defined width-to-depth ratio. Equation [2] should be used whenever the b/d_h computed from equation [1] exceeds 40. Using Manning's equation and equation [1] or [2], the flow velocity, V_{100} , the Froude number, F_r , the width of flow, b , and the unit discharge, q_f , can be computed.

RIPRAP ROCK SIZE

With the flow properties established, the S. R. Abt and T. L. Johnson equation

(1991) can be used to solve for the median rock size of the gravel veneer. The basic Abt and Johnson equation provides a prediction of the flow conditions when failure is expected to occur, but for constructed applications, failure at the design flow is not tolerable. "Riprap design should be directed toward preventing stone movement and to insure the riprap layer does not fail" (Abt and Johnson, 1991, page 962). Abt and Johnson state that the values from the basic equation "should be adjusted to prevent stone movement" (Abt and Johnson, 1991, page 967). In addition, actual construction is expected to be somewhat more variable than the hand placement of rock in a controlled laboratory experiment, and minor construction variability could cause failure prior to the conditions identified in the Abt and Johnson field laboratory testing. Abt and Johnson recommend that factor of safety of 1.2 be applied to the rock size equation (page 967).

The Abt and Johnson equation uses the unit discharge, and profile slope to compute the median rock size when failure is expected to occur. The unit discharge is computed using the smallest b derived using Manning's equation and equation [1] or [2] so that the computed unit discharge is the maximum value computed from the two equations. The equation for unit discharge is:

$$q_f = Q_{200}/b \quad [3]$$

where: q_f is the unit discharge or unit flow rate (m^2/s).

The Abt and Johnson equation with the addition of the recommended factor of safety and converted to metric form is:

$$D_{50} = (1.2 \times 502.9) s^{0.43} q_f^{0.56} \quad [4]$$

where: D_{50} is the median rock size of the gravel veneer (mm).

The physical testing by Abt and Johnson did not use slopes steeper than 20% (0.20 m/m) and the extension of the procedure to slopes steeper than 33% (0.33 m/m) is not recommended. Abt and Johnson's paper suggested that the gravel layer thickness should be 1.5 to 3.0 times the D_{50} . However, only two of their 26 tests had a layer thickness less than 2.0 times the D_{50} . All of their tests were for separately placed riprap and granular filter layers.

CRITERIA FOR GRAVEL VENEER RIPRAP AND FILTER

The D_{50} computed from equation [4] can be used to determine the rock gradation for the gravel veneer and the total thickness of the veneer layer. The following procedure is recommended:

- specify a construction minimum D_{50} (D_{50-min}) based on the computed value from equation [4] rounded to the nearest 6.4 mm (0.25 inch).
- specify a design maximum D_{50} (D_{50-max}) at 140% of the D_{50-min} , rounded to the nearest 6.4 mm (0.25 inch).
- specify a minimum D_{100} ($D_{100-min}$) at 150% of the D_{50-min} , rounded to

the nearest 6.4 mm (0.25 inch).

- specify a design maximum D_{100} ($D_{100-max}$) at 200% of the D_{50-min} , rounded to the nearest 6.4 mm (0.25 inch). The constructed veneer can have a larger value with an appropriate adjustment in the layer thickness.
- specify a minimum D_{15} (D_{15-min}) at 45% of the D_{50-min} , rounded to the nearest 6.4 mm (0.25 inch).
- specify a design maximum D_{15} (D_{15-max}) at 80% of the D_{50-min} , rounded to the nearest 6.4 mm (0.25 inch).
- specify the coefficient of uniformity ($C_u = D_{60} / D_{10}$) with an allowable range between 1.75 and 3.0.
- specify the minimum rock layer thickness (Y_{min}) at the 2.0 times the D_{50-min} , or 1.0 times the $D_{100-max}$, whichever is larger.

The Abt and Johnson physical testing used rock with an average specific gravity of 2.66. In order to use equation [4] without adjustment, the rock in the gravel veneer should have an average specific gravity of 2.65 or larger. This is equivalent to a particle unit weight of 2650 kg/m³ (165 lbs/ft³). If any rock with a smaller average specific gravity is proposed for use, the size of the D_{15} , D_{50} , D_{100} , and Y_{min} would need to be adjusted based on the ratio of the buoyant weight of the rock.

The gravel veneer in the Abt and Johnson testing used a granular filter immediately below the rock layer. Filter material is placed below the rock layer to prevent loss of material below the layer which would cause failure of the erosion layer. The size of the granular bedding must be based on size of the gravel in the erosion layer. Some guidelines on granular filter design can be found in the US Federal Highway Administration, Hydraulic Engineering Circular No. 11 (1989, FHWA-IP-89-016). The following procedure is recommended:

- specify a minimum *Filter* D_{85} (*Filter* D_{85-min}) at 20% of the maximum veneer D_{15} (D_{15-max}), rounded to the nearest 0.25 mm (0.01 inch).
- specify a minimum *Filter* D_{50} (*Filter* D_{50-min}) at 4% of the maximum veneer D_{50} (D_{50-max}), rounded to the nearest 0.25 mm (0.01 inch).
- specify a design minimum *Filter* D_{60} (*Filter* D_{60-min}) at 140% of the minimum *Filter* D_{50} (*Filter* D_{50-min}), rounded to the nearest 0.25 mm (0.01 inch).
- specify a design minimum *Filter* D_{10} (*Filter* D_{10-min}) at the minimum *Filter* D_{60} (*Filter* D_{60-min}) divided by 3.5, rounded to the nearest 0.25 mm (0.01 inch).
- specify the *Filter* coefficient of uniformity (*Filter* $C_u = \text{Filter } D_{60} / \text{Filter } D_{10}$) with an allowable range between 2.0 and 3.5.
- specify the minimum *Filter* layer thickness (*Filter* Y_{min}) at 0.152 m (6.0 inches).

For the range of gravel veneer sizes that are likely to be required for steep landfill slopes, a typical roadway aggregate base will typically contain a higher percentage of finer grained soils than is recommended to meet granular filter criteria. Table 1 provides two granular filter gradations that might be considered with steep

sloped rock layers. The Type A Granular Soil Filter in Table 1 can generally be used when the veneer D_{50-min} is 100 mm (4.0 inches) or less. The Type B Granular Soil Filter can generally be used when the veneer D_{50-min} is between 100 mm (4.0 inches) and 180 mm (7.0 inches). A somewhat finer filter could be specified for cases where the D_{50-min} is smaller than 65 mm (2.5 inches). For each gravel veneer size, the *Filter D_{85-min}* , *Filter D_{50-min}* , and *Filter D_{10-min}* should be examined to verify that the appropriate Granular Filter Soil (Type A or B) is used.

Table 1. Suggested Granular Filter Gradations

Granular Filter Soil - Type A		Granular Filter Soil - Type B	
Passing	% by weight	Passing	% by weight
75 mm (3 inch)	100%	100 mm (4 inch)	100%
20 mm (3/4 inch)	30 to 90%	25 mm (1 inch)	30 to 80%
10 mm (3/8 inch)	10 to 70%	10 mm (3/8 inch)	5 to 40%
#4 (0.475 mm)	0 to 20%	#4 (0.475 mm)	0 to 20%
#200	0 to 3%	#200	0 to 3%

A SINGLE RIPRAP-FILTER LAYER

As an alternative to separately placed riprap and granular filter layers, a combined material layer could serve the same function as the separate layers, and reduce construction costs. With a riprap-filter mixture the resulting material properties need to be examined to determine if the erosion protection and the filtering criteria can be met. With the riprap-filter mix, it is possible to perform some material selection and processing to produce different classes of mix, but more refined material selection may not be feasible.

Rather than specify detailed rock and filter gradations applicable to a single design flow and slope, a preliminary design to determine rock and filter gradations can be used in selecting a riprap-filter mixture that can be efficiently produced. Even with material from a single source area, it is expected that there will be variability of test results. The arithmetic mean and standard deviation of the test data are important measurements to obtain a specified gradation range. It may be desirable to specify a wider range of particle sizes than would be indicated by statistical sampling of a single source in order to allow greater flexibility in material source selection and processing. However, a larger range of values will change the layer erosion protection capability and may reduce the design efficiency. There are limits to the range of allowable gradations. For example, if there is not a sufficient quantity of particles that resist the erosive forces, no additional thickness can compensate for this deficiency.

With a specified riprap-filter mix the gradation of the portion of the mix that can be considered as riprap must be considered. Particle sizes at "25% of the D_{50} " can carry only 8.4% of the unit discharge of particles at "100% of the D_{50} ". Based on examination of riprap guide specifications from several sources, particle sizes in the riprap-filter mix that are smaller than 25% of the computed D_{50} , should not be included in the riprap portion of the mix. The US Dept. of Transportation, Federal Highway Administration, *Design of Riprap Revetment* (Hydraulic Engineering

Circular, FHWA-IP-89-016, 1989, p.36) recommends D₁₅ at 40% to 60% of the D₅₀. The percentage of riprap size material in a proposed gradation can be determined from the percentage of material passing the computed "25% of the D₅₀", where:

$$\%Riprap = 100\% - \% \text{ passing "25\% of } D_{50}" \quad [5]$$

Using a similar procedure, the percentage of effective filtering material can be determined. For the range of gravel sizes expected, any particle sizes that pass a #10 sieve (2.0 mm) should not be considered as contributing to riprap filtering. Therefore the percentage of filter material in a gradation can be computed as:

$$\% Filter = \% \text{ passing "25\% of } D_{50}" - \% \text{ passing \#10 sieve (2.0 mm)} \quad [6]$$

With the % Riprap and % Filter established, it is also possible to use the total grain size distribution to obtain an equivalent riprap grain size distribution for the portion of the particle sizes that can be considered as riprap. The individual sieve size percent passing values for the riprap portion are computed as:

$$\% \text{ passing riprap portion} = 100\% \left(1 - \frac{(100\% - \% \text{ passing})}{\% \text{ riprap}} \right) \quad [7]$$

Using the grain size values for the riprap portion, the $D_{15 \text{ riprap}}$, $D_{50 \text{ riprap}}$, $D_{85 \text{ riprap}}$ and $D_{98 \text{ riprap}}$ of the riprap can be computed. The basic riprap layer thickness is computed as:

$$T_{Riprap-1} = 1.6 \times D_{50 \text{ Riprap}} \quad \text{or} \quad [8]$$

$$T_{Riprap-1} = (0.6 \times D_{90 \text{ Riprap}}) + (0.9 \times D_{85 \text{ Riprap}}) \quad [9]$$

whichever is smaller, but not less than:

$$T_{Riprap-1} = 2 \times \text{computed } D_{50} \quad [10]$$

When the $D_{15 \text{ riprap}}$ is smaller than 40% of the computed D_{50} , there is more small size material than is recommended for a normal riprap gradation and the riprap layer thicknesses should be adjusted for the excess of smaller material by the following equation:

$$T_{Riprap-2} = \left[1 - \frac{\left(0.15 \left(\ln(D_{15 \text{ Riprap}}) - \ln(25\% \text{ comp } D_{50}) \right) \right)}{\left(\ln(40\% \text{ comp } D_{50}) - \ln(25\% \text{ comp } D_{50}) \right)} \right] \left(\frac{T_{Riprap-1}}{0.85} \right) \quad [11]$$

When the sample $D_{50 \text{ riprap}}$ is smaller than the computed D_{50} , the average size of the riprap is too small and the riprap layer thickness is adjusted by the following equation:

$$T_{Riprap-3} = \left[1 - \left(\frac{0.50 (\ln(D_{50Riprap}) - \ln(25\% \text{ comp } D_{50}))}{\ln(40\% \text{ comp } D_{50}) - \ln(25\% \text{ comp } D_{50})} \right) \right] \left(\frac{T_{Riprap-1}}{0.50} \right) \quad [12]$$

The riprap layer thickness then is the largest value, or:

$$T_{Riprap} = \text{Maximum} (T_{Riprap-1}, T_{Riprap-2}, T_{Riprap-3}) \quad [13]$$

The minimum percentage of filter in the gravel-soil mix is determined from the following equation derived from typical riprap filter designs:

$$\text{Min \% Filter} = \%Riprap \times (15\% \text{ of } D_{50})/4.0 \quad [14]$$

but not less than $0.10 \times \% Riprap$ or more than $0.25 \times \% Riprap$. The computed $\% Filter$ material is compared with this sample value, and if the Min \% Filter is greater than the $\% Filter$ provided, the total layer thickness is adjusted.

If the percentage of the material finer than the Riprap size in the sample gradation does not exceed 25%, and the Minimum \% Filter does not exceed the $\% Filter$ provided by the gradation, the computed T_{Riprap} will also be the computed layer thickness. When these conditions are not met, the total layer thickness must be adjusted to account for filter bulking or $\% Filter$ deficiency. The following equation is used:

$$T_{Layer} = \left[\text{Max} \left(\frac{75\%}{\%Riprap}, 1 \right) \right] \times \left[\text{Max} \left(\frac{\text{Min \%Filter}}{\%Filter}, 1 \right) \right] \times T_{Riprap} \quad [15]$$

with T_{Layer} never less than T_{Riprap} .

GRAVEL RIPRAP-FILTER SELECTION FOR A GRADATION RANGE

The procedure for the riprap-filter mix can be used to test a single specified gradation and determine the applicable layer thickness appropriate to that gradation. It does not directly give the appropriate thickness when a gradation range is specified for a given location. When a gradation range is identified, the material that could be supplied may fall anywhere within the gradation band. Checking the computed thickness for only the minimum and maximum gradations does not provide a thorough examination of the possible gradations. A series of nine gradation scenarios within the gradation range is examined to determine the critical admixture layer thickness, T_{Layer} , applicable to a single slope and length condition. With a single thickness and slope used to compute the T_{Layer} for a specified gradation, it is also possible to examine a range of slopes and lengths from 10% to 30% that can utilize the same gradation and T_{Layer} .

APPLICATION OF DESIGN PARAMETERS

A riprap-filter mix was applied to a typical landfill side slope in an arid climate. A multiple page spreadsheet was used to perform the computation. A section of the side slope with an area of 0.468 ha (1.157 ac) and a uniform slope of 0.20 m/m was considered. A summary of the design parameters are given below:

Design storm for erosion stability = 200-year frequency (0.5% per year)

Top slope = 0.20 m/m (20%)

Overland flow slope length = 137 m (449 ft)

Peak flow = 0.319 m³/s (11.27 cfs)

Unit flow rate = 0.130 m²/s (1.396 ft²/s)

Maximum channel velocity = 2.11 m/s (6.92 ft/s)

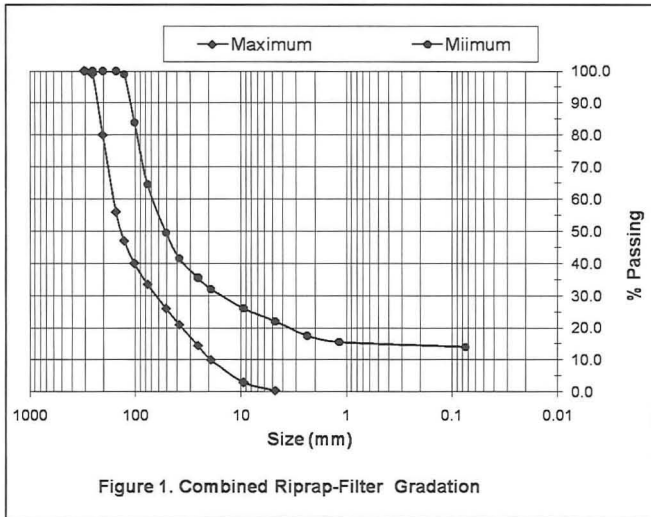
Hydraulic depth of channel flow = 62 mm (0.202 ft)

Computed D_{50} of riprap portion = 96 mm (3.79 in.), use 95 mm (3.75 in.)

Required thickness of riprap only = 0.203 m (8.00 in.)

Computed thickness of riprap-filter layer, T_{Layer} = 0.254 m (10 in.)

The design admixture gradation for the 0.468 ha area at a slope of 0.20 m/m is shown on Figure 1.



The design admixture gradation from Figure 1 with a layer thickness, T_{Layer} , of 0.254 m (10 in) and slope of 0.20 m/m (20%) can also be applied to a spreadsheet analysis for slopes from 0.10 to 0.30 m/m (10 to 30%). Slopes flatter than 0.20 m/m will allow larger runoff areas and longer overland flow slope lengths, and slopes steeper than 0.20 m/m will require smaller runoff areas and shorter overland flow slope lengths. Table 2 shows values for the runoff areas and overland flow lengths that can be applied to the Figure 1 gradation with a 0.254 m (10 in) layer thickness.

Table 2. Riprap-Filter Mix Runoff Areas and Overland Flow Lengths

Layer thickness (m)	Max. Area at $\leq 12\%$ slope (ha)	Max. Area at $\leq 14\%$ slope (ha)	Max. Area at $\leq 16\%$ slope (ha)	Max. Area at $\leq 18\%$ slope (ha)	Max. Area at $\leq 20\%$ slope (ha)	Max. Area at $\leq 22\%$ slope (ha)	Max. Area at $\leq 26\%$ slope (ha)	Max. Area at $\leq 30\%$ slope (ha)
0.254	1.024	0.808	0.660	0.551	0.468	0.406	0.313	0.251
Layer thickness (m)	Max. Length at $\leq 12\%$ slope (m)	Max. Length at $\leq 14\%$ slope (m)	Max. Length at $\leq 16\%$ slope (m)	Max. Length at $\leq 18\%$ slope (m)	Max. Length at $\leq 20\%$ slope (m)	Max. Length at $\leq 22\%$ slope (m)	Max. Length at $\leq 26\%$ slope (m)	Max. Length at $\leq 30\%$ slope (m)
0.254	202	180	162	148	137	127	112	100

CONCLUSIONS

Measures to control erosion at the steep side slopes of a landfill are critical for safe function. Mechanical stabilization of steep slopes by a combined riprap-filter layer can be used to prevent water erosion. Standard rainfall-runoff procedures can be combined with geomorphologic equations to compute channelized flow. Procedures commonly applied to determine riprap size and filter gradation can then be modified to establish requirements for a single riprap-filter layer. The resulting riprap-filter gradation can then be evaluated for a range of slope and watershed conditions to determine applicable layer thicknesses. The design method presented here was prepared to guide the construction of erosion protection for steeply sloped areas on a landfill in the arid and semi-arid Southwest. However, the method implements design concepts that are commonly applied at steep slopes, and the design method could be readily adapted to any slopes where rock veneers are warranted.

REFERENCES

- Abt, S. R. and Johnson, T. L. (1991). "Riprap Design for Overtopping Flow." *Journal of Hydraulic Engineering*, 117 (8), pp 959-972.
- Simons, D. B., Li, R. M., et al. (1980). *Watershed and Stream Mechanics*, prepared for the US Department of Agriculture, Soil Conservation Service, Washington, D.C.
- Simons, Li and Associates (1982). *Engineering Analysis of Fluvial Systems*, Fort Collins, CO.
- US Federal Highway Administration (1989). *Design of Riprap Revetment*, Hydraulic Engineering Circular No. 11, FHWA-IP-89-016, Washington, D. C.